

**CHARACTERIZATION OF DAMAGE
EDGE DISTANCE EFFECTS ON THE
RESIDUAL STRENGTH OF METALLIC
HONEYCOMB SANDWICH PANELS
SUBJECTED TO EDGE-WISE
COMPRESSION**

**CARACTÉRISATION DES EFFETS DE
LA DISTANCE DE RIVE SUR LA
RÉSISTANCE RÉSIDUELLE DES
PANNEAUX SANDWICHS
MÉTALLIQUES EN NID D'ABEILLE
ENDOMMAGÉS SOUMIS À UNE
COMPRESSION AU NIVEAU DES RIVES**

A Thesis Submitted to the Division of Graduate Studies
of the Royal Military College of Canada
by

Patrick Wheeler, BEng
Major

In Partial Fulfillment of the Requirements for the Degree of
Master of Applied Science in Mechanical Engineering, Structures

April, 2024

© This thesis may be used within the Department of National Defence
but copyright for open publication remains the property of the author.

To Erika and Evelyn for their support, encouragement, and sacrifices.

Acknowledgements

- Dr. Jeremy Laliberté for his continued support since the very beginning of my graduate studies in 2016 at Carleton University.
- Dr. Diane Wowk for allowing me to join her team and for her guidance and mentorship over the past two years.
- Brendan Freeman, Curtis Keogh, Jason Pell, Charles Sadiq, and Cory Sharpe for their reliable support, advice, and for making the work fun.
- Alek Pach and Dr. Mengqian (Cathy) Sun for sharing the workspace and their help at every step of the way.
- DND and the AERE community for this opportunity.

Abstract

Honeycomb sandwich panels are a type of structural composite that is widely used in aerospace applications because of their exceptional stiffness and strength-to-weight properties. Throughout their service life, many sandwich panels will experience damage in the form of dents on the facesheet caused by low-velocity impacts with foreign objects. This damage, depending on the size and location, can cause a significant reduction in the residual strength of the sandwich panel and affect the way the loads are carried by the structure. Although all known aircraft structural repair manuals have a minimum required distance between a dent and the edge of the sandwich panel, the technical data packages supporting these limitations are subject to intellectual property restrictions. No academic literature has been found discussing and quantifying the effects of damage edge distance on sandwich panels.

The current work, taking advantage of existing industry standards where possible, presents a new experimental approach to characterizing the damage edge distance effects on dented sandwich panel specimens subjected to compression after impact tests. The effects are characterized as changes in residual strength, failure mode, and facesheet strain behaviour. Data are collected using a combination of displacement, load cell, and three-dimensional digital image correlation instruments.

The test methodology developed, including test panel fabrication, testing, and data collection using three-dimensional digital image correlation, successfully characterized damage edge distance effects. For smooth circular dents 20 % of panel thickness in depth and 43 mm in diameter, the damage edge distance was found to affect residual strength, failure mode, and facesheet strain at damage edge distances up to 60 mm. The residual strength was found to have an inverse correlation with the damage edge distance. Edge distance effects were observed in the form of asymmetric dent growth and delayed macrobuckling of the sandwich panel. Finally, the facesheet strain became asymmetric in the presence of edge effects. Hypotheses are proposed as to why these effects occurred and how loads transfer from the sandwich panel into the adjacent structure when edge effects are present.

Résumé

Les panneaux sandwich en nid d'abeille sont un type de composite structurel utilisé dans les applications aérospatiales en raison de leurs rapports exceptionnelles de rigidité-poids et résistance-poids. De nombreux panneaux subissent des dommages sous la forme d'indentation sur la semelle causée par des impacts à faible vitesse avec des objets étrangers. Ces dommages, en fonction de leur taille et de leur emplacement, peuvent entraîner une réduction significative de la résistance résiduelle du panneau et affecter la façon dont les charges sont supportées. Bien que tous les manuels de réparation des structures d'aéronefs connus prévoient une distance minimale entre une indentation et la rive du panneau (distance de rive), les ensembles de données techniques étayant ces limites sont sujets aux droits de propriété intellectuelle. Aucune littérature académique n'a été trouvée qui traite et quantifie les effets de la distance de rive des dommages aux panneaux sandwichs.

Le présent travail, qui tire parti des normes existantes, présente une nouvelle approche expérimentale pour caractériser les effets des distances de rive. Pour caractériser ces effets des spécimens indentés sont soumis à des essais de compression après impact. Les effets sont caractérisés par trois mesures; la résistance résiduelle, le mode de défaillance et la déformation relative de la semelle. Les données sont acquises à l'aide d'une combinaison d'instruments de déplacement, de capteur à jauge et de corrélation d'images numériques tridimensionnelles.

La méthodologie d'essai mise au point, comprenant la fabrication de panneaux, les essais et la collecte de données, a permis de caractériser avec succès les effets de la distance de rive. Pour les indentations circulaires lisses d'une profondeur de 20 % de l'épaisseur du panneau et d'un diamètre de 43 mm, on a constaté que la distance de rive affecte les trois mesures à des distances de rive allant jusqu'à 60 mm. La résistance résiduelle est inversement proportionnelle à la distance de rive. Concernant le mode de défaillance, les panneaux se sont déformés de manière asymétrique et le flambement du panneau a été retardé à ces mêmes distances de rive. Enfin, la déformation relative de la semelle est devenue asymétrique en présence d'effets de distance de rive. Des hypothèses sont proposées sur les raisons de ces effets et sur la manière dont les charges sont transférées à la structure adjacente change en présence d'effets de rive.

Contents

Acknowledgements	iii
Abstract	iv
Résumé	v
List of Tables	ix
List of Figures	x
1 Introduction	1
1.1 Motivation	2
1.2 Overall Approach and Constraints	3
1.3 Outline	5
2 Background	6
2.1 Sandwich Structures and Their Components	7
2.1.1 Sandwich Structure Facesheets	7
2.1.2 Sandwich Structure Cores	7
2.2 Sandwich Panel Design	10
2.3 Continued Airworthiness of Sandwich Panels in Aviation	11
2.4 Digital Image Correlation	12
2.4.1 2D DIC	13
2.4.2 3D DIC	13
3 Literature Survey	15
3.1 Foundations of Sandwich Panel Research	15
3.2 Recent Sandwich Panel Research	15
3.3 Sandwich Panel Damage Edge Distance Research	21
3.4 Use of 3D Digital Image Correlation for Research	21
3.5 Research opportunities	22
4 Methodology	24
4.1 Standards	26
4.1.1 Fabrication	26

4.1.2	Impact Damage	26
4.1.3	Residual Strength Testing	26
4.2	Test Panel Cutting	26
4.2.1	Rough Cut	27
4.2.2	Final Cut	27
4.3	End Potting	28
4.4	Test Panel Inspection and Measurements	30
4.5	Creating Damage	31
4.5.1	Drop Tower Design and Fabrication	31
4.5.2	Dent Sizing and Measurement	34
4.5.3	Drop Tower Operation and Damage Results	36
4.6	Speckle Pattern Application	37
4.6.1	Speckle Sizing	37
4.6.2	Speckling Methods	37
4.6.3	Speckling Procedure	38
4.7	Compression After Impact Testing	40
4.7.1	MTS and Support Fixture	40
4.7.2	3D DIC Setup and Calibration	40
4.7.3	Data Collection	42
4.7.4	Strain Validation	44
4.7.5	Test Procedure	47
4.8	Post-Processing	47
4.8.1	Strain Validation	47
4.8.2	MTS Data	48
4.8.3	3D DIC	48
4.8.4	Net Section Yield	50
4.8.5	Data Presentation and Sign Conventions	53
5	Results	54
5.1	Verification and Quality Control	54
5.1.1	3D DIC System Calibration and Resultant Accuracy	54
5.1.2	Strain Validation	55
5.1.3	Dent Depth and Width Measurements with 3D DIC	60
5.1.4	Panel Weights	64
5.1.5	Dimensional Tolerance, Squareness and Far-Field Strain	64
5.2	Residual Strength	67
5.3	Failure Mode and Deformation	71
5.4	Facesheet Strain	79
5.5	Stress-Strain Behaviour	87
6	Discussion, Analysis and Recommendations	89
6.1	Development of Test Methodology	89
6.1.1	Test Panel Fabrication	89
6.1.2	Test Panel Indentation	90

6.1.3	3D DIC	92
6.1.4	Strain Validation	93
6.1.5	CAI	93
6.2	Effects of Damage Edge Distance on Residual Strength	94
6.3	Effects of Damage Edge Distance on Failure Mode and Deformation	95
6.4	Effects of Damage Edge Distance on Strain and Asymmetry	101
6.5	Stress-Strain	103
6.6	Effects of Edge Distance and Engineering Application	105
7	Conclusion	107
7.1	FEA Model Validation	107
7.2	Experimental Test Methodology	107
7.3	Damage Edge Distance Effects	107
7.4	Overall Conclusion	108
	Bibliography	109
	Appendices	116
	A Test Reports and Calibration Certificates.	117
	B Tabulated Data Used for Graphs	120

List of Tables

4.1	Manual Dent Measurements.	37
4.2	DIC Equipment and Software List	40
4.3	Strain gauge system specifications.	44
4.4	MTS servohydraulic system specifications.	44
5.1	Subset and step size values for each test panel.	56
5.2	Dent Depth Measurement Comparison - Manual vs 3D DIC	61
5.3	Dent Width Measurement Comparison - Manual vs 3D DIC and ImageJ	62
5.4	Test Panel Weights.	64
5.5	Test panel dimension inspection results. All dimensions are in mm.	65
B.1	Deformation data presented in Figures 6.3 and 6.6. All values are averages.	120
B.2	Displacement data presented in Figure 6.7	120

List of Figures

1.1	Basic sandwich panel construction [3].	1
1.2	Sketch of damage edge distance, the distance between the centre of the dent and the closest edge of the panel.	4
2.1	Classification of cellular structures used in sandwich panels [2]. . .	8
2.2	Various 3D printed part infill patterns are used to provide structural support to outer layers of filament-printed components. Infill patterns, like more traditional sandwich core materials, are normally selected based on design needs [19].	9
2.3	Detailed view of single wall corrugated cardboard using a 2D prismatic design approach. In this industry, facesheets are called liners and cores are called medium [20].	9
2.4	Detailed honeycomb core cell view showing ribbon direction and repeated element consisting of three half-cell walls, two of thickness t and one of thickness $2t$ (ribbon direction). Figure adapted from Wierzbicki et al. [21].	10
2.5	Illustration of a DIC pixel subset captured and identified in the images [28].	12
2.6	Diagram showing a top-down view of the SBKF 3D DIC test setup. Eight vertically-separated 3D DIC cameras pairs each capture 45° of the SBKF cylinder to provide surface strain and 3D deformation data for the entire outer surface [29].	14
3.1	Comparison of simple-clamped vs supported sandwich panel edge-wise compression test fixtures.	18
3.2	Failure modes in sandwich columns subjected to edge compression. In compression tests, columns ends are constrained to in-plane movement. (a) Euler macrobuckling; (b) core shear macrobuckling; (c) facesheet microbuckling and (d) facesheet wrinkling [44].	19
3.3	Knife edge support component. This near top-down view of the support fixture component shows the front and rear facesheet knife edge supports used to prevent outward movement of the test panel at the vertical edge.	20

4.1	Sketch of the basic test setup. The test panel is installed in the two halves of the support fixture with lightly clamped and knife edge supports. Compression is performed vertically. 3D DIC cameras are vertically separated with a clear view of the dented facesheet.	25
4.2	Final cut saw setup was based on a wet tile saw. The main components adjusted and added are identified.	28
4.3	End potting effect on edge-wise compression tests.	29
4.4	Test panel top edges have been filled with construction adhesive and are curing.	29
4.5	Measurements taken for test panel dimension inspection.	31
4.6	Drop tower assembly. In this development test, the drop tower is configured with a 360 mm drop height and a spherical impactor of 25.4 mm (1 inch) diameter.	32
4.7	Drop tower base plate reference design from ASTM 7136 [49].	33
4.8	Dial indicator (distance amplifying instrument) with spherical tip on flat surface used to measure dent depth.	35
4.9	Dent measurement sketch showing the sandwich panel with a dented top facesheet and slightly deformed bottom facesheet placed onto a flat surface at a non-deformed section to provide a consistent panel placement. The panel is of thickness A. If the panel were to be placed entirely onto the flat surface, the top facesheet at the dent would be raised by distance B as opposed to the desired distance C. The dent depth is the difference between lengths A and C.	35
4.10	Speckle pattern applied to test panel.	39
4.11	ASTM 8287-compliant support fixture installed in MTS servohydraulic test system. Coordinate system is also identified.	41
4.12	Experimental setup. Key components are identified.	43
4.13	A strain validation panel was created from a wide aluminum bar. The bar was instrumented with a 30 mm strain gauge and a speckle pattern was applied to the top face. This apparatus permits comparison of DIC-calculated strain with strain gauge measurements.	45
4.14	Strain validation panel being processed in VIC-3D 9. The 30 mm strain gauge, the two digitally-applied 30 mm extensometers (E0 and E1), and the DIC area are identified. The scale shown is vertical strain, e_{yy} , from 0.37% (red) to 4% (purple).	46
4.15	Comparison of facesheet strains calculated using VIC-3D 9 for the same correlation image. Note that von Mises strain calculation always return a positive value, even in compression.	49
4.16	Sample deformation image before being processed. Knife edge bolt spacing was used as reference to set the image scale.	51
4.17	Typical tensile and compressive stress-strain and compressive tangent-modulus curves for 2024-T3-clad aluminum alloy sheet at room temperature [57].	52

5.1	Results from the strain validation performed at the start of batch experimental testing on 28 November 2023. Readings from the 30 mm strain gauge, the average DIC strain, and the average of two digital extensometers placed on either side of the strain gauge in DIC post-processing are compared.	57
5.2	Bland-Altman plot comparing the 30 mm strain gauge % strain reading with average validation panel speckle area % strain measured using 3D DIC. Data is from the strain validation test completed at the third of three batch experimental testing events, 28 November 2023.	58
5.3	Bland-Altman plot comparing the 30 mm strain gauge % strain reading with % strain calculated via two 30 mm digital extensometers placed in the speckle pattern on either side the strain gauge in DIC post-processing. Data is from the strain validation test completed at the third of three batch experimental testing events, 28 November 2023.	59
5.4	Dent depth measured with an inspection line in VIC-3D 9. The top portion shows an inspection line drawn across the panel that passes through the dent centre. Scale is indicating surface profile in z-direction (out-of-plane) from 0 mm (purple) to -2.4 mm (red). The bottom portion shows the extraction graph of that inspection line in a plot of z (mm) vs the in-plane horizontal coordinate, x (mm). Dent edges used for depth measurement are marked with black lines.	63
5.5	Vertical strain, e_{yy} , and four 30 mm extensometers (E0, E1, E2, and E3) with extraction data strain vs. index (frame) plot are shown for test panel 2023-003 at 7.5 kN load. The 7.5 kN load occurs at index (frame) 88, marked with a small black dot on the strain-index plot.	66
5.6	Force-displacement CAI Performance. Force and displacement are measured by and collected from the MTS compression apparatus.	69
5.7	Zoomed view of the differentiation area for force-displacement CAI Performance presented in Figure 5.6.	70
5.8	Centre dent deformation. Black identifies flat facesheet. White identifies a dented area of at least 0.25 mm depth. The scale bars are 50 mm. The white vertical line marks the panel centre.	72
5.9	60 mm ED dent deformation. Black identifies flat facesheet. White identifies a dented area of at least 0.25 mm depth. The scale bars are 50 mm. The white vertical line marks the panel centre.	73
5.10	50 mm ED dent deformation. Black identifies flat facesheet. White identifies a dented area of at least 0.25 mm depth. The scale bars are 50 mm. The white vertical line marks the panel centre.	74

5.11	40 mm ED dent deformation. Black identifies flat facesheet. White identifies a dented area of at least 0.25 mm depth. The scale bars are 50 mm. The white vertical line marks the panel centre.	75
5.12	CAI failure mode variations of dented sandwich panels. Variation (i) is characterized by outward deformation of the damaged facesheet in addition to the inward deflection in the dent area. Variation (ii) is characterized by having only inward deflection of the damaged facesheet. Outward deflections (positive Z) are circled in red. Inward deflections (negative Z) are boxed in blue.	77
5.13	CAI failure mode on the back facesheet were all very similar. The facesheet deformed outward in a Euler macrobuckling manner (see Figure 3.2 (a)). but the knife edge prevented full outward deformation at edged. In the foreground, a mark made by the rear knife edge onto the panel is visible.	78
5.14	Vertical Lagrangian strain, e_{yy} , behaviour of test panel 2023-004 is shown using a 16 colour gradient representing 0 to -4% strain. The 14 images capture every 25 seconds of the test (every 50 frames at 2 Hz). The net section yield force occurs in frame 276. The peak load occurred in frame 478.	81
5.15	Centre dent strain. Black identifies area in plastic strain while white identifies areas under elastic strain. Scale bars are 50 mm. The vertical white line marks the panel centre.	82
5.16	60 mm ED dent strain. Black identifies area in plastic strain while white identifies areas under elastic strain. Scale bars are 50 mm. The vertical white line marks the panel centre.	83
5.17	50 mm ED dent strain. Black identifies area in plastic strain while white identifies areas under elastic strain. Scale bars are 50 mm. The vertical white line marks the panel centre.	84
5.18	40 mm ED dent strain. Black identifies area in plastic strain while white identifies areas under elastic strain. Scale bars are 50 mm. The vertical white line marks the panel centre.	85
5.19	Observed asymmetry for 40 mm, 50 mm and 60 mm ED panels in strain distribution following peak load. The centre dent panels do not show asymmetry. Elastic strain areas are coloured white while plastic strain areas are coloured black.	86
5.20	Stress-strain CAI performance. Stress is calculated using load cell data. Strain is calculated using DIC average e_{yy} data.	88
5.21	Zoomed view of the differentiation area for stress-strain CAI performance presented in Figure 5.20.	88
6.1	Facesheet wrinkling was observed near the top edge of the undamaged test panel, in the unsupported section at loads above 80 kN.	91

6.2	Residual strength distribution of for all tested panel. The results are averaged for each configuration. The error bars represent the standard deviation. Sample sizes of 3 and 1 are indicated in square brackets.	95
6.3	Change in average dent area for each configuration. The error bars represent the standard deviation. Data used for this Figure is available at Table B.1.	96
6.4	Dent area and width measurement performed in ImageJ.	97
6.5	Average dent area at peak force demonstrates a linear relationship for the 40 mm ED, 50 mm ED, and 60 mm ED dented panels tested. The error bars represent the standard deviation.	98
6.6	Change in average dent width for each configuration. The error bars represent the standard deviation. Data used for this Figure is available at Table B.1.	98
6.7	Displacement at peak load all tested panel. The results are averaged for each configuration with displacement normalised to the displacement at a 5 kN pre-load to minimise the effect of test apparatus and test panel settling. The error bars represent the standard deviation. Sample sizes of (3) and (1) are indicated. Data used for this Figure is available at Table B.2.	99
6.8	Elastic strain area comparison at net section yield. Error bars represent the standard deviation.	102
6.9	Elastic strain area comparison at peak load. Error bars represent the standard deviation. The undamaged panel had zero elastic strain in the facesheet at peak load.	102
6.10	Stress-strain CAI Performance. Stress is calculated by dividing the force data from the load cell (provided to the DIC computer via an analogue DAC) by the cross-sectional area of the facesheet. Strain is the average facesheet strain from DIC results. A line of best fit was used in Excel to generate the experimental modulus of elasticity with slope 72.7 GPa	104
6.11	Cross sectional view of the manufactured edge of a CH146 Griffon aluminum honeycomb sandwich panel. At the edge, the core is tapered and facesheets are joined together into a laminated aluminum sheet that can be riveted or otherwise fastened to other structural members.	106
A.1	Test Report 18D0202 - 0.500x48x96 Aluminum Sandwich Panel . .	118
A.2	Manufacturer's Certificate, Strain Gauge Type N11-FA-30-120-11 Lot 9008-411.	119
A.3	Calibration Certificate 0432-5870, Dutchess, MTS Model 204.71, Serial 517, expires 9 March, 2024.	119

Nomenclature

Abbreviations

.csv	Comma-Separated Values (file type)
2D	Two-Dimensional
2D DIC	Two-Dimensional Digital Image Correlation
3D	Three-Dimensional
3D DIC	Three-Dimensional Digital Image Correlation
ASTM	American Society for Testing and Materials
CAI	Compression After Impact
CI95	Confidence Interval of 95 %
DAQ	Data Acquisition System
DIC	Digital Image Correlation
DND	Department of National Defence
ED	Edge Distance (damage centre to panel edge)
Excel	Microsoft Excel (software)
FEA	Finite Element Analysis
ICA	Instructions for Continued Airworthiness
ISO	International Organization for Standardization
MEK	Methy Ethyl Ketone
MMPDS	Metallic Materials Properties Development and Standardization
RMC	Royal Military College of Canada
SBKF	Shell Buckling Knockdown Factor Project
SD	Standard Deviation

SF	Safety Factor
SRM	Structural Repair Manual
USB	Universal Serial Bus
WW2	World War II

Symbols

ϵ	Strain
μ	Mean of a data set
σ	Stress
e	Lagrangian Strain (3D DIC)
i	Value in a data set
N	Number of points in a data set
A	Area
E	Modulus of Elasticity
F	Force
t	Thickness
W	Width
x	Coordinate for horizontal in-plane direction
y	Coordinate for vertical in-plane direction
z	Coordinate for out-of-plane direction

Subscripts

c	Compressive
eng	Engineering
$exp.$	Experimental
t	Tensile
y	Yield
yy	Vertical direction

1 Introduction

Honeycomb sandwich panels are a widely used structural composite panel that offers exceptionally high stiffness and strength-to-weight properties. As with many high-performance composite materials, they were originally cost prohibitive for many use cases; however, they are now widely used in aerospace, automotive, and marine applications [1, 2]. In aerospace, sandwich panels are used for load bearing designs in fixed-wing and rotary-wing aircraft as floorboards, interior panels, exterior panels, and even as main structural members, such as left hand and right hand main beams in the Bell 412 helicopter. Sandwich panels are characterized by two thin facesheets sandwiching and adhered to a thin and light core material as shown in Figure 1.1. Facesheets are often made of metal or fibre-reinforced polymer materials. Core materials are often made of a foam or a periodic structure, such as a honeycomb structure. Other skin and core structures exist; however, these are not common in aerospace applications.

Weight minimisation is an important design criterion in all aerospace designs. For this reason, sandwich panels are designed with thin facesheets and low-density cores that, once adhered together, provide the desired stiffness and

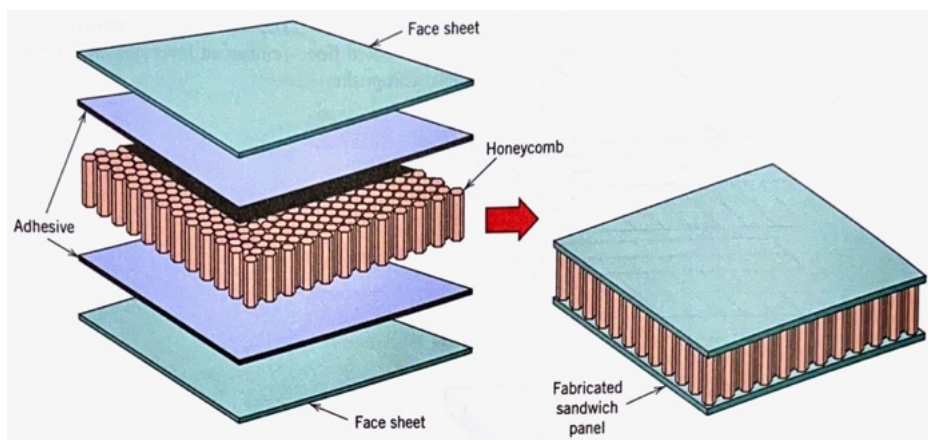


Figure 1.1: Basic sandwich panel construction [3].

strength-to-weight properties. In a similar manner as the web and flanges of a traditional I-beam work in a complementary manner to carry bending, tension, compression, and shear loads along the beam's axis, sandwich panel skins and core material work in a complementary manner to carry loads along the panel's plane. However, light and thin material design used for sandwich panel design makes the composite inherently vulnerable to out-of-plane low-velocity impact damage [4].

Noor, Burton, and Bert assert that the concept of sandwich constructions, of which sandwich panels are a subset, dates back to at least Fairbairn in 1849 in his account on tubular bridges [5, 6]. However, early mass production of a sandwich composite in an aerospace application was first achieved on the DeHavilland DH.98 Mosquito aircraft, the fastest fighter-bomber of World War II [7, 8]. Balsa wood was laminated between two veneer sheets and used, at least in part, as a result of a shortage or other materials. Sandwich construction, even with these relatively low-performance materials, allowed for strength and stiffness-to-weight performance that could not otherwise be achieved with these low-cost materials. Following World War II and the success of the Mosquito, more advanced sandwich constructions were developed. In the postwar years, there was a surge in sandwich panel research and development, including aluminum facesheets and honeycomb core materials. Sandwich panels remain a prevalent high-performance solution for applications requiring stiff and strong panels with minimal weight [2, 9].

1.1 Motivation

Sandwich panels used in aerospace applications have always aimed to minimise weight while providing the required stiffness and strength. With the reduction of material and the optimisation of the design, the strength-to-weight ratio has improved; however, sandwich constructions remain susceptible to damage from low-velocity impacts. Low-velocity impact damage occurs when a foreign object hits the facesheet with enough energy to deform the facesheet and the core of the sandwich panel without puncturing the top facesheet. This damage can be caused in normal aircraft operations such as when rocks or birds strike the outside of an aircraft fuselage and when equipment is mishandled when being loaded or unloaded into an aircraft cargo or cabin compartment. Similarly, low-velocity impact damage can occur during maintenance operations when tools are dropped and equipment hits the aircraft fuselage.

To balance safety, economy of operation, and operational capability, most aircraft designed after 1978 have been designed to damage tolerant design philosophy and standards [10]. To operate safely as a damage tolerance-based design, each aircraft type must have inspection instructions, damage limits, repair instructions, and replacement procedures for each of its structural components. In the case of sandwich structures, this includes designing for low-

velocity impact damage, approving serviceability limits, and providing repair and/or replacement instructions. The details of specific aircraft serviceability limits, repair instructions, and replacement instructions are almost always subject to intellectual property restrictions and therefore specific aircraft limits are not presented in this paper.

The Department of National Defence (DND) operates several aircraft fleets that have honeycomb sandwich panels, including the ageing CH146 Griffon helicopter, which was first delivered to the government of Canada 30 years ago in 1994 [11]. The operational and financial costs of sandwich panel-related repairs and in-service support engineering are significant. The DND, seeking to improve the operational availability of its aircraft and reduce operating costs, has sponsored research at the Royal Military College of Canada (RMC) that supports an improved prediction of the residual strength of the low-velocity impact-damaged sandwich panels. An improved understanding of the residual strength of damaged sandwich panels helps ensure the safety of passengers and crew, as well as the security of the aircraft and its cargo. In addition, it helps reduce the cost of repairs and maintenance.

The RMC research group is conducting academic research to support the development of an analytical model to predict the residual strength of damaged sandwich panels. The model is intended to be able to predict residual strength based on a number of factors such as the size and shape of the dent, the interaction between multiple dents, and the interaction between the dent and the edges of the panel. This thesis presents experimental methodology, results, and analysis on dent and panel edge interactions that will be used to help validate the model.

1.2 Overall Approach and Constraints

The goal of this thesis is to characterize edge distance effects for damaged panels. Damage edge distance is represented in Figure 1.2. Damage edge distance characterisation is achieved through an experimental test. Compression After Impact (CAI) tests are selected as a means of testing residual strength as they are an industry standard for testing laminate polymer matrix composites and structural composite sandwich panels [12–15]. CAI tests of laminate sheets, described in ASTM 7137 for example, differ from CAI sandwich panel testing described in ASTM 8287 mainly in the acceptable range of thickness of the test panel / sheet, but also in test panel size. Both test standards lightly clamp the test panel at their top and bottom edges and provide vertical edge support for out-of-plane movement, while the top and bottom edges are compressed towards one another. For laminate polymer matrix composites, ASTM D7137 specifies 100 by 150 mm test panels of between 4 and 6 mm thick. For sandwich panels, ASTM D8287 specifies 215 by 265 mm test panels of any representative constant thickness.

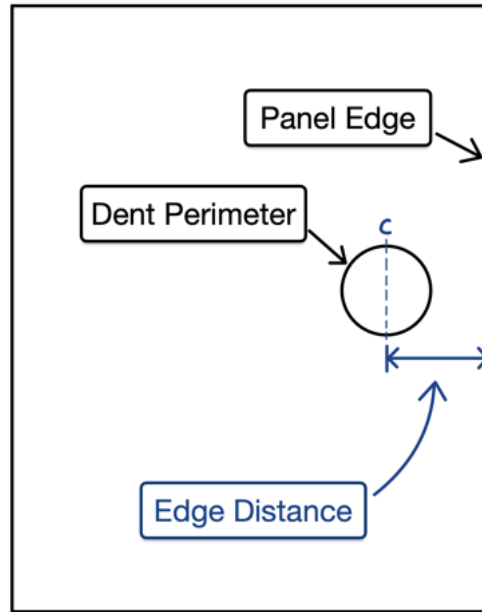


Figure 1.2: Sketch of damage edge distance, the distance between the centre of the dent and the closest edge of the panel.

Unlike CAI, bending tests on sandwich panels are extremely difficult and expensive to perform [16]. They require a large volume of material and are particularly difficult to implement. Although bending loads may be the most critical load design in many applications, the critical component load on a sandwich panel created by pure bending loads is on the facesheet in compression. For this reason, engineers can use much of the data collected in CAI tests when designing a sandwich panel with bending as a critical load case.

ASTM D8287 specifies that strain gauges be placed in the far-field strain area of each test panel, however, unlike the physical constraint of individual strain gauges, Digital Image Correlation (DIC) can be used to provide full-field facesheet strain information during CAI testing. This thesis demonstrates a novel approach using DIC to measure far-field strain in CAI testing as opposed to the individual strain gauges specified in the ASTM D8287 standard. In addition to traditional DIC capabilities, three-dimensional digital image correlation (3D DIC) can be used to collect surface profile and surface deformation data from the facesheet during the CAI testing. 3D DIC-collected data will be combined with the load and displacement data collected during CAI tests to characterize the effects of the damage edge distance in sandwich panels.

Problem statement. The effects of damage edge distance on the residual strength of metallic honeycomb sandwich panels are not well understood. The effects of damage edge distance will be characterized via CAI tests in three

ways:

- Residual strength will be measured as the peak compressive load.
- Deformation behaviour will be characterized by quantifying changes in the dent area and depth and describing the failure mode of the test panel.
- Facesheet strain behaviour will be characterized by measuring and analysing the full-field strain on the damaged facesheet.

In addition to characterizing damage edge distance effects, the 3D DIC-collected and analysed data will be compared with traditional and alternate data sources. The strain results from DIC will be compared with the results of a strain gauge. Initial dent depth and width measurements taken by hand using traditional instruments before CAI testing will be compared with the results of the facesheet models generated by 3D DIC.

1.3 Outline

Chapter 2, Background, presents a technical explanation of metallic honeycomb sandwich panels, their place within the many types of sandwich constructions, their design process, and an overview of in-service damage implications. This chapter also provides a technical summary of DIC and the differences between 2D DIC and 3D DIC.

Chapter 3, Literature Survey presents prior academic works and standards relevant to characterizing the effects of damage edge distance of the metallic honeycomb sandwich panels including foundational sandwich panel research, recent trends in sandwich panel research, and works on damage edge distance. Finally, this chapter also considers the use of 3D DIC in academic research and substantiates the academic value of damage edge distance research.

Chapter 4, Methodology, presents in detail the approach taken in developing a novel approach to damage edge distance effect characterisation. The entire process from test panel fabrication to DIC to CAI testing to data post-processing is presented.

Chapter 5, Results presents all results including the experimental results from CAI tests as well as the quality control results from test panel fabrication, 3D DIC calibrations, and post-processed data.

Chapter 6, Discussion, Analysis and Recommendations, explains the reasoning behind the results. In addition to detailed analysis of residual strength, deformation behaviour and strain behaviour, fabrication and CAI quality control is analysed to understand confidence in results and potential experimental sources of error. Recommendations for further research and process improvements are made throughout.

Chapter 7, Conclusion, states all the conclusions identified from this work.

2 Background

Although most commonly used for flat and curved panels, the basic sandwich construction model can be used to make a number of light-weight structures that serve different purposes depending on the design needs. Sandwich constructions can usually be classified as plates (panels), beams, or shells; however, these classifications are not necessarily discrete; rather, they describe regions on a spectrum. Plates are characterized by having moderate to no curvature and being connected to other structural members at all edges. Beams are similarly flat or near-flat but are usually long relative to their width and are usually unsupported along their length. Shells are significantly curved up to and including cylindrical and dome shapes [17].

Sandwich constructions are designed to transfer loads (nondestructive) and/or absorb energy (destructive). Load transfer applications take advantage of the high stiffness and strength-to-weight properties of sandwich constructions to carry operational loads at minimal weight. Importantly, load transfer applications are designed so that the sandwich construction is not damaged while carrying expected operational loads. Energy absorption applications involve designing for an intentional permanent deformation of the sandwich structure in response to a short-duration high-load event. During a one-time load event, such as a vehicle crashing into a barrier, the lightweight and strong sandwich construction absorbs energy as it is compressed and deformed. This plastic deformation consumes energy and attenuates forces that would otherwise be directly transferred to the rest of the vehicle and its occupants [18]. Sandwich constructions used in high-performance vehicles, such as helicopters, can be designed to transfer loads in normal operations and contribute to protecting the occupants by absorbing energy during a crash event. The metallic sandwich panels considered in this paper are primarily used for load transfer. As a result, large plastic deformation is considered to be a failure of the structure. However, some small local plastic deformation(s) of the sandwich panel such as barely visible impact damage in the form of dents is expected.

2.1 Sandwich Structures and Their Components

Sandwich structures consist of two facesheet materials adhered to opposite faces of a core material. This basic design principle allows sandwich structure designers to select from an almost limitless number of materials and geometries for the skin and core materials. Sandwich structure facesheets are usually thin, and materials are traditionally selected for favourable in-plane properties. Core materials and geometries vary greatly. However, they can generally be categorised as stochastic structures (foams) or periodic structures (2-dimensional or 3-dimensional). Both facesheets and cores are discussed further in the following sections.

2.1.1 Sandwich Structure Facesheets

Facesheets in sandwich structures are selected and designed to carry in-plane compression, tensile, and shear loads. As facesheets are thin, application of in-plane compression loads to a facesheets prior to assembly would result in buckling failure at low loads. Buckling failure loads of assembled sandwich structures are much higher than those of the facesheets in isolation.

Aluminum and fibre-composite skins are common skin materials for sandwich structures in high-performance applications. They are light relative to their in-plane tensile and shear load-carrying capacities. Fibreglass facesheets are also common, but tend to be used in applications less concerned with weight minimisation such as marine vehicles. All three of these materials can be made in a number of thicknesses and shapes depending on the design requirements.

2.1.2 Sandwich Structure Cores

The purpose of most cores in sandwich panels is to maintain facesheet separation by carrying out-of-plane compression and shear loads. Both stochastic (foam) and periodic structure cores come in a number of materials and designs. Figure 2.1 provides an organised list of the cellular structures that sandwich structure designers can consider [2].

Polymeric foams tend to be less expensive and heavier relative to out-of-plane compression and shear strength than periodic structures. Metallic foams are not widely used and are not necessarily less expensive than periodic structures. Foams, particularly closed-cell foams, trap or restrict air movement and tend to have thermal insulation properties superior to those of periodic structures. Similarly, stochastic closed-cell structures can have an advantage in marine applications because they do not allow moisture to travel between cells.

3D periodic structures are not widely used, as they are relatively new, with several configurations that are particularly complex and expensive to

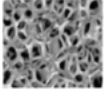
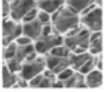




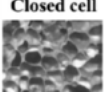









Cellular structures					
Stochastic structures		Periodic structures			
Foam		2D		3D	
Metal	Polymeric	Honeycomb	Prismatic	Truss	Textile
Open cell 	Open cell 	Hexagonal 	Triangular 	Tetrahedral 	Diamond 
Closed cell 	Closed cell 	Square 	Diamond 	Pyramidal 	Diamond collinear 
		Triangular 	Navtruss 	3D Kagome 	Square 

Figure 2.1: Classification of cellular structures used in sandwich panels [2].

manufacture at scale. Like foams, 3D periodic structures can be designed to permit or restrict air and moisture propagation [2]. That said, 3D-printed components without 100% infill can also be considered a sandwich structure in some sense: the infill material serves the function of the core and the outer layers of the print act as facesheets. These infill patterns often fit the definition of 2D and 3D periodic structures. Figure 2.2 shows a number of 3D printed infill patterns that can be selected based on design needs and preference. In practice, infill is almost always completely hidden in the final product.

2D prismatic cells are relatively easy and inexpensive to manufacture, but do not provide particularly strong out-of-plane load-carrying capabilities when compared with other core designs. 2D prismatic cells are the most widely successful and available commercial sandwich construction. This design is used as the basis for the completely recyclable and ubiquitous corrugated cardboard. Figure 2.3 shows the three main components of corrugated cardboard; two liners and a medium.

2D honeycomb cell structures are widely used in applications demanding exceptional strength and stiffness-to-weight properties such as aerospace. The hexagonal honeycomb pattern is by far the most common honeycomb configuration and is most commonly the implied pattern when referring to honeycomb sandwich panels. The honeycomb core is made of many ribbons that have been formed and adhered to each other to create the hexagonal cell pattern (also because beeswax honeycombs are hexagon-based). The structure of the hexagonal honeycomb is regular and symmetric, characterized by a ribbon direction. Figure 2.4 provides a detailed view of the honeycomb core structure. The cell walls are of the same thickness as the ribbons, except for the cell wall



Figure 2.2: Various 3D printed part infill patterns are used to provide structural support to outer layers of filament-printed components. Infill patterns, like more traditional sandwich core materials, are normally selected based on design needs [19].

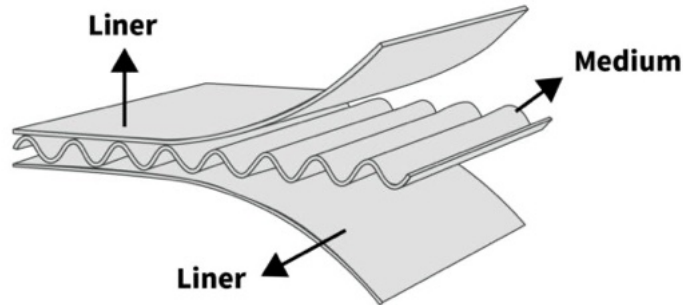


Figure 2.3: Detailed view of single wall corrugated cardboard using a 2D prismatic design approach. In this industry, facesheets are called liners and cores are called medium [20].

in the ribbon direction, which has twice the thickness of the other cell walls. The smallest repeated element in the honeycomb pattern, marked in bold in Figure 2.4, consist of three half-cell walls intersecting at 120° from each other.

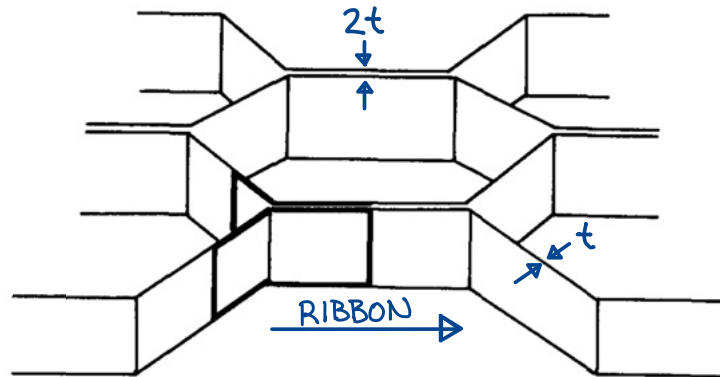


Figure 2.4: Detailed honeycomb core cell view showing ribbon direction and repeated element consisting of three half-cell walls, two of thickness t and one of thickness $2t$ (ribbon direction). Figure adapted from Wierzbicki et al. [21].

2.2 Sandwich Panel Design

The geometry and construction of the sandwich structure (facesheet material selection, thickness and layout, adhesive selection, thickness and curing process, and core selection, geometry, density, and thickness) significantly affect the characteristics of sandwich panels [22–24].

Sandwich panel design considerations include the following:

1. The required mechanical properties of the sandwich panel including strength, stiffness, and safety margins;
2. The required thermal properties of the sandwich panel, as needed;
3. The required vibration damping properties of the sandwich panel, as needed;
4. The importance of weight minimisation;
5. Environmental conditions including potential in-service damage types, temperature, moisture, and corrosives (saltwater environment, etc.);
6. Selection, fabrication, and sizing of facesheet materials, ensuring that they have sufficient stiffness for expected tensile, compressive, and shear stresses;
7. Selection, fabrication, and size of the core, including type of core, thickness of the cell wall, and the resulting density of the core so that the anticipated shear stresses can be carried safely and core crushing is prevented;
8. Adhesive selection, sizing, and curing procedure;
9. Final sandwich panel properties such that the stiffness of the core and the compressive strength of the facesheet do not permit facesheet wrinkling, the core cells are sized to prevent inter-cell buckling of the facesheet, and the sandwich structure does not deflect excessively under applied loads [25];

10. Installation, including joining and fastening of the panel to adjacent structures taking into account the transfer of loads and the ease of assembly;
11. Manufacturing costs, including materials, fabrication, and certification;
12. Fabrication process;
13. In-service inspection, repair, and replacement requirements, procedures, and costs; and
14. Testing and validation to ensure that the design meets the design specifications.

2.3 Continued Airworthiness of Sandwich Panels in Aviation

Instructions for Continued Airworthiness (ICA) are required for all civilian aircraft flying under the authority of Canadian or American aviation authorities [26, 27]. ICAs contain serviceability limits for aircraft components which, in the case of an aircraft with sandwich panels, includes damage limits. These damage limits define under what conditions a sandwich panel is considered and is not considered airworthy. In conditions where a sandwich panel is not considered airworthy, a maintenance action is required before the aircraft can be returned to operational service. This would normally include a further inspection and either repair or replacement of the component. Standard Repair Manuals (SRM), which are part of the ICA, detail approved instructions for the repair of structural components.

When ICA are developed or changed, the decision is substantiated by a documented technical data package. Both the ICA and the supporting technical data package are often subject to intellectual property limitations. No ICA free of intellectual property limitations are available to be included in this paper; however, this author is familiar with multiple ICA for aircraft with sandwich panels. In general, the following may be included in ICA for sandwich panel components:

1. A frequency and means of inspection will be defined;
2. Small surface damage that is smooth and of very small depth will be defined as negligible;
3. Inspection for disbond of the facesheet from the core will be a major criterion. Disbonded panels will need to be repaired or replaced;
4. Some level of smooth dents on the facesheet will be permissible provided one or more of the following:
 - a. The dent depth is below a certain threshold;
 - b. The dent diameter (maximum measurable) is below a certain threshold;
 - c. The total dent area within a panel is below a certain threshold; and

- d. The proximity of the dent to the edges of the panel or to fixtures in the panel is above a certain threshold.

To ensure airworthiness, each limit prescribed in the ICA must be substantiated through sound engineering. When there is a lack of data available to engineers who are building and developing technical data packages, they must adopt a conservative approach to ensure airworthiness. These necessary areas of conservatism provide an opportunity for further research. As research is performed and additional data are available for consideration, ICA can be revised and improved accordingly.

2.4 Digital Image Correlation

DIC is an image-based non-contact strain and deformation measurement technique. DIC applications include materials testing, structural analysis, and biomechanics. At its core, the image analysis technology involves identifying pixel subsets on a surface captured in a reference image and then locating the same pixel subsets in subsequent images. The subsets of pixels in the subsequent images are correlated with their location in the reference image to determine any deformation or strain that occurred. Modern DIC tracks not only the movement of pixel subsets, but also the deformation of the pattern within the subset itself, by having subsets overlap with each other [28]. An illustration of the identification and comparison of subsets is presented in Figure 2.5.

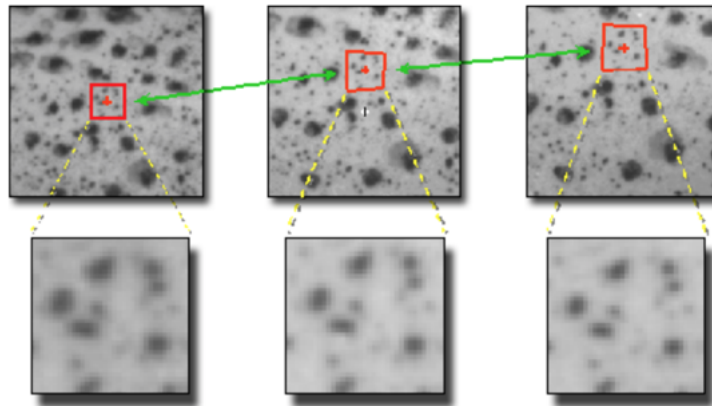


Figure 2.5: Illustration of a DIC pixel subset captured and identified in the images [28].

The amount of overlap between subsets is defined by the subset size and the step size, both measured in pixels. The size of the subset is the dimension of the unique pixel patterns (height and width) that are being tracked. The

size of the step is the distance between the start of sequential subsets. For example, a DIC analysis with a subset size of 24 pixels and a step size of 12 pixels will have the next subset start halfway across the first subset resulting in a 50% overlap between adjacent subsets.

As shown in Figure 2.5, the surface being measured must allow unique subsets to be defined in the reference image and their identification in subsequent images. Several factors other than the software used affect this ability, including surface finish, lighting, camera(s), and lenses. A random speckle pattern such as the one shown in Figure 2.5 is almost always created or applied to the surface.

2.4.1 2D DIC

Two-dimensional DIC uses a single camera to capture all images. Provided satisfactory speckle pattern, lighting, camera, and lens settings are present, deformation and strain in the camera plane can be calculated. Out-of-plane movement, either as deformation or strain, cannot be measured with a single camera.

Modern DIC software, such as VIC-Snap and VIC-3D 9 software used in this research, perform additional processing to basic deformation and strain calculations. Importantly, strain results are analysed for unreasonable variation in strain values between adjacent subsets. Sufficiently high and concentrated strain gradient areas undergo data smoothing with the intention of correcting for errors in image correlation.

2.4.2 3D DIC

Three-dimensional DIC uses two cameras with shared fields of view to capture image pairs. With a second camera, additional image correlation functions can be performed. That is, each subset can be triangulated using the stereo camera system. This triangulated subset information permits the calculation of the strain and deformation in three dimensions. This means that not only can deformation and movement (translation and rotation) be calculated in three dimensions, but also that surface strain can be calculated in any plane that exists in both cameras' field of view. This is particularly useful for curved and multi-surface objects.

It is important to note that 3D DIC systems can be expanded to more than two cameras with multiple cameras capturing the entire perimeter of a test specimen. This is what Gardner et al. performed for NASA's Shell Buckling Knockdown Factor Project (SBKF) where multiple cameras were used to measure strain and deformation on the entire outer surface of a cylindrical structure [29]. See Figure 2.6 for a diagram for the SBKF 3D DIC setup.

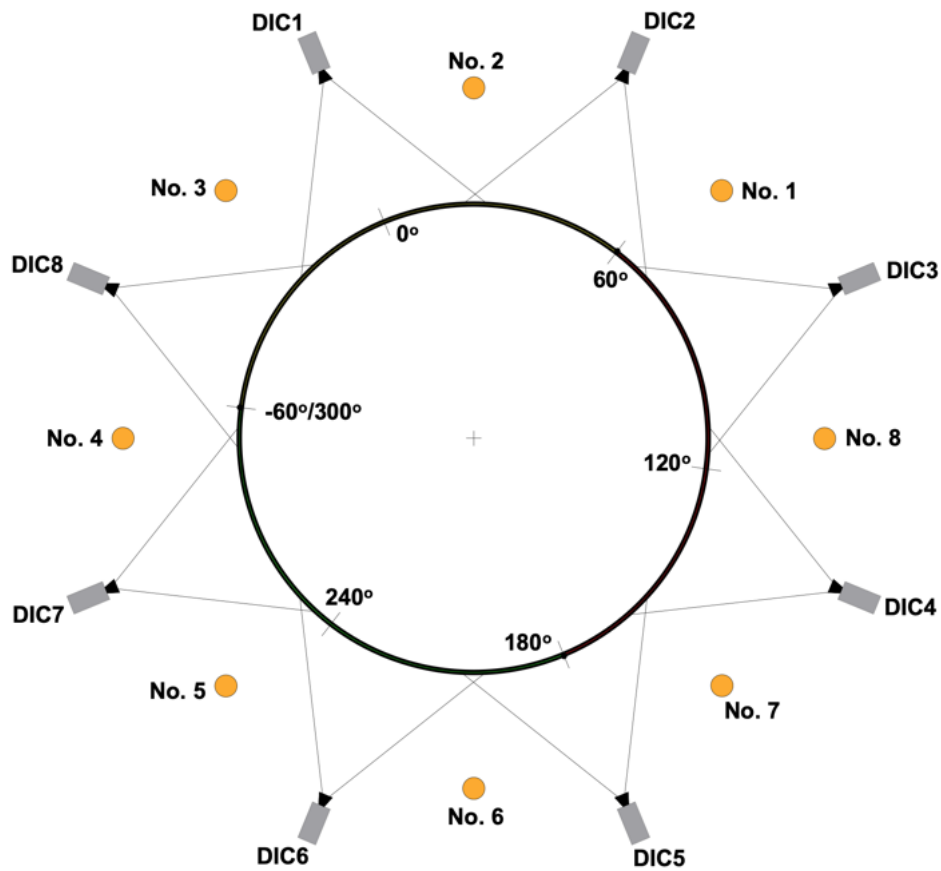


Figure 2.6: Diagram showing a top-down view of the SBKF 3D DIC test setup. Eight vertically-separated 3D DIC cameras pairs each capture 45° of the SBKF cylinder to provide surface strain and 3D deformation data for the entire outer surface [29].

3 Literature Survey

3.1 Foundations of Sandwich Panel Research

As stated in Chapter 1, the first academic work on sandwich constructions dates back to at least Fairbairn in 1849 [6]. The first major use of sandwich constructions in aviation was with the use of balsa wood core and veneer facesheets in the very successful DeHavilland DH.98 Mosquito developed and first employed during World War 2 (WW2) [7]. Following WW2 in the 1940s and 1950s, there was a significant increase in sandwich panel research with the first theoretical works being published. Hoff et al. performed and published some of the first buckling analysis of sandwich panels in the 1940s [30]. This period also included the development of new constructions primarily for the aerospace industry, including metallic sandwich panels and honeycomb cores [31]. Honeycomb cores with hexagonal cell shapes offered the best performance (shear and stiffness to weight) when they were first developed and continue to be a very high performing configuration for sandwich panels.

Honeycomb core research continued through the remainder of the 20th century. Notable research related to metallic honeycomb sandwich panels included McFarland's 1963 journal article that presented an analytical model to determine the mean crushing stress of the hexagonal core subjected to axial load [32]. Wierbicki further developed a method for determining the crushing strength of hexagonal cell structures by including considerations of both energy and plasticity [21].

In the same period, metallic honeycomb sandwich panels were adopted for commercial use, particularly in aviation. The Bell UH-1 military helicopter (the civilian variant is the Bell 212), which was first flown in 1968, uses metallic honeycomb sandwich panels for interior and exterior load bearing panels, including the tailboom [33].

3.2 Recent Sandwich Panel Research

Sandwich panel research has remained an active field, partly driven by academic interest in the development of new structural designs and analysis models, the development of new materials suitable for sandwich constructions, the

development of new manufacturing technologies, and by industry interests. As shown in Figure 2.1, there are several new core cell structures (metallic foams, complex 3D periodic structures, etc.) that were simply not feasible to create with the 1940s technology. Manufactured sandwich panels used in aviation, first made with balsa wood and veneer, were largely replaced by metallic sandwich panels. With significant advancement in fibre-reinforced polymers, sandwich panels made with fibre-reinforced polymer facesheets have become increasingly popular and cost-effective [2, 34].

Commercial and government use of sandwich panels in aviation has generated significant interest in the impact resistance and residual strength of damaged sandwich constructions. Manufacturers and standardisation organisations have developed standardised testing protocols to test sandwich panels, namely in compression, against projectile impact, and bending. Compression test standards include ASTM C364 for undamaged sandwich panels, and ASTM 8287, ISO 18352:2009, and Boeing’s BSS 7260 for damaged sandwich panels [13, 14, 35]. Projectile impact standards include a number of drop-weight and quasi-static indentation methods such as ASTM 7137 and ASTM 7766 [12, 36]. Bending standards include the long beam flexure standard, ASTM 7249 [16].

Effects of Smooth Dent Damage on Sandwich Panels Subjected to Edge-Wise Compression

The effect of smooth dent damage on edge-wise compression of sandwich panels is a main topic of research in the RMC research group along with shear as these are thought to be the most representative critical loading modes for dented sandwich panels. Dents are damage to the sandwich panel caused by contact with a foreign object that deformed the facesheet and the underlying core without puncturing the facesheet. They are normally categorised as smooth when the dent curvature is gradual with no creases or sharp curves, or sharp when the dent curvature is severe or there is a crease or fold in the dent. The edge-wise compression test of damaged sandwich panels is most often referred to as the compression after impact (CAI) test. Schubel et al. highlighted the particular sensitivity of sandwich panel CAI strength with composite facesheets to delamination (internal separation of composite facesheet layers) [37]. Similarly, many aircraft ICA consider disbond (detachment of the facesheet from the core) as the most important internal sandwich panel damage mechanism, as it also greatly affects the residual strength of the sandwich structure [38]. Both delamination and disbond can be created by surface impacts on sandwich panels. Disbonds are not usually allowed and require immediate panel repair or replacement.

Horrigan et al. showed that in CAI tests, the critical loading force required to initiate failure is a function of both the core damage area and the dent depth [39]. Boctor used simulated edge-wise compression tests to predict the effect of multiple smooth dents on sandwich panels [40]. Deeper dents were found

to affect the residual strength of the panels in the simulations, as Horrigan et al. showed experimentally. Sufficiently separated dents were found to behave individually, while sufficiently close dents were found to interact with each other.

Both Ye et al. and Tariq et al, [41, 42] also performed CAI tests for dented metallic sandwich panels however their dents were made in a quasi-static manner using small impactors that created relatively deep and narrow dent profiles that are not easily compared with smooth dents with a shallow depth relative to their width. In an aircraft maintenance context, these dents would be characterised as sharp dent (more severe) as opposed to smooth dent. Furthermore, Tariq et al. [42] did not adopt vertical edge supports to prevent macrobuckling, as is normally included in the CAI test standards.

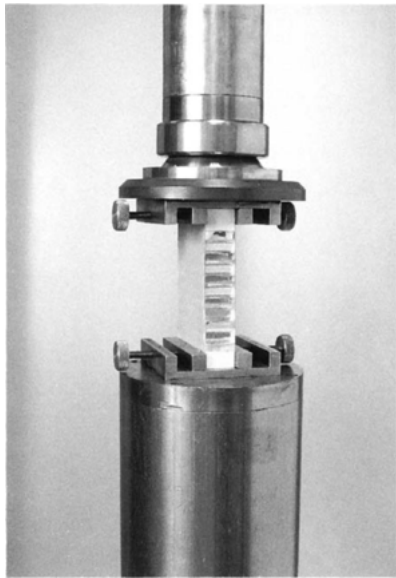
Column Buckling Behaviour of Sandwich Panels Subjected to Edge-Wise Compression

Edge-wise compression of sandwich panels is a well-established test method with variations including, but not limited to, ASTM C364, which tests short undamaged specimens with free vertical edges (simple-clamped), and ASTM D8287, which tests larger specimens with supported vertical edges and is designed to test the residual compressive strength of damaged panels [13, 35]. Figure 3.1 presents a simple comparison of the two general approaches. An alternative standard with vertical edge supports for testing damaged panels is ISO 18352:2009 however, the coupon size is smaller. In addition to the standards controlled and published by standardisation organisations, manufacturers provide their own recommendations for testing sandwich panels such as the Boeing Specification Standard (BSS) 7260 which is closely linked to the ISO 18352:2009 [14, 15].

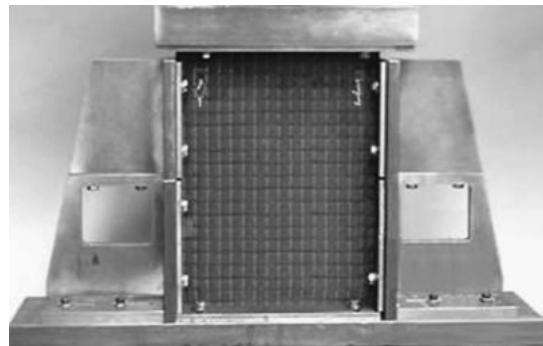
Fleck and Sridhar tested sandwich panels subjected to edge-wise compression and developed analytical models for axial strength [44]. They characterize four failure modes for edge-wise compression including (a) Euler macrobuckling, (b) core shear macrobuckling, (c) facesheet microbuckling and (d) face sheet wrinkling as illustrated in Figure 3.2. The same edge-wise compression failure modes, along with bending and face-wise compression failure modes, are described in the Hexcel technical manual for honeycomb sandwich design technology [45].

The purpose of vertical supports (supports to the non-loading edges as shown in Figure 3.1 (b)) present in the test standard for damaged sandwich panels (ASTM D8287, ISO 18352:2009, etc.) is to promote failure of the panel at the damage location. The CAI test of sandwich panels with dented facesheets without vertical supports is likely to result in premature failure due to early macrobuckling. Vertical supports in ASTM D8287 and ISO 18352:2009 are shaped as knife edges (sliding edges). To create the knife edge, an 8 mm thick plate is cut inward from both edges at 45° to form a blunt knife-like

edge (bevelled to a 1 mm radius) that contacts the facesheet perpendicular to the plate. A detailed view of the vertical supports showing the blunt knife edges that are placed against the front and rear facesheets of the test panel on both vertical edges is provided in Figure 3.3. The blunt knife edge geometry minimises vertical support edge surface area in contact with the facesheet and therefore minimises friction while preventing outward out-of-plane facesheet movement. The facesheets at the knife edge can still wrinkle or buckle inward, away from the knife edge support but the overall panel is prevented from moving outward at its edges.



(a) Simple-clamp support fixtures, normally used to test undamaged sandwich panels, have no vertical edge supports [35].



(b) Support fixtures with fixed knife edge supports along the vertical edges of the test are normally used to prevent premature macrobuckling of the panel when testing damaged sandwich panels [43].

Figure 3.1: Comparison of simple-clamped vs supported sandwich panel edge-wise compression test fixtures.

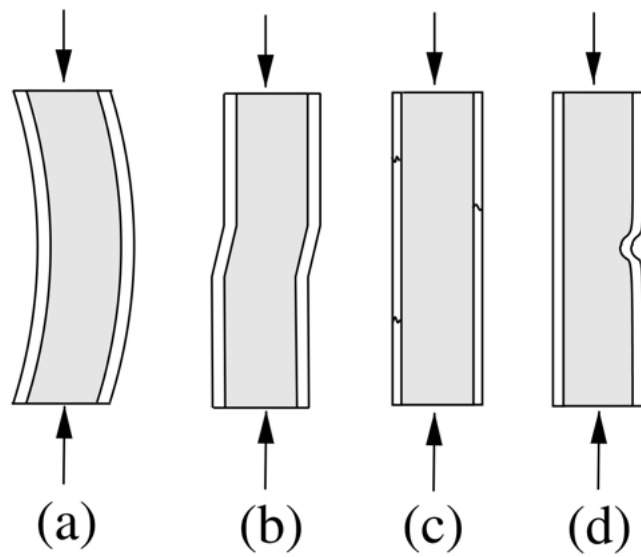


Figure 3.2: Failure modes in sandwich columns subjected to edge compression. In compression tests, columns ends are constrained to in-plane movement. (a) Euler macrobuckling; (b) core shear macrobuckling; (c) facesheet microbuckling and (d) facesheet wrinkling [44].

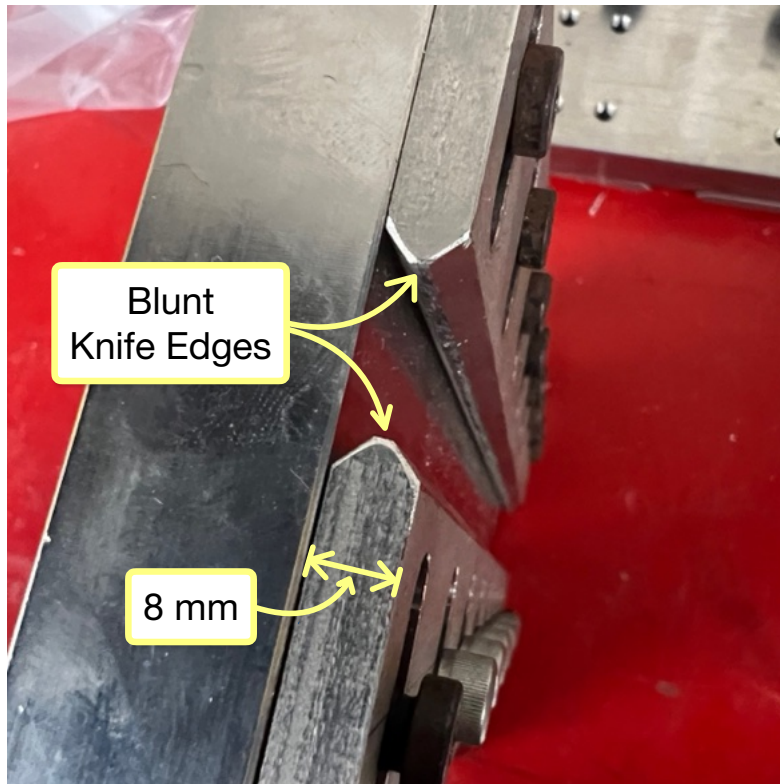


Figure 3.3: Knife edge support component. This near top-down view of the support fixture component shows the front and rear facesheet knife edge supports used to prevent outward movement of the test panel at the vertical edge.

3.3 Sandwich Panel Damage Edge Distance Research

For the purpose of this research, the damage edge distance is defined as the distance between the centre of a damage and the edge of the sandwich panel, as shown in Figure 1.2. This is one of several means of quantifying the proximity of a damage area and a panel edge. For example, edge margin, the shortest distance between the edge of damage area and the panel edge, can also be used to characterize damage to panel edge geometry. Damage edge distance is the term used in this paper.

Boctor et al. refer to the Gulfstream Standard Repair Manual (SRM) prescribing limit for the distance between two dents on a sandwich panel being no less than 101.6 mm (4 inch) [40]. While the Gulfstream SRM is not available to this author due to intellectual property restrictions, it is very likely that similar distance limits would be published for the distance between a dent and a panel edge. Similar limits are known to be published in other SRMs and ICA for other aircraft. For example, this author is familiar with the published limits for the CH146 Griffon helicopter. However, all known limits are subject to intellectual property limitations and cannot be published in an academic paper.

Bouwhuis et al. investigated the edge effects on the compressive testing of periodic cellular metal cores (lattice structure); edge effects were found to be comparatively small, with samples as small as two by two cells wide being representative of bulk cores [46]. Damage edge distance effects are expected to manifest at distances greater than two-cell width.

No articles were found that specifically discussed the effects of the damage edge distance on the residual strength of metallic honeycomb sandwich panels subjected to CAI.

3.4 Use of 3D Digital Image Correlation for Research

ASTM D8287 explicitly states that DIC is not used in the standard because there are no ASTM-accepted calibration methods for DIC systems [13]. However, 3D DIC is a powerful tool set that can generate sufficiently precise strain and out-of-plane deformation data when properly configured for the application and calibrated [28, 29]. Gardner et al. demonstrated with the NASA SBKF project that, unlike traditional linear variable displacement transducers and electrical resistance strain gauges that allow data to be collected only for a select number of point locations, 3D DIC can be used to characterize full field displacement and strain behaviour. As the intent of strain measurement in this research is to characterize strain throughout the facesheet to understand the effects of damage edge distance, the full-field strain results of the DIC system

are more meaningful than the local high-precision results of the individual strain gauges. However, to better align this research with the ASTM D8287 standard, the results of the DIC instrument will be compared with known, trusted, and calibrated measurements provided by a traditional strain gauge.

McQuigg et al. reported using DIC to measure 3D displacement and strain information during CAI tests of nonmetallic sandwich panels; however, this was only done for select panels within their data set that compared CAI results at various impact energy levels [47]. The main benefit of 3D DIC for their research was the ability to quantify the change in size and shape of the damage region during CAI loading. McQuigg et al. found that the dent width (perpendicular to the loading direction) grew with an increase in the CAI load while there was little change in the dent height (in the loading direction) with the CAI load. Importantly, the CAI support fixture described and shown by McQuigg et al. does not appear to have vertical edge supports. It appears that the ASTM C364 standard test method for edge-wise compressive strength of sandwich constructions, which is designed to test undamaged sandwich panels and does not include any vertical edge supports, was used as a basis for the tests.

Wang et al. tested sandwich panels for blast performance, the sandwich panel's response to a blast shock wave striking a facesheet while the panel is under various in-plane compressive loads [48]. To characterise the mechanical response to the blast shock wave, 3D DIC was used to measure the out-of-plane deformation of the rear sandwich panel facesheet in response to the front facesheet being exposed to the shock wave. Undamaged sandwich panel test coupons were tested for their response to blast shock waves at various in-plane compression loads; however, the panels were not supported along their vertical edges.

For the RMC research group, there is a desire to validate finite element simulations of dented sandwich panels subjected to edge-wise compression. Simulations generate full-field displacement and strain behaviour in the facesheet that can be compared with 3D DIC results from experimental tests. At this stage in the development of simulation models, the full-field experimental strain and deformation results from a 3D DIC system are more valuable than the strain values at discrete locations collected from individually placed strain gauges on the facesheet. The DIC results allow for a comparative analysis of the entire facesheet deformation and strain behaviour to the model, as opposed to only the discrete local results from individual strain gauges.

3.5 Research opportunities

Only one published article was found using 3D DIC for CAI testing of damaged sandwich panels, McQuigg et al. [47]. That article did not publish 3D DIC strain information, only changes in dent width and height during CAI. Furthermore, their CAI test fixture did not appear to be compliant with an existing

standard: Most notable, since they were testing damaged panels, no vertical knife edge supports were used and therefore the test coupons were unrestricted from macrobuckling. Knife edge supports are far more representative than unsupported edges of a sandwich panel installed in aircraft as sandwich panels installed on aircraft are attached to supporting structure on all edges. The research performed for this thesis uses the opportunity to significantly improve DIC-collected facesheet deformation and strain information for CAI tests of damaged sandwich panels with edge supports that more closely represent sandwich panels in aircraft.

No articles or academic works were discovered that present the effects of damage edge distance for sandwich panels subjected to CAI. Meanwhile, damage edge distance limits for multiple aircraft's sandwich panels are known to exist, but the technical data packages supporting these limits are subject to intellectual property limitations.

In the RMC sandwich panel research group, an experimental test basis is needed for the validation of the CAI FEA model. 3D DIC-collected facesheet deformation and strain data from experiment CAI tests provide an excellent opportunity to compare results.

In summary, this research on metallic honeycomb sandwich panels focuses on the following goals:

1. FEA model validation. Conduct experimental CAI tests that can be used to validate the FEA models of the RMC research group.
2. Experimental test methodology. Develop an experimental CAI test method for damaged sandwich panels that collects full-field facesheet deformation and strain data using 3D DIC. This improves upon all known metallic sandwich panel research by using 3D DIC in a representative CAI test fixture.
3. Damage edge distance effects. Characterise the effects of edge distance for dented panels under in-plane compression on residual strength, failure mode, and facesheet strain behaviour.

4 Methodology

The overall approach taken was to perform experimental CAI tests of sandwich panel coupons dented at various edge distances. The CAI test methodology is based on ASTM D8287 but adapted for 3D DIC instruments [13]. The test panels were placed in a support fixture compliant with ASTM D8287 and vertically compressed to failure using a fixed displacement protocol. 3D DIC cameras were vertically separated and placed perpendicular to the dented facesheet of the test panel as shown in Figure 4.1 which provides a sketch of the basic CAI test setup.

Several of the test standards were consulted and considered in the development of the test methodology. ASTM D8287 was selected over ISO 18352:2009 as the test samples are physically wider at 215 mm versus 100 mm [13, 14]. For a given dent size, it would have been more difficult to differentiate edge effects from non-edge effect conditions. Details of the sandwich panels purchased are presented, including manufacturer test reports. All material processing for the creation of test panels is presented in detail, including cutting, end potting, damage introduction, speckle pattern technique, and the quality control practices implemented. The methodology for compression after impacts tests, including all systems used, procedures followed, and postprocessing, is also presented.

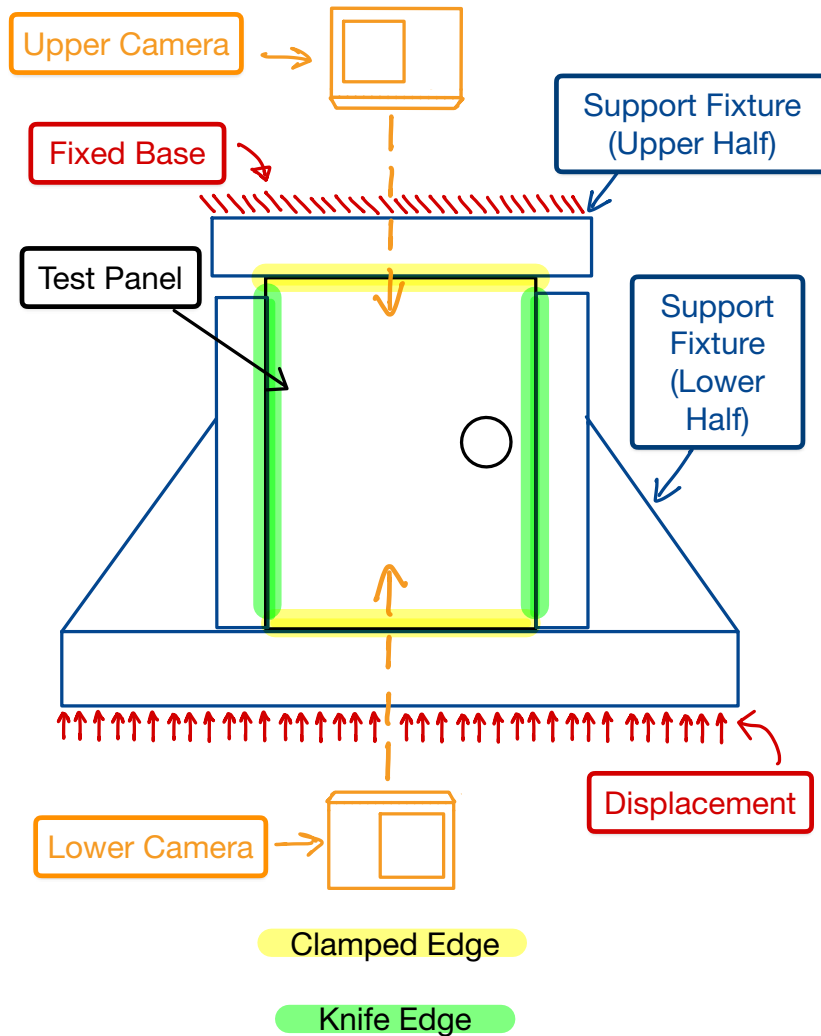


Figure 4.1: Sketch of the basic test setup. The test panel is installed in the two halves of the support fixture with lightly clamped and knife edge supports. Compression is performed vertically. 3D DIC cameras are vertically separated with a clear view of the dented facesheet.

4.1 Standards

4.1.1 Fabrication

The sandwich panels used for this experiment were purchased and delivered with a test report. The test report is available in Figure A.1 in Appendix A. The panels were tested for flatness, thickness, and dry peel strength. Dry peel is a test of the adhesive bonds between the facesheets and the core. ASTM D903 is one of the standard test methods for peel or stripping strength of adhesive bonds [43].

4.1.2 Impact Damage

ASTM D7136, Standard Test Method for Measuring the Damage Resistance of a Fibre-Reinforced Polymer Matrix Composite to a Drop Weight Impact Event, was used as the standard for the design of the drop tower fabricated for this research and used on the test specimens in this experiment [49]. The drop tower is detailed in Section 4.5. ISO 18352:2009 provides an alternative but similar standard [14].

4.1.3 Residual Strength Testing

The compression tests of the undamaged panels can be tested as per ASTM C364 [35]. Damaged panels are commonly tested in compression after impact (CAI) tests. The international standards ASTM D8272 and ISO 18352:2009 were both considered but ASTM D8287 was selected as the preferred option [13, 14]. Data collection was performed via both the compression test apparatus (time, force, displacement) and 3D DIC (image sets and high-resolution deformation data).

4.2 Test Panel Cutting

As the objective of these experiments was to collect data representative of aircraft metallic honeycomb sandwich panels, sandwich panels were purchased in large sheets from a commercial vendor and subsequently cut to size and prepared for CAI testing. Purchasing from a commercial vendor reduced the risk of errors in fabrication and allowed the RMC test panel fabrication efforts to be focused on cutting and end potting.

All test panels used in this experiment were fabricated from a single 1.22 m \times 2.44 m (4 foot \times 8 foot) aluminum sandwich panel purchased in 2019. The sandwich panel facesheets are made of 0.508 mm (0.020 inch) thick 2024-T3-Clad aluminum. The honeycomb core material is 5052 aluminum with a single cell wall thickness (foil thickness) of 0.051 mm (0.002 inch) cut into ribbons and then shaped and adhered together to make 6.35 mm (0.25 inch)

hexagonal cells. The vendor test report, including manufacturing details, is available in Appendix A, Figure A.1.

4.2.1 Rough Cut

The oversized panel coupons were cut from the sheet using a skill saw with a blade of high tooth count to allow for a finer cut. The depth of the blade was set at approximately 16 mm (0.625 inch), only slightly deeper than the thickness of the panel, to minimise the tearing of the facesheet. Painters tape was applied in a single layer to the top surface of the sandwich panel at all locations where the skill saw base was in contact with the panel. This prevented the facesheet from scratching. A long, rigid, and straight aluminum bar was placed and gently clamped to the sandwich panel as a guide edge for all cuts to ensure straight cuts. The cuts were made slowly. The resulting cut edges were quite straight and smooth with no indication of excess heat being generated. This provided a good starting point when making final cuts, helping minimise the oversize dimensions required and conserving material.

4.2.2 Final Cut

The oversized panel coupons were cut to final dimensions using a wet tile saw with a moving base plate and a porcelain cutting blade. The specific model used was a RIDGID 9 amp 7 inch portable wet tile saw with stand, model R4031S [50]. The wet tile saw was tuned for the smooth operation of the moving base plate and the squareness of the guide edge was adjusted. The moving base plate rollers were well aligned. A 0.356 mm (0.014 inch) shim was attached to the guide edge to achieve sufficiently square cuts.

Jigs were made to achieve test panel dimensions of 215 mm and 265 mm consistently. The jigs were designed to be stiff and bolted to the base plate. Once calibrated to the right cut length, all moving parts of the jigs were secured in place. The wet tile saw with a jig installed is presented in Figure 4.2.

When cutting the panel coupons, the emphasis was first on establishing two straight edges 90° from each other. Subsequently, the jigs were used to cut the panel to the final dimensions. The cuts were made slowly and light hand pressure was evenly applied to the moving base plate to minimise loads on the saw frame, the moving base, and the panel coupon. This approach resulted in clean, straight cuts and no damage to the cell walls. The panel coupons were dried in a dehydrator set to 35°C before proceeding. Low-temperature dehydration was performed to remove any humidity from the wet cutting before end potting (which may trap the humidity in the test specimen).

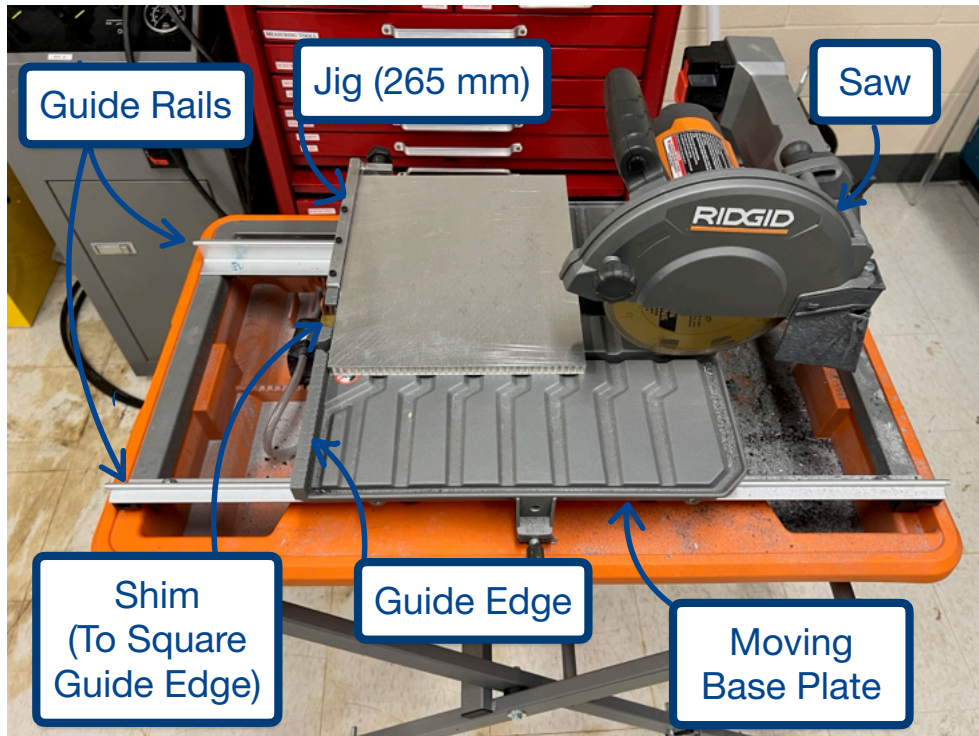


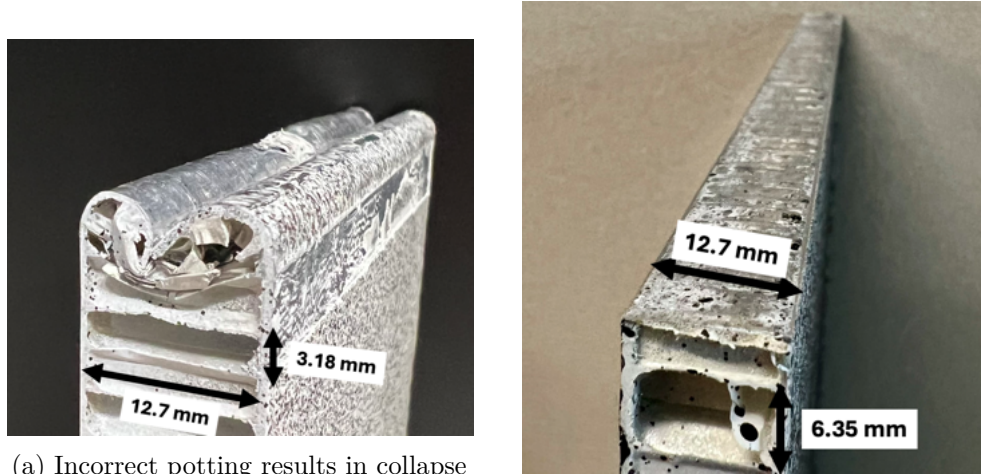
Figure 4.2: Final cut saw setup was based on a wet tile saw. The main components adjusted and added are identified.

4.3 End Potting

As recommended by ASTM D8287, potting compound was applied to the top and bottom edges of the test panel. This reinforcement of the loaded ends of the test panel helps prevent curling of the end of the facesheet under compression load. Figure 4.3 illustrates end curling on a prototype panel with inadequate end potting compared to a well-potted end.

LePage PL Premium Construction Adhesive was used for end potting [51]. This product provided sufficient strength and adhesion. It is premixed and can be worked into cell cavities. It expands only slightly when dried, helping to fill in voids without causing damage. Once fully cured, excess adhesive can be easily removed and flattened in a manner similar to that of working with wood.

Painter's tape was applied to the test panel facesheet along its top and bottom edges to protect the panel from spillover and simplify cleanup. The end of the construction adhesive cartridge was cut small to create a dispensing hole with a diameter of approximately 5 mm. The adhesive was carefully fed



(a) Incorrect potting results in collapse of open end cells and inward curling of facesheet ends.

(b) Correct potting provides open end cell reinforcement which in turn supports the facesheet ends.

Figure 4.3: End potting effect on edge-wise compression tests.

into the open cells along a single edge. The adhesive was worked into open cavities with a wooden tongue depressor. The excess adhesive was removed while wet. The test panels were stored vertically with the adhesive at the top edge while curing. The adhesive was allowed to cure for a minimum of three days before proceeding (see Figure 4.4).



Figure 4.4: Test panel top edges have been filled with construction adhesive and are curing.

Once cured, excess adhesive was carefully cut away with a utility knife while ensuring that no aluminum material was removed. The final shaping of the cured adhesive to bring it to a level even with the edges of the facesheet was

performed by sanding in two steps. A small orbital sander was used to remove most of the excess adhesive remaining. The final removal and smoothing of excess adhesive was performed by hand with 180 grit sandpaper wrapped on a machinist's 1-2-3 block. The machinist's block provided a flat sanding edge.

The whole end potting process was repeated for the bottom edge of the panels. Removal of the painter's tape removed almost all of the adhesive spillover. Any remaining adhesive spillover was dissolved and removed using a section of a rag soaked with methyl ethyl ketone (MEK) ensuring no damage to the panels.

4.4 Test Panel Inspection and Measurements

End potting was the last fabrication step that involved material removal from the test panels. After end potting, test panels were inspected for facesheet condition, edge straightness, and squareness. Inspection of the facesheet condition was performed as a detailed visual inspection. Only minor surface scratches were observed on the test panels. Inspection of the panel edges for straightness and squareness was performed using a large machinist square and a light source. The light source was placed behind the edges being inspected so that light would pass through any gaps between the panel edges and the square. All panel edges were found to be straight and square.

The final panel inspection was carried out by taking dimensions A through H identified in Figure 4.5. ASTM D8287 Figure 4 requires that dimensions A through F be within 0.25 mm. The results of the measurement of the dimensions are presented in Chapter 5, Table 5.5.

As required by ASTM 8287, the test panels were weighed once all material was removed using a kitchen scale and are reported in Table 5.4 [13].

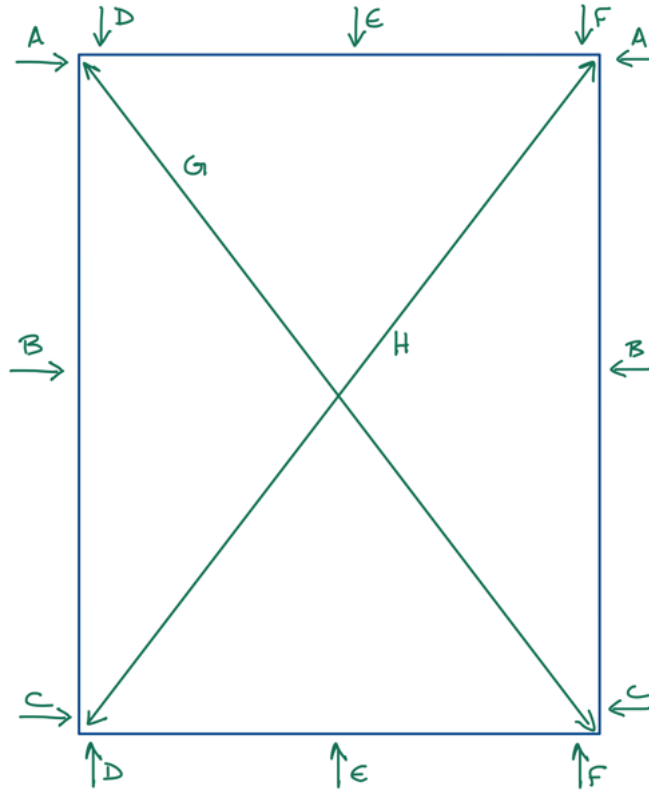


Figure 4.5: Measurements taken for test panel dimension inspection.

4.5 Creating Damage

4.5.1 Drop Tower Design and Fabrication

The test panels were dented with a drop tower. The drop tower was designed and fabricated according to ASTM D7136 standards [49]. Figure 4.6 shows the drop tower in a dynamic state immediately after the drop section is released. The drop tower frame is made of aluminum extrusion. The base plate is made from a 22.23 mm (0.875 inch) aluminum plate, with the working surface that contacts the test specimen milled flat to obtain the required 1 mm (5 thou) tolerance [49]. The rectangular cutout in the base plate immediately below the impactor, as shown in Figure 4.7 was made but is not visible in Figure 4.6. The rubber-tipped clamps that hold the test panel in place were sized to achieve a minimum retention force of 890 N (200 lb_f) and oriented so that the test panels could be moved laterally to effectively create dents at various edge distances while still contacting the panel at the desired locations. The guide pins shown in Figure 4.7 were not included to allow for various placements of

the test panel on the base plate to achieve the various damage edge distances required. The drop section is made of aluminum extrusion, 3D printed plastic parts, and various hardware. The spherical impactor is made of stainless steel. Impactors of 25.4 mm, 38.1 mm and 50.8 mm (1 inch, 1.5 inch and 2 inch) were made and available. Additional steel plates were secured to the drop section to achieve the required weight.

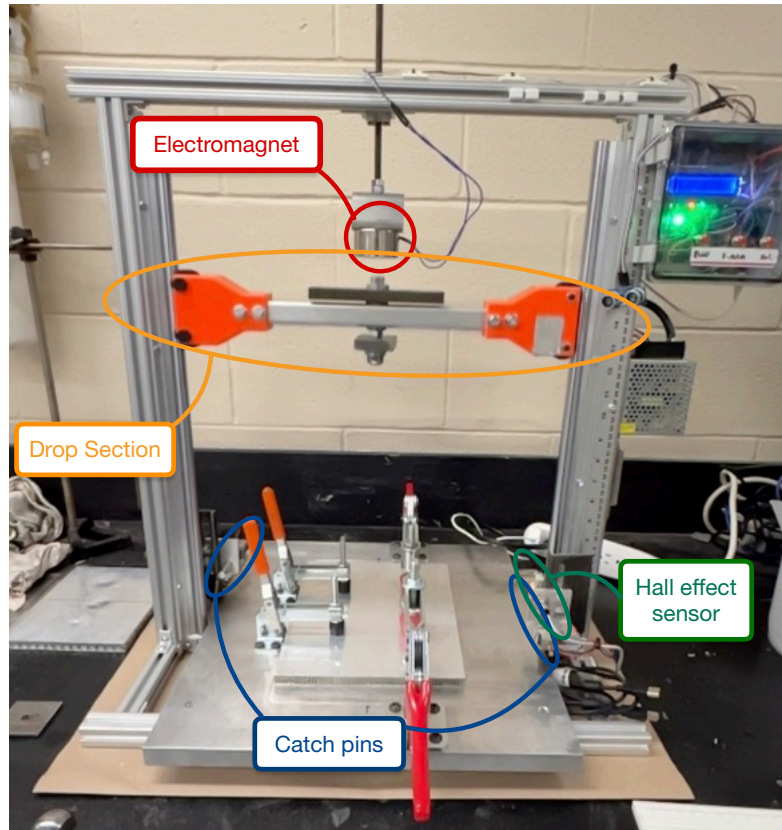


Figure 4.6: Drop tower assembly. In this development test, the drop tower is configured with a 360 mm drop height and a spherical impactor of 25.4 mm (1 inch) diameter.

The drop tower impact actuator sequence is controlled using an Arduino-based controller and various electromechanical devices. The drop section, circled in orange in Figure 4.6, is suspended and released using an electromagnet. The electromagnet, circled in red in Figure 4.6, is attached to a vertical threaded shaft that allows the drop height to be adjusted. The electromagnet is activated by the operator using a button on the Arduino controller, and the drop section is manually raised to the electromagnet. The Arduino deactivates the electromagnet to release the drop section.

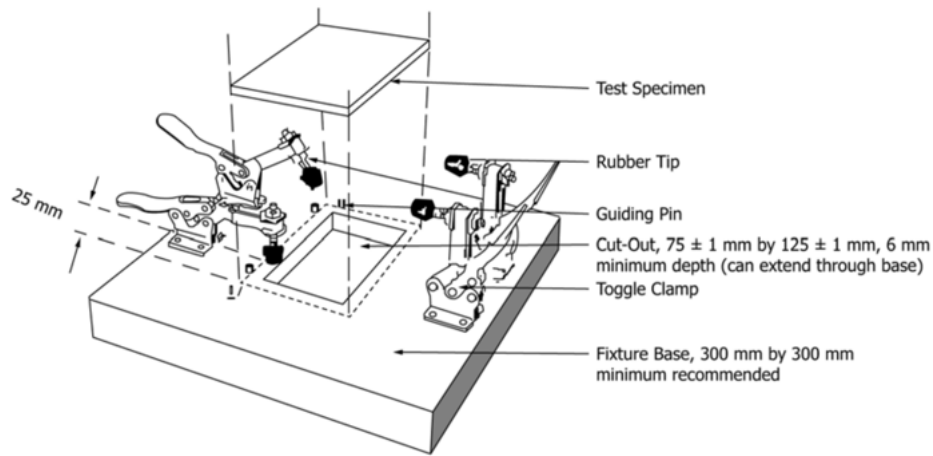


Figure 4.7: Drop tower base plate reference design from ASTM 7136 [49].

Two moving catch pins, circled in blue in Figure 4.6, are placed above the base plate at either end of the drop section span to catch the drop section after a single impact on the test panel. These moving catch pins are actuated by linear electromagnetic actuators. After the drop section is raised to the electromagnet, the catch pins are retracted by the operator using a button on the Arduino controller. The catch pins are released by the Arduino following impact detection.

To trigger the activation of the catch pins, multiple means of detecting the impact were considered, including optical sensors, audio sensors, and Hall effect sensors. An audio sensor was readily available and was first used for this purpose; however, it proved to be problematic. The isolation of impact sound and signal processing caused errors and unacceptable delays in system response. A Hall effect sensor that incorporates threshold detection was placed to effectively perform a switching function. It detects the presence of the drop section immediately before the impactor makes contact with the test panel and triggers the release of the catch pin. The Hall effect sensor is circled in green in Figure 4.6. This design achieved repeatable results and is used in the final design of the drop tower. An optical sensor would have been tested if the Hall-effect sensor had been unsuccessful.

The inclusion of sensors to detect the speed of the drop section was also considered and explored. An ultrasonic sensor was installed on the vertical cross beam of the drop tower and pointed downward to the drop section to measure its speed. The results obtained using this sensor were inconsistent. Furthermore, processing the sensor data and displaying the results took significant processing power from the Arduino. This computational load caused delays that negatively

affected the operation of the essential catch pin mechanism. The ultrasonic sensor is installed, but not used in the final design.

4.5.2 Dent Sizing and Measurement

The size of the damage is characterized by the contour of the dent (smooth or sharp), the width, and the depth. This research is only interested in smooth dents as sharp dents have a much larger impact on residual strength are not usually permissible in aircraft ICA. Spherical impactors, prescribed in ASTM D7136, reliably produced smooth dents and were used in all prototyping and experimental tests. The indentation of the panels using the ASTM 7136 base plate standard with the cut-out [49] resulted in a small outward deformation of the bottom facesheet of the sandwich panel in the dent area. The dents created by the spherical impactor had circular or near-circular perimeters. The dent width was always measured perpendicular to the direction of the honeycomb ribbon and the loading direction.

The width of the dent on flat sandwich panels is traditionally measured by placing a straight edge on the largest dent span and using a flashlight on the back side of the straight edge to determine the dent edges. This procedure was used for this experiment. Upon identification of the dent edges, they were marked and the dent width was measured with a caliper.

The depth of the dent was measured using a precision dial indicator (indicator, Figure 4.8) equipped with a spherical tip and a flat working surface. Due to the deformed bottom facesheet in the dent area, measuring the top facesheet relative to the bottom facesheet in the dent area did not provide an accurate measurement of the depth of the dent. Therefore, an undamaged section of the panel was placed on the flat surface to create and maintain a baseline plane for the panel during measurements with the rest of the panel hanging out beyond the flat surface. The fixed dial indicator was used for the first time to establish a reference position for the upper facesheet of the test panel in an undamaged section. Once a reference position measurement was established, the test panel was moved across the flat surface so that the indicator tip was located at the bottom of the dent (depth position). The difference between the indicator measurement at the reference position and the depth position provided a depth of the dent. Figure 4.9 provides a sketch of the depth measurement setup.



Figure 4.8: Dial indicator (distance amplifying instrument) with spherical tip on flat surface used to measure dent depth.

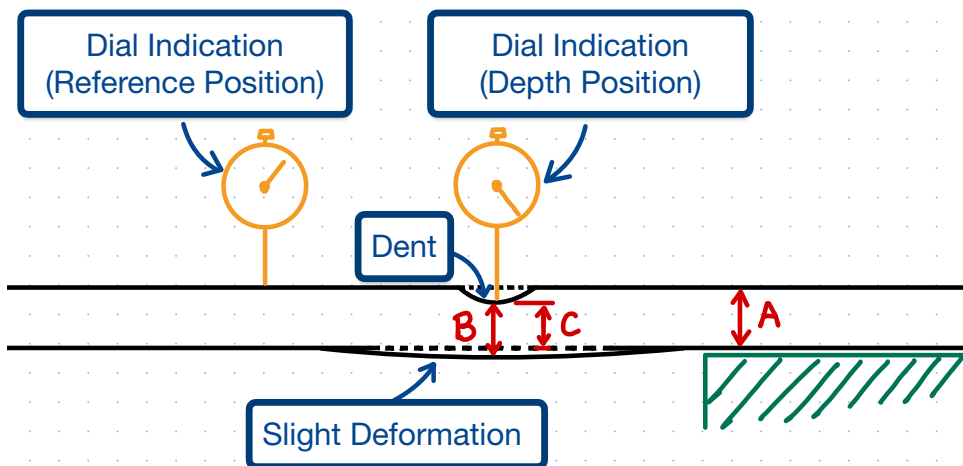


Figure 4.9: Dent measurement sketch showing the sandwich panel with a dented top facesheet and slightly deformed bottom facesheet placed onto a flat surface at a non-deformed section to provide a consistent panel placement. The panel is of thickness A . If the panel were to be placed entirely onto the flat surface, the top facesheet at the dent would be raised by distance B as opposed to the desired distance C . The dent depth is the difference between lengths A and C .

4.5.3 Drop Tower Operation and Damage Results

The target damage depth was established as 20% of the thickness of the panel. For the 12.7 mm panels used, this resulted in a target dent depth of 2.54 mm. The target dent width was $1/5^{th}$ of the test panel width as recommended in ASTM D8287 [13]. Since the test panels had a width of 215 mm, a target dent width of 43 mm was established. ASTM D8287 requires the damage width to be no more than $1/3^{rd}$ of the panel width or 71.6 mm for the 215 mm-wide test panels.

The drop height, the weight of the drop section, and the selection of the impactor are the drop tower configuration variables available to change the dent size. To determine the configuration required to achieve the desired dent shape and size, the available 3.175 mm (0.125 inch) cell aluminum sandwich panel was first used to create the first prototyping coupons. Once the configuration was found that created the desired damage parameters on the first, 3.175 mm (0.125 inch) cell, prototyping coupons, a second set of prototyping coupons were cut from the 6.25 mm (0.25 inch) cell test panel. Only small adjustments were required to the configuration between the first and second set of prototyping coupons to achieve the desired dent size on the 6.25 mm (0.25 inch) cell sandwich panels. The final configuration used to create the desired damage was a 50.8 mm (2 inch) impactor, a drop section weight of 2417 g and a drop height of 365 mm as a measure between the bottom of the impactor and the top facesheet of the undamaged panels.

For the 12 test panels dented with a target depth of 2.54 mm, an average measured depth of 2.58 mm with a standard deviation of 0.13 mm was achieved. For the target dent width of 43.00 mm, and the average measured width of 43.58 mm with a standard deviation of 1.24 mm was achieved. All dent measurements, included all edge distance (ED) configurations, are presented in Table 4.1.

Table 4.1: Manual Dent Measurements.

<u>Test Panel Serial</u>	<u>Dent Location</u>	<u>Depth (mm)</u>	<u>Width (mm)</u>
2023-001	Centre	2.54	44
2023-002	Centre	2.54	46
2023-003	40 mm ED	2.46	42
2023-004	40 mm ED	2.64	43
2023-005	Centre	2.54	45
2023-006	40 mm ED	2.57	43
2023-007	60 mm ED	2.54	44
2023-008	60 mm ED	2.64	43
2023-009	60 mm ED	2.41	43
2023-010	50 mm ED	2.54	43
2023-011	50 mm ED	2.64	45
2023-012	50 mm ED	2.92	42
2023-013	No Dent	-	-

4.6 Speckle Pattern Application

The 3D DIC system requires that a speckle pattern be present on the surface of the object being measured. The speckle pattern is made irregular, such that the DIC system can identify and track the movement and deformation of thousands of unique local patterns throughout the experiment. The speckle pattern should be made of two high contrast colours with each colour covering approximately 50% of the surface area to make detection and identification more reliable. Black and white are commonly used [28].

4.6.1 Speckle Sizing

The size of the speckles in the speckle pattern is determined by the camera resolution and field of view: speckles should be sized to 3 to 5 pixels in the DIC images [52]. This size balances achieving a unique mixture of black and white pixels in each DIC subset and minimising the required size of the DIC subset. In the User Guide of the Correlated Solutions Speckle Kit a table is provided that confirmed that a speckle size of approximately 0.66 mm (0.026 inch) was required [53].

4.6.2 Speckling Methods

Once an entirely black or white base layer is created on the face being speckled, several methods are available to apply a speckle pattern including:

- Using a marker to draw the speckles on by hand;
- Using a speckle pattern stamp to apply the speckle pattern; and
- Using spray paint to apply paint droplets.

Because the dented panel was not flat, the stamp could not be used to apply speckle to the dented area. The marker method took an exceptionally long time to apply. The spray paint method was used because it allowed a random speckle pattern to be applied quickly and consistently.

4.6.3 Speckling Procedure

The speckle pattern was applied following the indentation of the panel. The facesheet was cleaned once again with MEK prior to painting. Two coats of Rust Oleum Painter's Touch 2X Flat White were applied to the dented facesheet to make a base for the speckle pattern to be applied. Rust Oleum Painter's Touch 2X Flat Black was used to create a black speckle pattern on the flat white base.

The white painted panels were placed face-up on the table. The black spray paint can nozzle was held at the same height as the panels, approximately 150 mm away and on one side. The nozzle was partially depressed, allowing the paint to sputter out in larger than normal paint droplets. The amount of nozzle depression was adjusted to change the droplet size. Once the droplets of the right size were created, the can was moved horizontally, allowing the sprayed paint to fall onto and over the panel. This was repeated from multiple sides of the panel until the panel facesheet was approximately 50% black speckle and 50% white background paint. An example of the resultant product is presented in Figure 4.10.

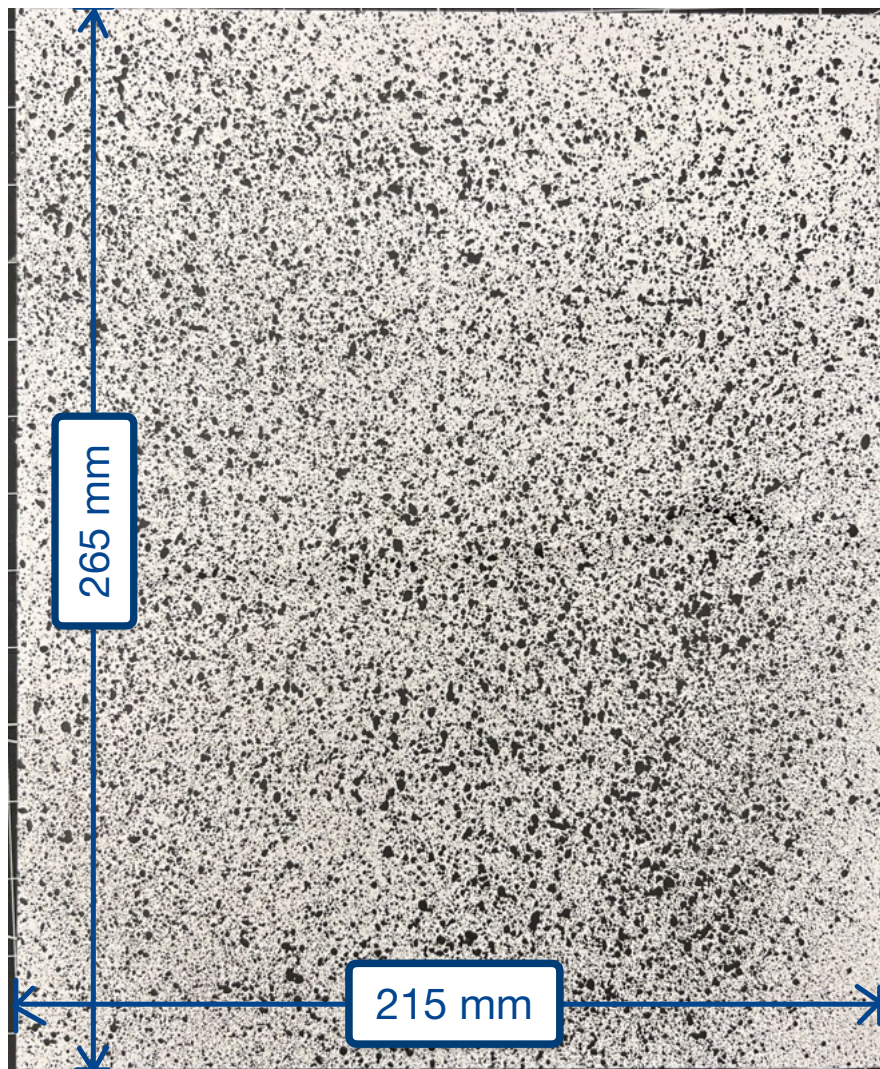


Figure 4.10: Speckle pattern applied to test panel.

4.7 Compression After Impact Testing

Each damaged test panel configuration (centre, 60 mm ED, 50 mm ED, and 40 mm ED) was tested three times. For the non-centre configurations, two test panels had their dent placed on the right side and one had its dent on the left side. This was done to mitigate the effects of any asymmetry associated with the alignment of the CAI support fixture.

4.7.1 MTS and Support Fixture

A MTS Model 204.71 servohydraulic test system installed at the Royal Military College of Canada was used to perform all CAI tests. It was fitted with an ASTM D8287-compliant support fixture made available by the Carleton University Department of Mechanical and Aerospace Engineering. The support fixture, installed in the MTS system, is shown in Figure 4.11.

4.7.2 3D DIC Setup and Calibration

The 3D DIC system used is a Correlated Solution VIC-3D quasi-static solution. The key hardware and software used are provided in Table 4.2. Additional equipment included tripods, lights, various cables, and a desktop computer.

Table 4.2: DIC Equipment and Software List

<u>Item</u>	<u>Description</u>
Cameras [2]	Basler acA2440-77um (5 MP)
Lenses [2]	Schneider-Kreuznach Citrine 1.9/35 C
Data Collection Software	Correlated Solutions VIC-Snap
Post-Processing Software	Correlated Solutions VIC-3D 9

The two cameras used in the 3D DIC system were separated vertically as this maximised shared field of view along the vertical panels edges. The cameras were separated at approximately 25° . The lights were placed outside and forward of the cameras to maximise illumination while avoiding reflections. A pedestal fan was used to keep air moving across the lights and minimise heat waves rising from the lower light interfering with the cameras. The effect of heat waves from the lower light was apparent in the correlated data of early prototype tests. The cameras were connected to the 3D DIC computer by USB 3.0 cables.

Particular care was taken not to disturb the 3D DIC hardware during experimental test sessions. The laboratory was only occupied by the experiment operators and the door was kept closed as much as possible.

The experimental setup is presented in Figure 4.12 (see Figure 4.11 for more detail on the MTS system). The test panel is secured in the support fixture in the MTS servohydraulic system near the centre of the image. The

4.7. Compression After Impact Testing

MTS computer is visible on the left side of the image. The MTS servohydraulic system applies a constant (compressive) displacement at 0.75 mm min^{-1} through the support fixture. This fixed displacement speed was programmed into the MTS system and was established during prototype testing to produce panel failure in 1 min to 10 min, as prescribed by ASTM D8287 [13]. 3D DIC cameras and lights are vertically stacked and visible near the centre of the image with the DIC computer on the right. The strain gauge workstation is located behind the MTS servohydraulic system.

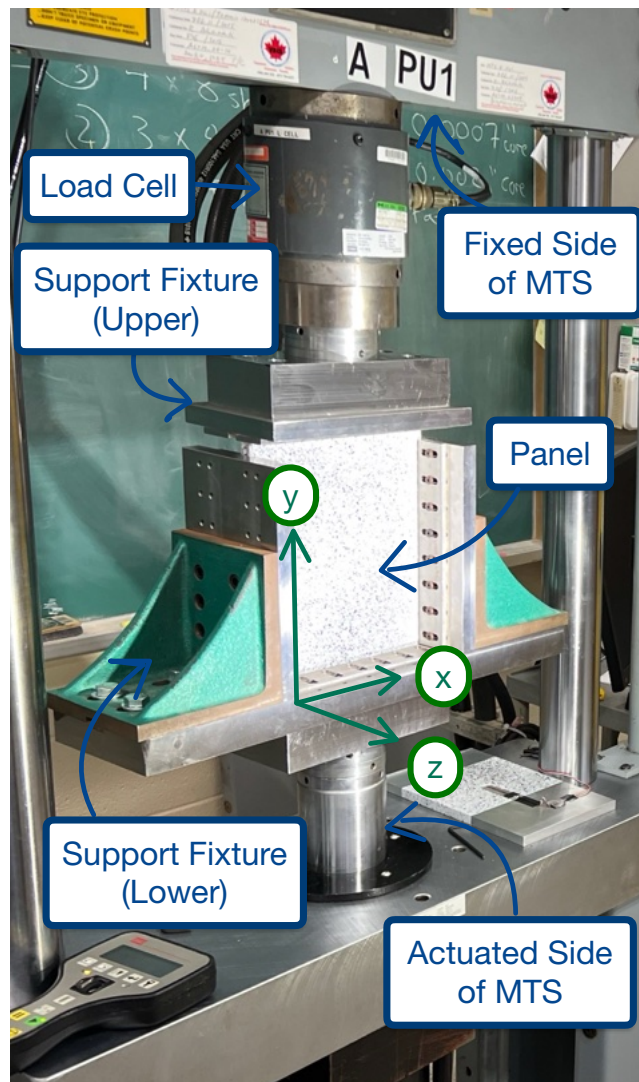


Figure 4.11: ASTM 8287-compliant support fixture installed in MTS servohydraulic test system. Coordinate system is also identified.

At the start of each experimental test session, the 3D DIC system was calibrated according to the manufacturer's instructions. This involves capturing a series of images of a calibration plate in the physical volume that the test specimens will occupy during the experiment. The calibration plate has a known pattern and identifier known to the software. From these calibration plate images, the 3D DIC image collection software can self-determine the exact position of each camera relative to one another. This precise camera position information is the core result of the calibration process. This is what then allows the 3D DIC system to triangulate the position of the test specimen's speckled surface during experimental tests. The typical out-of-plane resolution of the 3D DIC system used is $1/50\,000$ the field of view [54]. The calibration results are presented in Section 5.1.1.

Following the calibration process in either of the Correlated Solutions software programs, a calibration score is provided. The calibration score is the average distance (in pixels) between where the software predicts that a point seen on camera 1 should exist on camera 2 and the actual location that point was found on camera 2 [55]. Scores below 0.1 are considered acceptable, while scores between 0.02 and 0.05 are considered ideal.

4.7.3 Data Collection

Data were collected from the three main systems used during the experimental test sessions. This included a strain gauge, MTS servohydraulic, and 3D DIC system. An analogue DAQ was used to synchronise and transmit the data of the strain gauge and the MTS system to the 3D DIC system.

Strain Gauge System

The data from the strain gauge were only collected during strain validation at the beginning of the experimental test session. The data collected include the strain of the strain gauge on the strain validation panel and a voltage trigger signal used to sync the strain gauge system with the 3D DIC system. The strain gauge was connected to an independent analogue / digital DAQ that communicated with the computer running the catman software [56]. The strain gauge signal was converted to strain in the catman software at a 2 Hz frequency. At the same time, the catman software recorded the voltage of the trigger signal. The synchronised strain and trigger data were exported as a .csv file at the end of each test for further post-processing. The analogue / digital DAQ and software specifications are provided in Table 4.3. The strain gauge specifications are provided in Figure A.2.

More details on the strain validation panel are presented in Section 4.7.4.

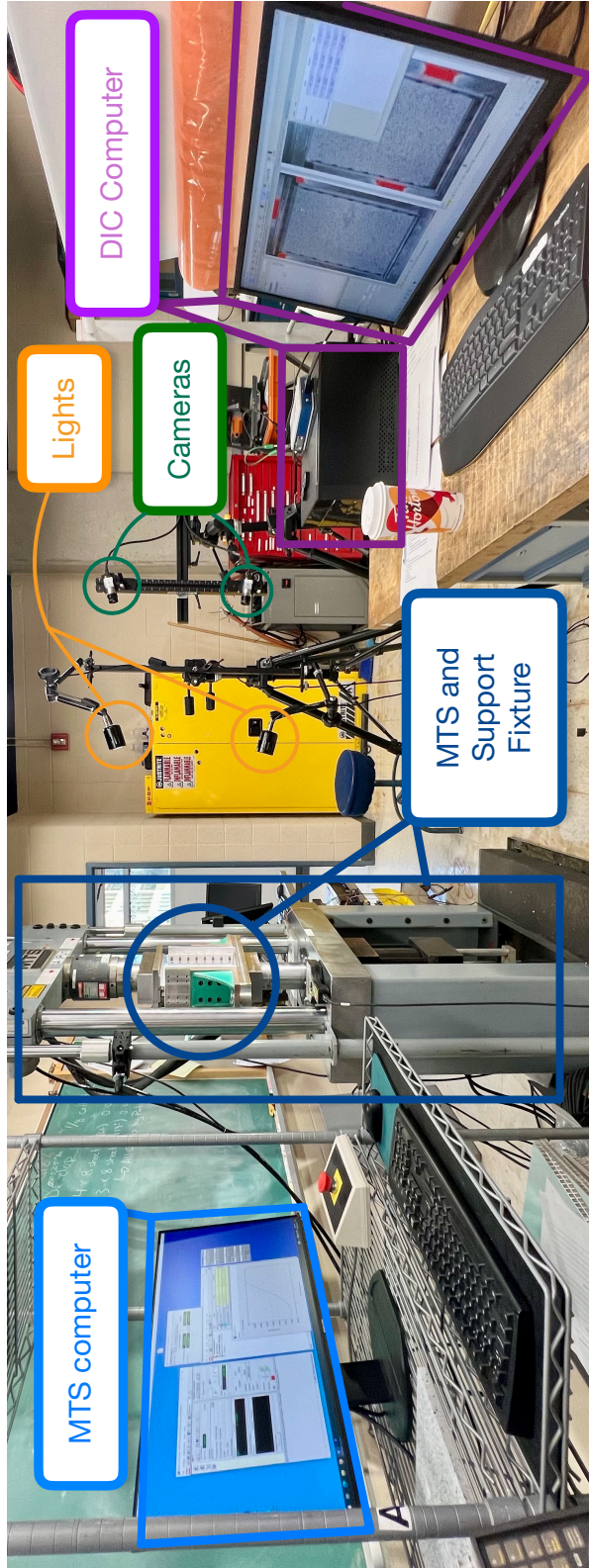


Figure 4.12: Experimental setup. Key components are identified.

Table 4.3: Strain gauge system specifications.

<u>Item</u>	<u>Description</u>
Analogue / Digital DAQ	HBM QuantumX 1615b
Software	HBM CatmanEasy V5.2.2.19

MTS Servohydraulic System

The MTS servohydraulic system generated force, displacement, and time data that were used in post-processing. The data were recorded in two places. First, the data were recorded at a 10 Hz frequency in a generic data file. Second, the force and displacement data were communicated to the 3D DIC system via a DAQ at a 2 Hz frequency. The software used to control the system and generate data is the MTS Flex Test 40 Station Manager. MTS servohydraulic system specifications are provided in Table 4.4. The calibration certificate for the system is provided in Figure A.3.

Table 4.4: MTS servohydraulic system specifications.

<u>Item</u>	<u>Description</u>
Servohydraulic and Load Cell	MTS Model 204.71 (250 kN)
Digital Controller	MTS Flex Test 40
Software	MTS Flex Test 40 Station Manager V5.9E

3D DIC System

The two cameras of the 3D DIC system captured image pairs of test panels and validation panels at a 2 Hz frequency using VIC-Snap software. Furthermore, VIC-Snap software collected digital information from other systems through the DAQ at the same 2 Hz frequency. Force and displacement information was collected from the MTS servohydraulic system during all tests. The same trigger signal that was sent to the strain gauge system during strain validation was sent to the 3D DIC system. These data were recorded in a combination of image files and .csv files for post-processing.

4.7.4 Strain Validation

Before starting the test session, the strain measurements from the calibrated DIC system were compared with those measured by strain gauges using a purpose-fabricated strain validation panel subjected to edge-wise compression. 3D DIC results were validated by obtaining agreement between the two systems. In the absence of the two far-field strain gauges prescribed in ASTM D8287, the 3D DIC strain in the far-field region was examined.

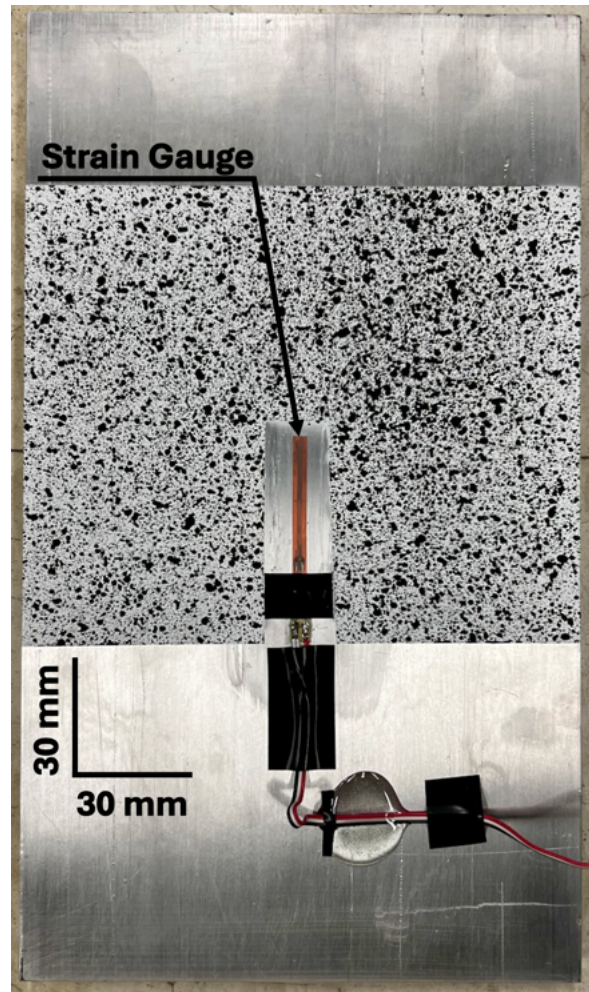


Figure 4.13: A strain validation panel was created from a wide aluminum bar. The bar was instrumented with a 30 mm strain gauge and a speckle pattern was applied to the top face. This apparatus permits comparison of DIC-calculated strain with strain gauge measurements.

The strain validation panel was made of a wide aluminum bar 12.7 mm (0.5 inch) thick and 152 mm (6 inch) wide with the upper and lower faces cut and milled parallel at approximately 265 mm separation. A 30 mm strain gauge was installed in the centre of the exposed face. The central location was selected as it would be the least affected by potential loading asymmetry. The strain gauge was designed for use on steel surfaces as this was the most applicable and available product for the aluminum surface. The certification data for the strain gauge are presented in Figure A.2 in the Appendix A. A speckle pattern was applied to most of the exposed face, as shown in Figure

4.13. In post-processing in the VIC-3D 9 software, 30 mm extensometers were digitally drawn on either side of the physical strain gauge. Figure 4.14 shows the strain validation panel being processed in VIC-3D 9 including the digital extensometers.

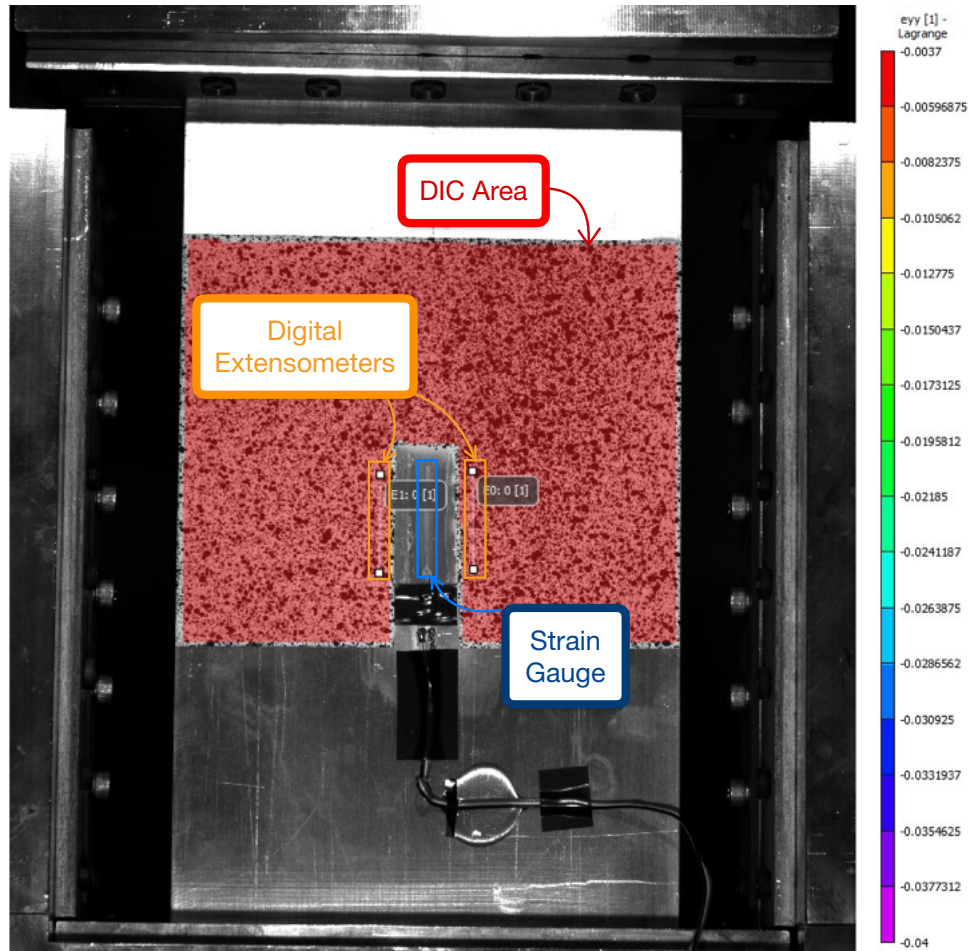


Figure 4.14: Strain validation panel being processed in VIC-3D 9. The 30 mm strain gauge, the two digitally-applied 30 mm extensometers (E0 and E1), and the DIC area are identified. The scale shown is vertical strain, e_{yy} , from 0.37% (red) to 4% (purple).

The MTS system was set to a constant displacement rate of 0.75 mm min^{-1} for strain validation. This test was stopped manually when a load of approximately 150 kN was reached. This load provided a sufficiently large data set of more than 100 points, kept the aluminum under elastic deformation, and was relatively short to perform at 1 min to 2 min. Once the 3D DIC strain values

were validated, CAI of the test panels could be performed. The test procedure described in ASTM D8287 was followed, except for matters related to strain gauges in the far-field strain [13]. The calibration results are presented in Section 5.1.2.

4.7.5 Test Procedure

The MTS test procedure was set to have a fixed displacement rate of 0.75 mm min^{-1} for the test panels as well. This displacement resulted in the failure of the dented test panel between 5 min and 6 min, which is within the ASTM D8287 standard of 1 min and 10 min [13]. The non-damaged panel took longer to fail at approximately 7 min. Force and displacement information was sent to the 3D DIC system through the DAQ for the entire test.

The test panel was placed in the support fixture and the support fixture was moved into position. The 3D DIC image capture procedure was started before the MTS test procedure was initiated and stopped after the MTS test procedure was stopped. The test was stopped only after the resistive force of the test panel reached its peak and had dropped by at least 30 %.

4.8 Post-Processing

4.8.1 Strain Validation

Strain validation was performed at the beginning of each test session. Following the strain validation test, the .csv file from the strain gauge system was transferred to the 3D DIC system for analysis.

With the 3D DIC system calibration previously completed, the strain validation panel images generated in VIC-Snap were processed for image correlation in VIC-3D 9. The area of correlation was selected to be the entire area of the speckle pattern with a cutout around the strain gauge. System recommendations were used for the size of the subset and step size (see Section 5.1.1 for values). Once the correlation was complete, the vertical Lagrangian strain (e_{yy}) was selected as the contour variable. 30 mm digital extensometers were placed vertically on either side of the strain gauge on the speckle pattern to measure the relative change in length of those spans. An extraction computation was performed for the image set. This generated both the average e_{yy} for the speckle pattern and the relative change in length data for each of the created digital extensometers. These data, along with the force, displacement, and trigger data from the DAQ, were exported from VIC-3D 9 to a .csv file.

The 3D DIC and strain gauge .csv files were combined into an Excel spreadsheet. The trigger data, present in both datasets, were used to align the indices in the two datasets. A graph was plotted to compare the three strain data

sources: strain gauge, average DIC e_{yy} strain, and average digital extensometer strain. Section 5.1.2 provides a detailed example of that comparison.

4.8.2 MTS Data

Force, displacement and time data recorded on the MTS system were transferred to an Excel spreadsheet for processing. The data were organised by test panel configuration and each test data series were aligned at 5 kN loads. The alignment at 5 kN helped account for differences in the structural settling of the sandwich panels under initial loading. These data were used to generate the force and displacement data presented and discussed in Sections 6.2 and 6.3.

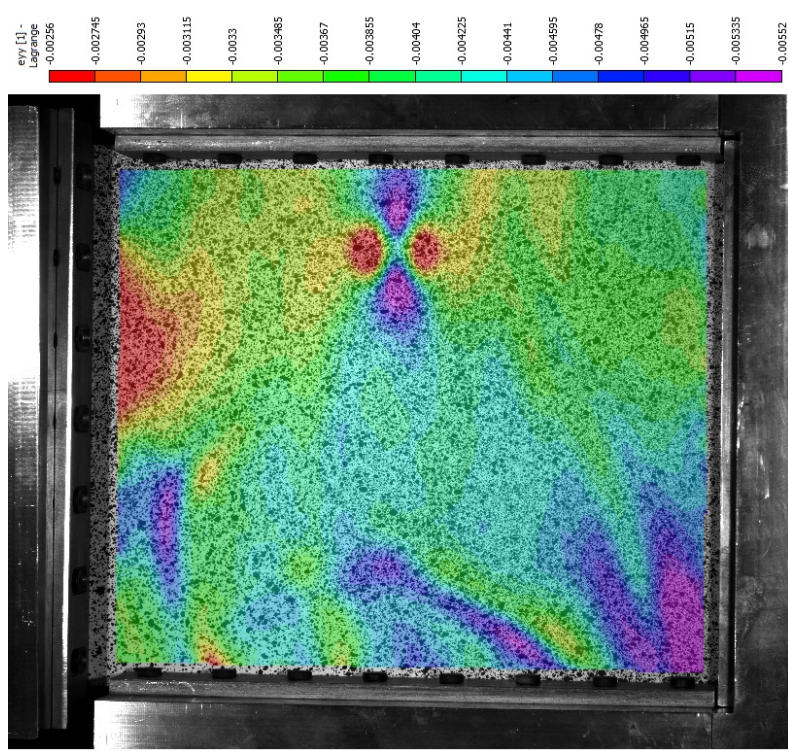
While force and displacement data were also available in the 3D DIC system from the DAQ connection, the MTS system data was used where possible for the following reasons:

- It was of higher resolution (10 Hz vice 2 Hz);
- The data transferred via the analogue DAQ, by nature of being analogue signals, had some noise that was not present in the MTS data; and
- The 3D DIC system data for panels 2023-003 and 2023-013 was incomplete. The MTS data that had been communicated through the DAQ to the DIC system was also incomplete. Complete data sets for all panels were available in the original data files on the MTS system computer.

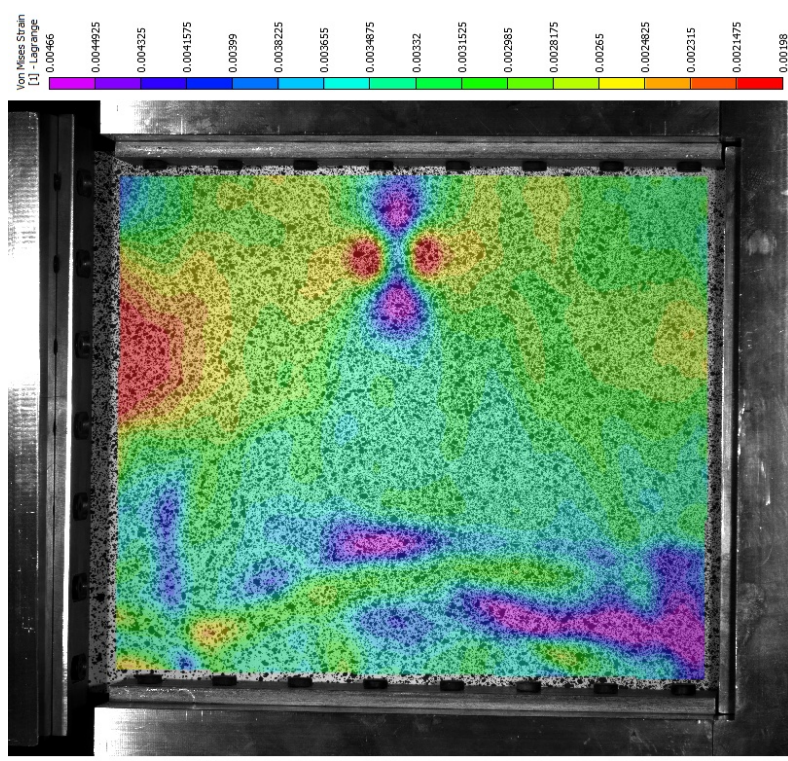
4.8.3 3D DIC

VIC-3D 9 was used for post-processing of the images and data collected through the DAQ. The VIC-3D 9 contour images were generated using both Lagrangian vertical strain (e_{yy}) and the out-of-plane facesheet coordinates (z). Figure 4.11 shows the coordinate system used. The inspection line tool was used to measure the depth profile of the dent. Extraction and export tools were used to generate .csv files containing strain, deformation, force, and displacement data.

Lagrangian vertical strain (e_{yy}) was used to quantify strain as vertical strain was the dominant expected strain in the CAI test and closely related to the strain measured by vertical strain gauges normally used to measure far-field strain on ASTM 8287 test panels [13]. Von Mises strain could have been used; however, the Lagrangian vertical strain component would be expected to be the largest contributing factor. Figure 4.15 compares von Mises and Lagrangian vertical strain (e_{yy}) facesheet strain for a test panel at net section yield. Noting that von Mises strain calculations always provide positive values, even when strains are compressive, it can be seen in Figure 4.15 that both strain calculation approaches identify similar high- and low-strain areas in the facesheet. In this correlation image, Lagrangian vertical strain values range from -0.26% to -0.55% strain as opposed to the von Mises strain, which ranges from 0.20% to 0.47% strain for the same correlation image.



(a) Von Mises facesheet strain distribution for test panel 2023-004 at net section yield.



(b) Lagrangian vertical facesheet strain (e_{yy}) distribution for test panel 2023-004 at net section yield.

Figure 4.15: Comparison of facesheet strains calculated using VIC-3D 9 for the same correlation image. Note that von Mises strain calculation always return a positive value, even in compression.

Several contour variable extraction images were generated in VIC-3D 9 and exported as image files for further processing. Although multicolour contour extraction images helped to understand changes in facesheet strain distribution throughout the test, these results made quantitative analysis difficult. The contour plots for the e_{yy} extraction images were made binary about a predicted yield strain for quantitative strain analysis purposes. Similarly, the contour plots for the z extraction images were made binary with an indentation threshold of 0.25 mm for quantitative deformation analysis purposes.

ImageJ for further analysis of 3D DIC Data

The open source image processing and analysis software ImageJ was used in the quantitative analysis of deformation and strain images. Specifically, once the images were scaled, dent area and width was measured on deformation images and elastic strain area was measured on strain images. Binary strain and deformation images generated in VIC-3D 9 were imported into ImageJ. The images processed in ImageJ underwent the following procedure:

- Set scale. The image scale was set using the known distance between the knife edge bolts (see Figure 4.16 for a sample of an unprocessed deformation image).
- Crop. The image was cropped to the largest available analysed rectangular area.
- Type. The image was converted to 8-bit.
- Scale bar. 50 mm vertical and horizontal scale bars were added.
- Adjust threshold. The threshold was adjusted to differentiate about the binary threshold represented in the image.
- Particle analysis. Particle analysis was performed, including area calculations. These area data represented the dent area and were saved to an Excel spreadsheet.
- Dent width. For deformation (z) images only, the dent width was measured using an inspection line. These data were also saved to an Excel spreadsheet.
- The cropped images were saved as new files.

The results are presented in Sections 5.3, 5.4, 6.3, and 6.4.

4.8.4 Net Section Yield

In addition to characterizing edge effects by examining the unloaded and peak load conditions in detail during the CAI tests, the edge effect's yield conditions were characterized. Local yielding of the facesheet is a focus of the DIC analysis presented in the following chapters; however, the onset of net section yield of the test panel is also of interest.

For honeycomb sandwich panels in edge-wise compression, the core is not expected to carry loads directly. The role of the honeycomb core during CAI is, namely, to keep the two facesheets parallel to each other. The honeycomb

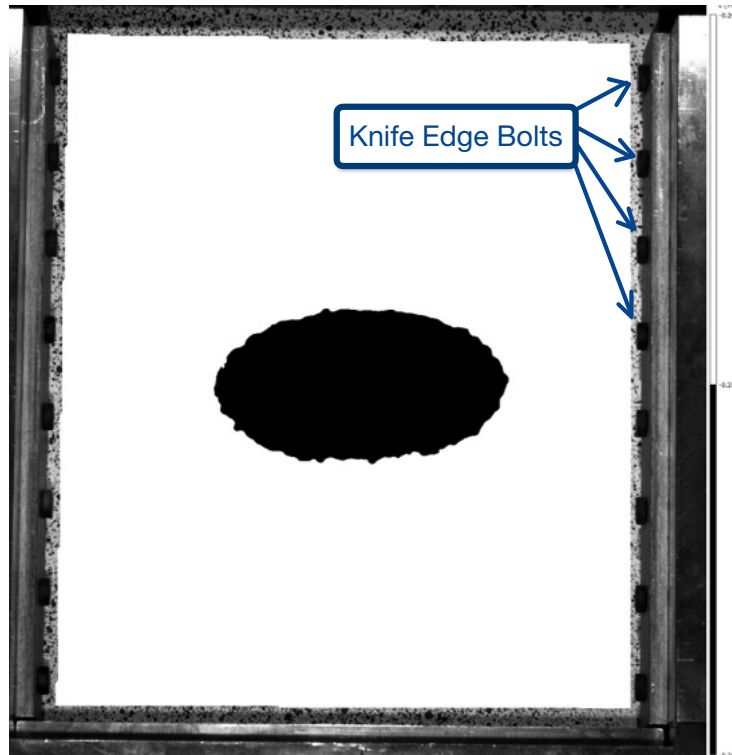


Figure 4.16: Sample deformation image before being processed. Knife edge bolt spacing was used as reference to set the image scale.

core only carries secondary loads during edge-wise compression of the sandwich panel. The adhesive strength is small relative to the aluminum facesheets and is not expected to carry primary loads during edge-wise compression of the sandwich panel: rather, it transfers the secondary loads between the facesheet and core.

Primary edge-wise compression loads experienced during CAI are carried by the facesheets in the loading direction. This means that the compressive material properties of the facesheets are likely to be most relevant to the sandwich panel properties in CAI. Similarly, the most relevant cross section to consider in edge-wise compression tests of a sandwich is the cross-sectional area of the facesheets relative to the loading direction. As presented in Section 4.2, the sandwich panels used for these tests are both 0.508 mm(0.020 inch) thick 2024-T3-Clad aluminum. For the 215 mm wide test panels, the cross-sectional area (A) is calculated using combined facesheet thickness (t) and width (W) using Equation 4.1.

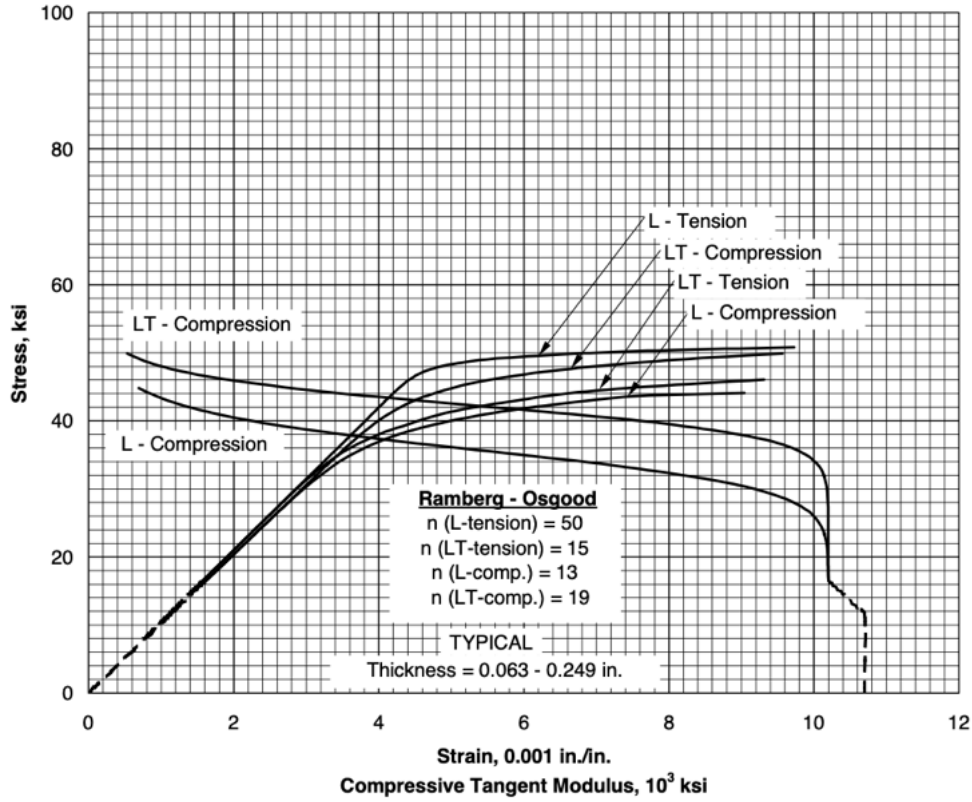


Figure 4.17: Typical tensile and compressive stress-strain and compressive tangent-modulus curves for 2024-T3-clad aluminum alloy sheet at room temperature [57].

$$\begin{aligned}
 A &= t \times W, \\
 &= [2 \times 0.508 \text{ mm}] \times [215 \text{ mm}] \\
 &= 218 \text{ mm}^2
 \end{aligned}
 \tag{4.1}$$

The exact compressive yield stress, $\sigma_{y,c}$, of 0.508 mm (0.020 inch) thick 2024-T3-clad aluminum is difficult to test and an exact value was not found to be published in MatWeb, MMPDS or the literature [57, 58]. The MMPDS provides typical tensile and compressive stress-strain curves for 2024-T3-clad aluminum at room temperature showing that the compressive curves are similar to the tensile curves, but have slightly less stress at a given strain (reproduced in Figure 4.17). MatWeb publishes a number of tensile yield stresses, $\sigma_{y,t}$ of 2024-T3-clad aluminum sheet at various thicknesses. For a sheet thickness of 0.254 mm to 1.57 mm (0.0100 inch to 0.0620 inch) a $\sigma_{y,t}$ of 270 MPa is published.

Although tensile and compressive yields are recognised to behave differently, the tensile yield stress of the facesheet material will be used to predict the net section yield of the sandwich test panels. Using a yield stress of 270 MPa, a net section yield force of 59 kN is calculated as presented in Equation 4.2 [58].

$$\begin{aligned} F &= \sigma_y \times A, \\ &= [270 \text{ MPa}] \times [218 \text{ mm}^2] \\ &= 59 \text{ kN} \end{aligned} \tag{4.2}$$

4.8.5 Data Presentation and Sign Conventions

In tension and compression testing, tensile forces and sample lengthening displacements are traditionally considered positive values. As CAI tests are compression tests, the displacement applied and the resulting forces are considered negative values. They are plotted as such in this paper.

5 Results

5.1 Verification and Quality Control

The destructive CAI tests were performed in three sessions of experimental test sessions on October 10th, November 8th and November 28th 2023. The 3D DIC system was calibrated and the strain was validated using the strain validation panel at the start of each of these experimental test sessions. The MTS servohydraulic test apparatus used, including the displacement and load cell instruments, was calibrated by an MTS Systems Corporation and valid during this period. Figure A.3 in Appendix A provides a copy of that MTS Systems Corporation calibration certificate.

5.1.1 3D DIC System Calibration and Resultant Accuracy

Experimental tests were performed in three test sessions. Calibration scores for the 3D DIC system from these three calibration events are 0.059 pixels, 0.058 pixels and 0.064 pixels. These scores are well below the acceptable threshold of 0.100 pixels and approaching the ideal case values of 0.02 pixels to 0.05 pixels [54]. These scores were achieved using 27, 24, and 25 calibration images, respectively. A total of up to 30 calibration images were captured for each session, and exceptionally poor images were deleted from the series to improve calibration scores.

As mentioned in Section 4.7.2, the typical out-of-plane resolution of the 3D DIC system used is 1/50 000 the field of view [54]. Based on the equipment used, the viewing area of approximately 0.3 m × 0.3 m, and an ideal calibration score, an ideal out-of-plane resolution (Z) of approximately 6 μm is calculated. See Equation 5.1 for the calculation of the ideal resolution in the out-of-plane, z , direction. However, the achieved calibration scores are not quite in the ideal range. It was decided to apply a safety factor (SF) of three to the expected resolution to conservatively account for achieving a calibration score slightly outside the ideal range. As a result, this paper expects an out-of-plane resolution of 18 μm or 0.018 mm. See Equation 5.2 for the calculation of the expected resolution in the out-of-plane, z , direction.

$$\begin{aligned}\text{Ideal Resolution}_z &= \text{Viewing Area Width} \times \frac{1}{50\,000} \\ &= 0.3\text{ m} \times \frac{1}{50\,000} \\ &= 6\ \mu\text{m}\end{aligned}\tag{5.1}$$

$$\begin{aligned}\text{Expected Resolution}_z &= SF \times \text{Ideal Resolution}_z \\ &= 3 \times 6\ \mu\text{m} \\ &= 18\ \mu\text{m}\end{aligned}\tag{5.2}$$

Meanwhile, the typical in-plane resolution of the 3D DIC system used is 1/100 000 the field of view [54]. The in-plane resolution is used for the strain calculation in this experiment and does not depend on the stereo calibration of the cameras. Rather, the in-plane resolution is a function of a simpler 2D DIC system that is not related to the calibration score. The calibration score is a measure of the average error (in pixels) between where the system expects a point observed in camera 1 to appear in camera 2 and where that point is actually located in camera 2's image. Therefore, an in-plane resolution of approximately 3 μm can be expected from this experimental setup. See Equation 5.3 for calculation of the ideal resolution in the in-plane, x and y, directions.

$$\begin{aligned}\text{Ideal Resolution}_{xy} &= \text{Viewing Area Width} \times \frac{1}{100\,000} \\ &= 0.3\text{ m} \times \frac{1}{100\,000} \\ &= 3\ \mu\text{m}\end{aligned}\tag{5.3}$$

Table 5.1 presents the subset and step values used for each of the test panels. For each test panel, the size of the subset was adjusted according to VIC-3D 9's recommended values for each panel, while the step size was kept at 7 pixels.

5.1.2 Strain Validation

The strain validation exercises were carried out successfully using the strain validation panel presented in Figure 4.13. The results of the strain validation exercise on November 28, 2023 are presented in Figure 5.1. As the aluminum bar used for the strain validation panel is made of a homogeneous material, the expected strain at any two points on the top face is expected to be identical. Figure 5.1 shows a linear elastic stress-strain measurement from the strain gauge. The average DIC strain (average strain calculated in the DIC area

Table 5.1: Subset and step size values for each test panel.

<u>Test Panel Serial</u>	<u>Subset (pixels)</u>	<u>Step (pixels)</u>
2023-001	27	
2023-002	27	
2023-003	27	
2023-004	23	
2023-005	23	
2023-006	23	
2023-007	25	7
2023-008	25	
2023-009	31	
2023-010	27	
2023-011	29	
2023-012	27	
2023-013	29	

of interest) follows the same trend; however, it has some scatter and reports slightly less strain than the strain gauge. The two digitally applied DIC extensometers follow the same trend, but have significantly more scatter than the average DIC strain.

A Bland-Altman plot is used to assess the agreement between two quantitative measurements. It consists of plotting the difference between two measurements against their average. It was used to assess the agreement between the average DIC strain and the strain gauge in addition to the agreement between the strain of the DIC extensometers and the strain gauge. The results are presented in Figures 5.2 and 5.3 respectively. In these figures, the average strain is plotted against the difference in measured strain for each point. The solid red line marks the average difference, while the upper and lower bounds (at a 95 % confidence interval) are marked with red dashed lines. Equations 5.4 through 5.7 are used for the Bland-Altman plot values as follows:

- Calculate the average of the two measurements:

$$\text{Average} = \frac{\text{Measurement 1} + \text{Measurement 2}}{2} \quad (5.4)$$

- Calculate the difference between the two measurements:

$$\text{Difference} = \text{Measurement 1} - \text{Measurement 2} \quad (5.5)$$

- Calculate the standard deviation, SD:

$$\text{SD} = \sqrt{\frac{\sum |i - \mu|^2}{N}} \quad (5.6)$$

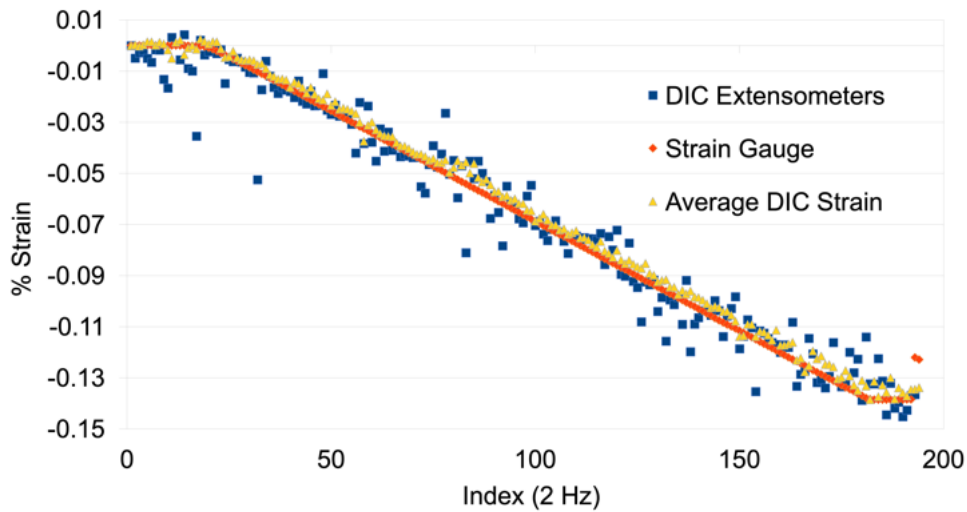


Figure 5.1: Results from the strain validation performed at the start of batch experimental testing on 28 November 2023. Readings from the 30 mm strain gauge, the average DIC strain, and the average of two digital extensometers placed on either side of the strain gauge in DIC post-processing are compared.

- Calculate the 95 % confidence interval, CI95:

$$\text{CI95} = 1.96 \times \text{SD} \quad (5.7)$$

The DIC system and strain gauge values are very similar. There is some scatter, but overall agreement in the DIC results for local (small area) strain values. The average difference is -0.0028% strain with upper and lower bounds (at a 95 % confidence level) of 0.0081% and -0.0025% strain respectively.

The strain values of the DIC extensometers follow the same trend as the strain gauge values; however, there is significant scatter in the extensometer values as compared to the strain gauge values. The average difference between the two is -0.0005% strain with upper and lower bounds (at a confidence level of 95 %) of 0.0171% and -0.0182% strain respectively. The upper and lower bounds are 0.0353% strain apart as opposed to the average facesheet strain bounds, which are only 0.0106% strain apart. There is more than three times the scatter when strain gauge results are compared with extensometer strain results, as with average facesheet strain results. The DIC extensometers were visually aligned with the strain gauge in VIC-3D 9 which may have been imperfect and contributed to the differences in measured strain. However, it is more likely that the scatter in the strain measured by the extensometer is a result of the extensometer values being based on the location of a small

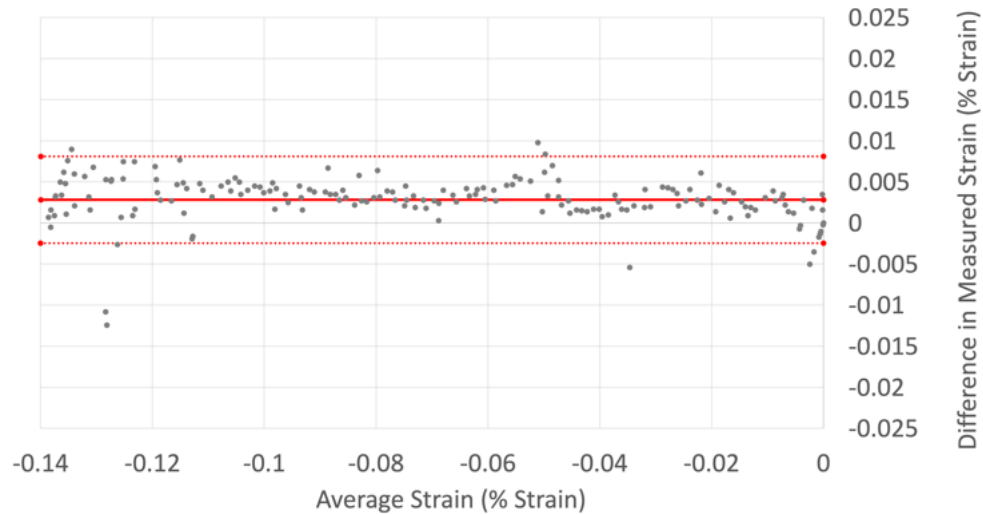


Figure 5.2: Bland-Altman plot comparing the 30 mm strain gauge % strain reading with average validation panel speckle area % strain measured using 3D DIC. Data is from the strain validation test completed at the third of three batch experimental testing events, 28 November 2023.

number of subsets and momentary errors in the correlation computations. These small errors in a single subset correlation would normally be considered in the context of results for nearby subsets, and data smoothing would be performed by VIC-3D 9.

The way in which the strain verification results informed the analysis of the experimental results is discussed in Section 6.1.4.

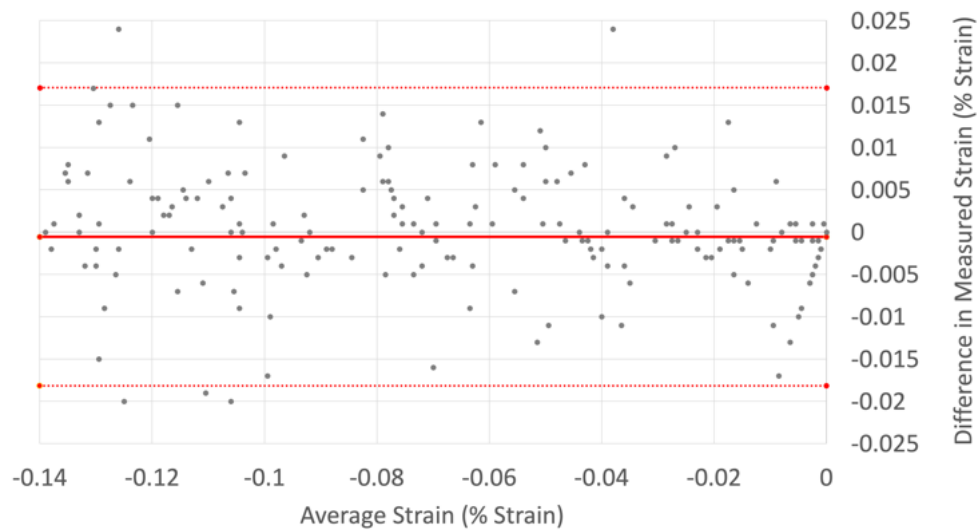


Figure 5.3: Bland-Altman plot comparing the 30 mm strain gauge % strain reading with % strain calculated via two 30 mm digital extensometers placed in the speckle pattern on either side the strain gauge in DIC post-processing. Data is from the strain validation test completed at the third of three batch experimental testing events, 28 November 2023.

5.1.3 Dent Depth and Width Measurements with 3D DIC

The depths of the dent were measured in VIC-3D 9 using an inspection line drawn horizontally through the dent centre. The data extracted from the inspection gave a two-dimensional cross-sectional profile of the dent running along the inspection line. Figure 5.4 is an example of this process with the inspection line on the test panel visible and the extracted out-of-plane deformation data from that line plotted below. This method was more precise than manual measurements. However, this additional resolution made it more difficult to select the dent edge and therefore the out-of-plane reference point from which the dent depth would be measured. The small change in the selection of the dent edge had a significant difference in the calculated depth of the dent. Taking Figure 5.4 for example, the z value marking the left edge of the dent could be reasonably selected on the curve and between -0.1 mm and -0.3 mm, while the right edge of the dent could be reasonably selected on the curve between 0.1 mm and -0.1 mm. This could result in difference of dent depth measurement of up to 0.4 mm. The average of the combined range (left and right edges) of reasonable values was selected.

Undented panels were inspected for comparison and, by visual inspection with a straight edge and backlighting, they did not display this minor convexity in either facesheet. The panel appeared to be perfectly flat. Furthermore, the sandwich panels used had the same facesheet on both faces. The determination of front (dented) vs rear (non-dented) facesheet was arbitrary during fabrication. It is suspected that the minor convexity observed in the 3D DIC deformation was caused during the drop tower indentation process.

Manual depth measurements are compared with 3D DIC dent depth measurements in Table 5.2. The average absolute difference in measured depth between the manual and DIC methods was 3.9%. Although there was up to a 15% difference in the measured depth, the mean absolute difference was small. Furthermore, the mean and standard deviation of the depth of the dent measured by 3D DIC, 2.56 mm and 0.13 mm, as compared to the manual measurement values, 2.54 mm and 0.14 mm are very similar. These very similar mean dent depth measurements and the small mean absolute difference indicate that the two methods were reasonably comparable for characterising dent depth. As the DIC method relied on digitally stored information, the measurement could be taken multiple times after the destructive CAI experiment. Meanwhile, the manual dent method could only be performed before the CAI experiment.

The width of the dents was measured as the diameter of the dent in the direction perpendicular to the loading direction. The width of the dent was measured digitally through a combination of 3D DIC analysis and image processing in ImageJ. The black and white images presented and described in Section 5.3 identify all areas of the facesheet indented by more than 0.25 mm for each test panel. A 0.25 mm threshold was chosen as a smaller threshold

Table 5.2: Dent Depth Measurement Comparison - Manual vs 3D DIC

<u>Panel Number</u>	<u>Dent Depth (mm)</u>		<u>Absolute Difference (%)</u>
	<u>Manual</u>	<u>DIC</u>	
2023-001	2.54	2.53	0.4
2023-002	2.54	2.57	1.2
2023-003	2.46	2.33	5.3
2023-004	2.64	2.62	0.8
2023-005	2.54	2.58	1.6
2023-006	2.57	2.50	2.7
2023-007	2.54	2.60	2.4
2023-008	2.64	2.62	0.8
2023-009	2.41	2.34	2.9
2023-010	2.54	2.76	8.7
2023-011	2.64	2.78	5.3
2023-012	2.92	2.48	15.1
2023-013	-	-	-
Mean	2.58	2.56	3.9
Standard Deviation	0.13	0.14	4.3

was found to capture blemishes on the facesheet that would not be easily identified in a visual inspection of aircraft panels or classified as dents. Once these images were scaled in ImageJ, a dent width was taken for each initial test panel image by manually applying a horizontal inspection line in ImageJ. The manual placement of an inspection line in ImageJ is comparable to the manual dent width measurement technique using a straight edge and caliper. The resultant dent width is compared to the manually measured dent width in Table 5.3 (also manually applied in the horizontal direction). The mean absolute difference in measured width between manual and DIC methods was 15%. The dent width measured by 3D DIC image analysis using the indentation threshold of 0.25 mm was consistently smaller than the manual width measurement: the mean dent width measured by 3D DIC image analysis was 38 mm while the mean for the manual measurement was 44 mm. The consistently smaller dent width in digital measurement was most likely a result of the dent perimeter threshold of 0.25 mm. A lower threshold of 0.20 mm or 0.15 mm would be expected to reduce the difference in the mean measured dent size but would likely result in a classification of some facesheet blemishes as dents. Furthermore, a repeatable process for measuring the width of the dent in VIC-3D 9 alone, using an inspection line and extraction of z and x coordinates along that line, may be worth considering in future research however; this may disassociate dent width measurements (now calculated in VIC-3D 9) from area measurements (calculated in ImageJ using dent thresholds).

Table 5.3: Dent Width Measurement Comparison - Manual vs 3D DIC and ImageJ

<u>Test Panel Number</u>	<u>Dent Width (mm)</u>		<u>Absolute Difference (Percent)</u>
	<u>Manual</u>	<u>Digital</u>	
2023-001	44	43	2
2023-002	46	52	14
2023-003	42	31	26
2023-004	43	36	17
2023-005	45	41	10
2023-006	43	33	23
2023-007	44	37	17
2023-008	43	37	15
2023-009	43	34	22
2023-010	43	38	11
2023-011	45	43	5
2023-012	42	33	22
2023-013	-	-	-
Mean	44	38	15
Standard Deviation	1	6	7

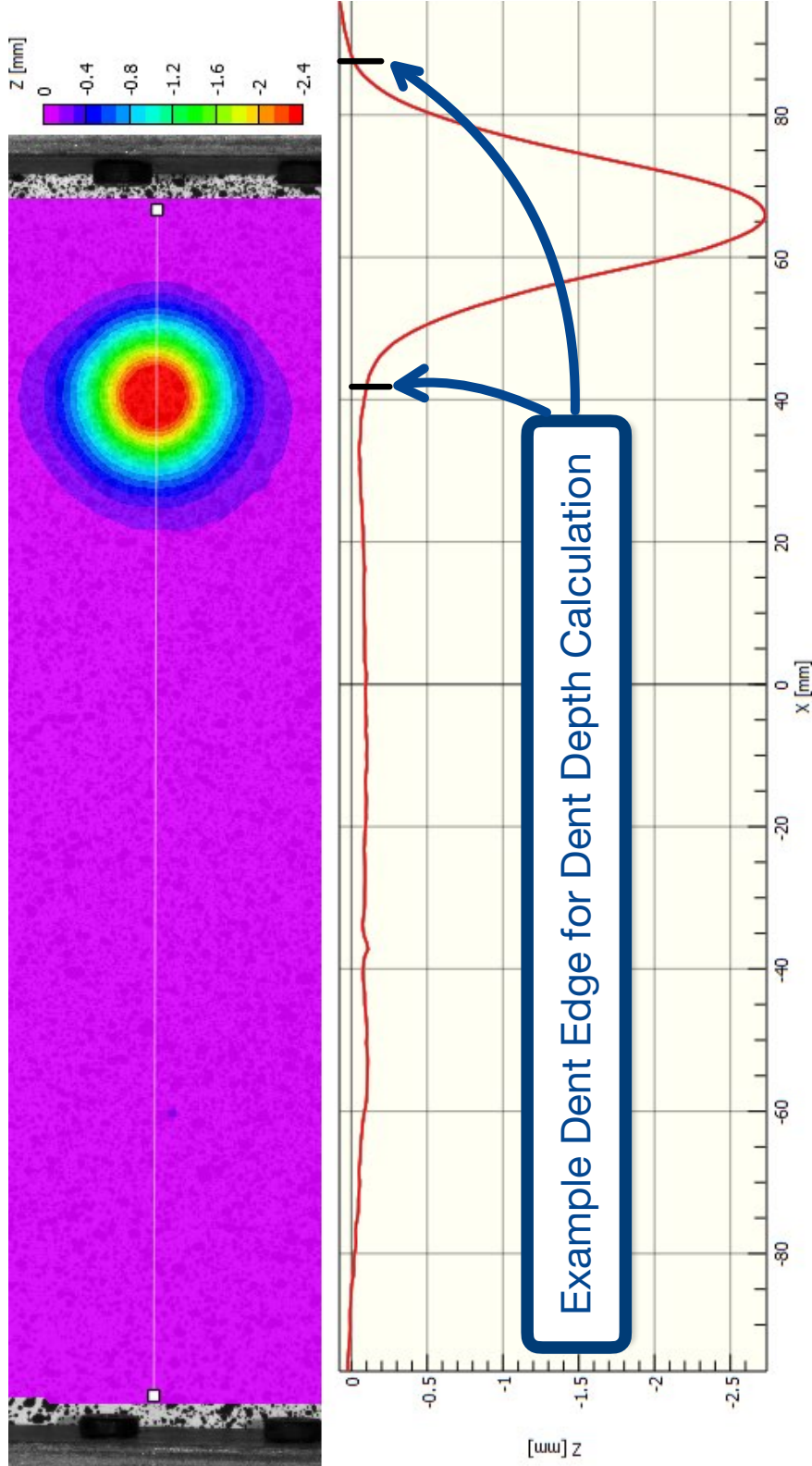


Figure 5.4: Dent depth measured with an inspection line in VIC-3D 9. The top portion shows an inspection line drawn across the panel that passes through the dent centre. Scale is indicating surface profile in z-direction (out-of-plane) from 0 mm (purple) to -2.4 mm (red). The bottom portion shows the extraction graph of that inspection line in a plot of z (mm) vs the in-plane horizontal coordinate, x (mm). Dent edges used for depth measurement are marked with black lines.

5.1.4 Panel Weights

The measured weights are presented in Table 5.4. Measurement of test panel weights is required by ASTM D8287 [13].

Table 5.4: Test Panel Weights.

Test Panel Serial	Dent Location	Weight (g)
2023-001	Centre	254
2023-002	Centre	261
2023-003	40 mm ED	267
2023-004	40 mm ED	257
2023-005	Centre	254
2023-006	40 mm ED	269
2023-007	60 mm ED	250
2023-008	60 mm ED	265
2023-009	60 mm ED	261
2023-010	50 mm ED	260
2023-011	50 mm ED	264
2023-012	50 mm ED	269
2023-013	No Dent	260

5.1.5 Dimensional Tolerance, Squareness and Far-Field Strain

Table 5.5 presents the results of the inspection and measurement practices of the test panels described in Section 4.4. The 0.25 mm dimension tolerances required by ASTM 8287 for measurements locations A through F were achieved. Additional diagonal measurements G and H were taken as an indication of squareness.

Figure 5.5 shows an example of alignment validation using 3D DIC results. The strain image shown is taken at an applied load of 7.7 kN, which is 10 % of the maximum expected load. The four extensometers, E0 (red), E1 (green), E2 (blue), and E3 (brown), are placed approximately 25 mm inside each corner, starting from the top left and moving clockwise. The plot in the lower half of the figure compares the index (frame at 2 Hz) on the x-axis with the engineering strain, $\Delta L/L_o$ on the y-axis.

Table 5.5: Test panel dimension inspection results. All dimensions are in mm.

<u>Test Panel</u>	<u>A</u>	<u>B</u>	<u>C</u>	<u>D</u>	<u>E</u>	<u>F</u>	<u>G</u>	<u>H</u>
Target	215.00	215.00	215.00	265.00	265.00	265.00	341.25	341.25
	± 0.25	± 0.25	± 0.25	± 0.25	± 0.25	± 0.25	-	-
2023-001	214.93	214.82	215.20	264.99	264.86	265.04	341.28	340.80
2023-002	214.87	215.02	215.25	265.18	265.11	265.22	341.15	341.00
2023-003	215.02	214.99	215.03	265.17	265.02	265.02	341.40	341.38
2023-004	215.13	215.15	215.13	265.21	264.98	265.15	341.24	341.46
2023-005	214.96	215.01	215.01	265.04	264.94	265.05	341.12	340.50
2023-006	215.08	215.05	215.23	265.12	265.25	265.09	341.22	341.00
2023-007	214.82	215.07	215.19	265.16	264.90	265.22	341.18	340.90
2023-008	215.00	215.16	215.12	265.21	265.25	265.20	341.18	341.48
2023-009	215.05	215.13	215.22	265.15	265.12	265.15	341.10	340.90
2023-010	214.98	215.19	215.23	264.84	264.91	264.96	340.74	340.80
2023-011	215.08	214.86	214.98	265.10	265.13	265.03	341.00	341.60
2023-012	215.07	215.10	215.17	265.17	265.16	265.14	341.38	341.00
2023-013	214.97	215.05	215.01	265.15	265.10	265.10	341.10	341.08

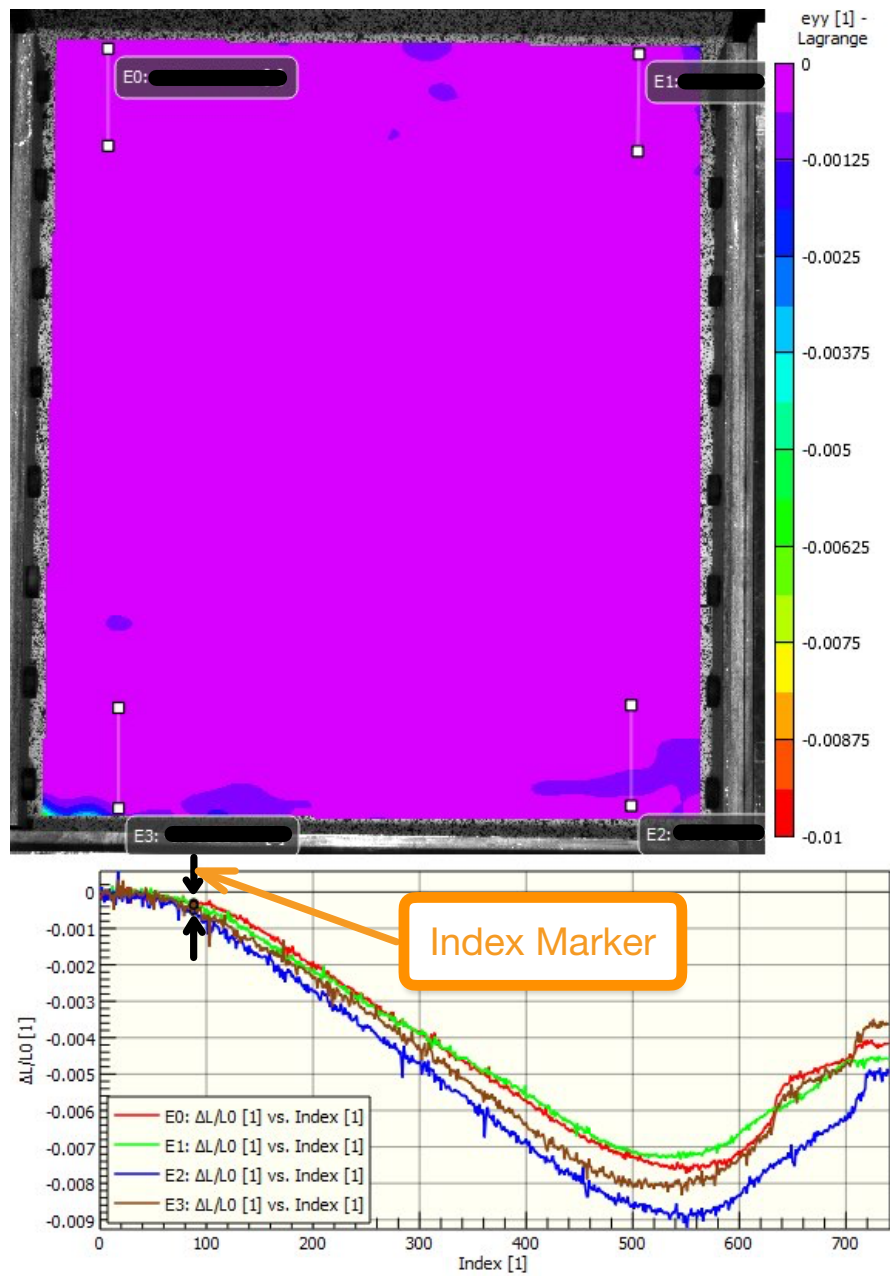


Figure 5.5: Vertical strain, e_{yy} , and four 30 mm extensometers (E0, E1, E2, and E3) with extraction data strain vs. index (frame) plot are shown for test panel 2023-003 at 7.5 kN load. The 7.5 kN load occurs at index (frame) 88, marked with a small black dot on the strain-index plot.

In these extensometer results, the same relatively high scatter can be seen as was seen on the strain validation extensometer presented in Section 5.1.2. Comparison of the strain measured by the top extensometers, E0 (red) and E1 (green), finds strong agreement between the two throughout the test. The two bottom extensometers, E2 (blue) and E3 (brown), agree well; however, there is more spread than in the top pair. Similar results were observed in the other test panels. In the bottom pair, the extensometer on the right side measures more strain. In the top pair, the right extensometer starts measuring slightly more strain but as the total strain increases, the left extensometer begins reading more strain.

An advantage of the 3D DIC system is access to full-field vertical strain and facesheet deformation data. In Figure 5.5, a compressive strain concentration can be seen in both lower corners of the facesheet, the bottom left corner being the strongest. However, as the test progresses, these strain concentrations become increasingly small compared to the high and low strain concentrations caused by panel damage. For example, a similar compressive strain concentration can be seen in the lower left corner of Section 5.4's Figure 5.14. The concentration is visible in frames 150, 250, and 300. However, around frames 350 and 400, the strain concentration becomes relatively small compared to the strain concentrations in the damaged area. The failure mode does not appear to be affected by the strain concentration in the bottom left corner. In fact, the strain concentrations in the lower left corner of these two panels may be caused by the asymmetry of the damaged panels itself. Over the panel height, the damaged (right) side of the panel is likely slightly less rigid in compression than the undamaged (left) side. The dented side of the test panel can be deformed out of plane in addition to compressive strain in response to compression loads, where the undamaged side responds to compression loads almost entirely through compressive strain.

5.2 Residual Strength

Figure 5.6 presents force-displacement data collected by the MTS system during CAI testing. Because these tests are compressive and in keeping with sign conventions, displacement and loads are presented in all figures as negative values. The loads were aligned at 5 kN rather than 0 kN to account for the settling of the sandwich panels. Figure 5.7 presents the same force-displacement data, but zooms in on the area where the maximum resistive loads and failure occur. Three test panels for each of the four damage configurations are reflected in the graph: centre dents in black, 60 mm ED in blue, 50 mm ED in orange, and 40 mm ED in green. The force-displacement behaviour of all panels is very similar below approximately 60 kN and 1.5 mm of compressive force and displacement. Above approximately 60 kN, the resistive force of the panels increases more slowly relative to displacement, and failures begin to occur. The

net section yield force for these panels is 59 kN (see Equation 4.2). Both the residual strength and the displacement of all damaged panels are significantly lower than those of the single undamaged panel tested. These results are further analysed in Section 6.2.

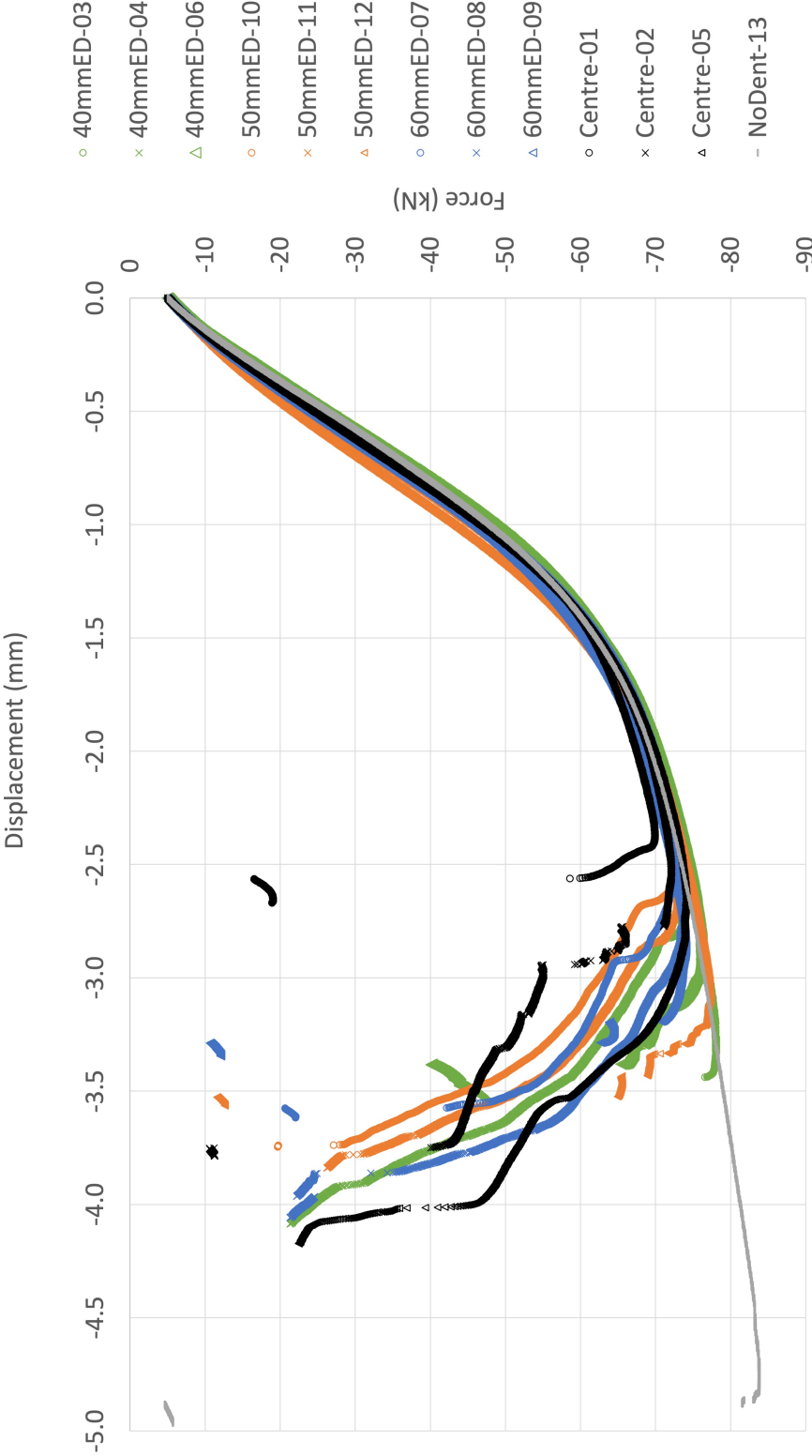


Figure 5.6: Force-displacement CAI Performance. Force and displacement are measured by and collected from the MTS compression apparatus.

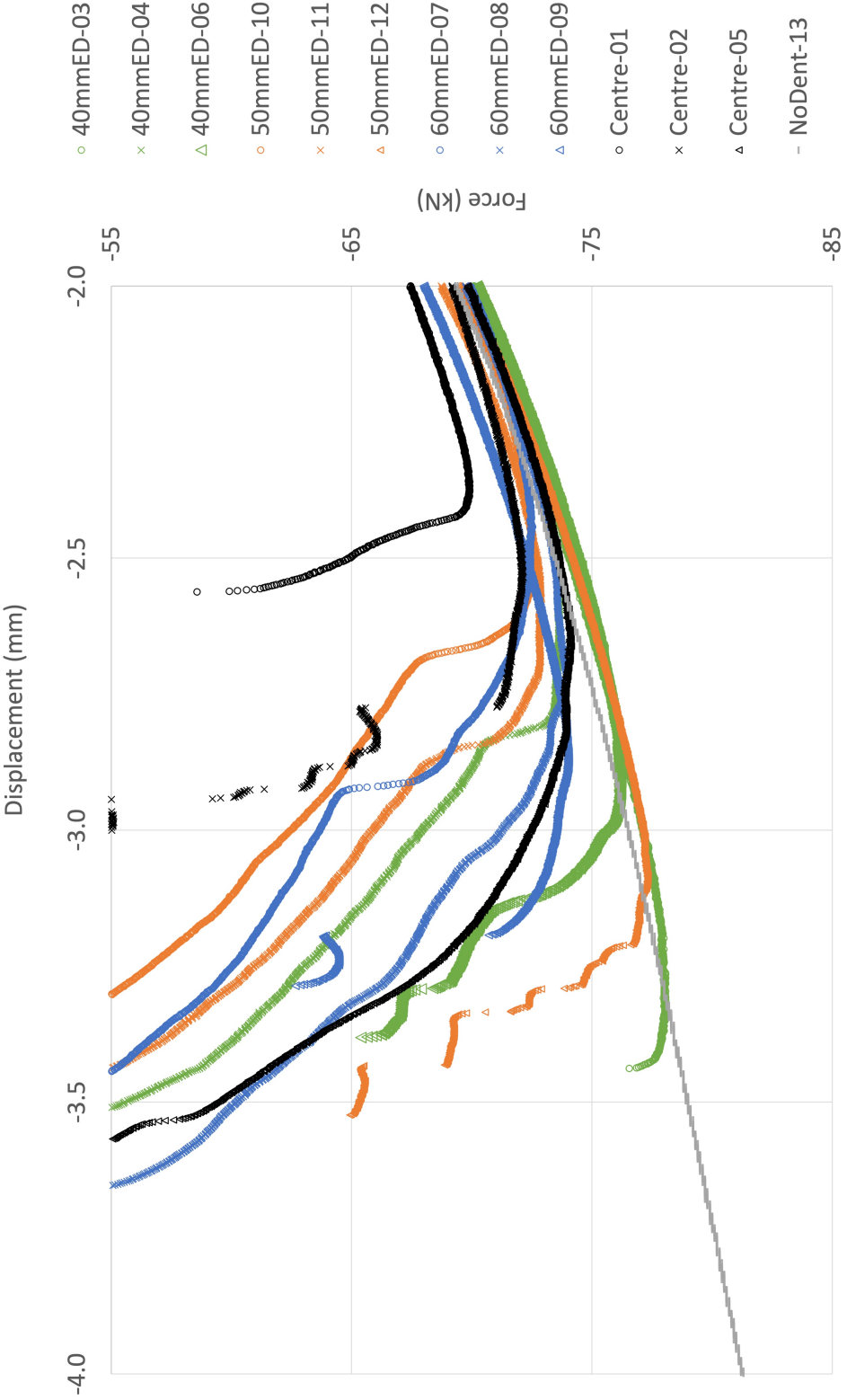


Figure 5.7: Zoomed view of the differentiation area for force-displacement CAI Performance presented in Figure 5.6.

5.3 Failure Mode and Deformation

3D DIC was used to measure the profile of the facesheet in each frame (2 Hz) of the test; however, the analysis of the results will only focus on the size and width of the dent under the non-load conditions (original), the net section yield, and the maximum load. A dent threshold of 0.25 mm was used to differentiate undented from dented areas of the facesheet. The size and width of the dent used for the deformation analysis is calculated using this threshold.

Figures 5.8 to 5.11 present the dent sizes for all dented test panels under original, net section yield, and peak load conditions. As introduced in Section 4.8, the facesheet profile images were created in VIC-3D 9; however, ImageJ was used to scale the profile images and analyse the dents. Due to the combined effect of the knife edge that covers part of the test panel, lighting, camera field of view, and the limits of the DIC system, the edges of the panels are 5 to 15 mm outside of the facesheets represented in Figures 5.8 to 5.11.

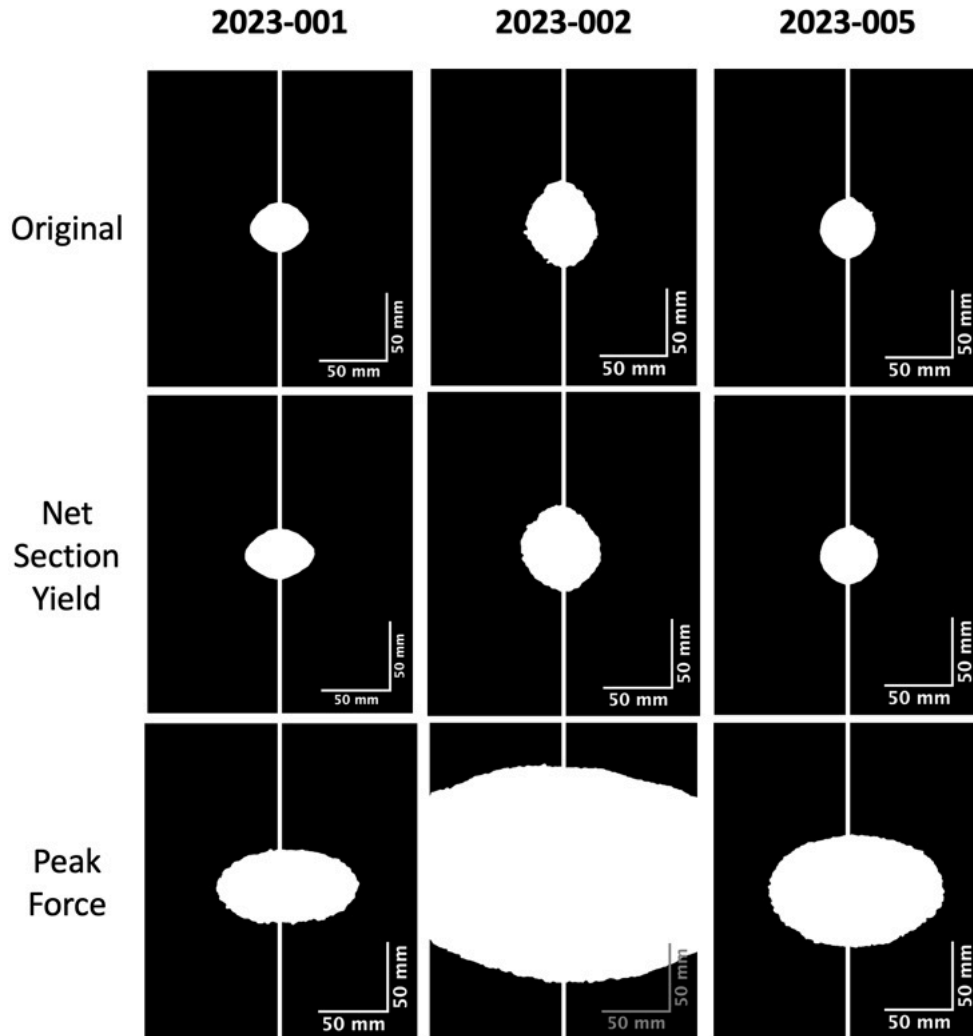


Figure 5.8: Centre dent deformation. Black identifies flat facesheet. White identifies a dented area of at least 0.25 mm depth. The scale bars are 50 mm. The white vertical line marks the panel centre.

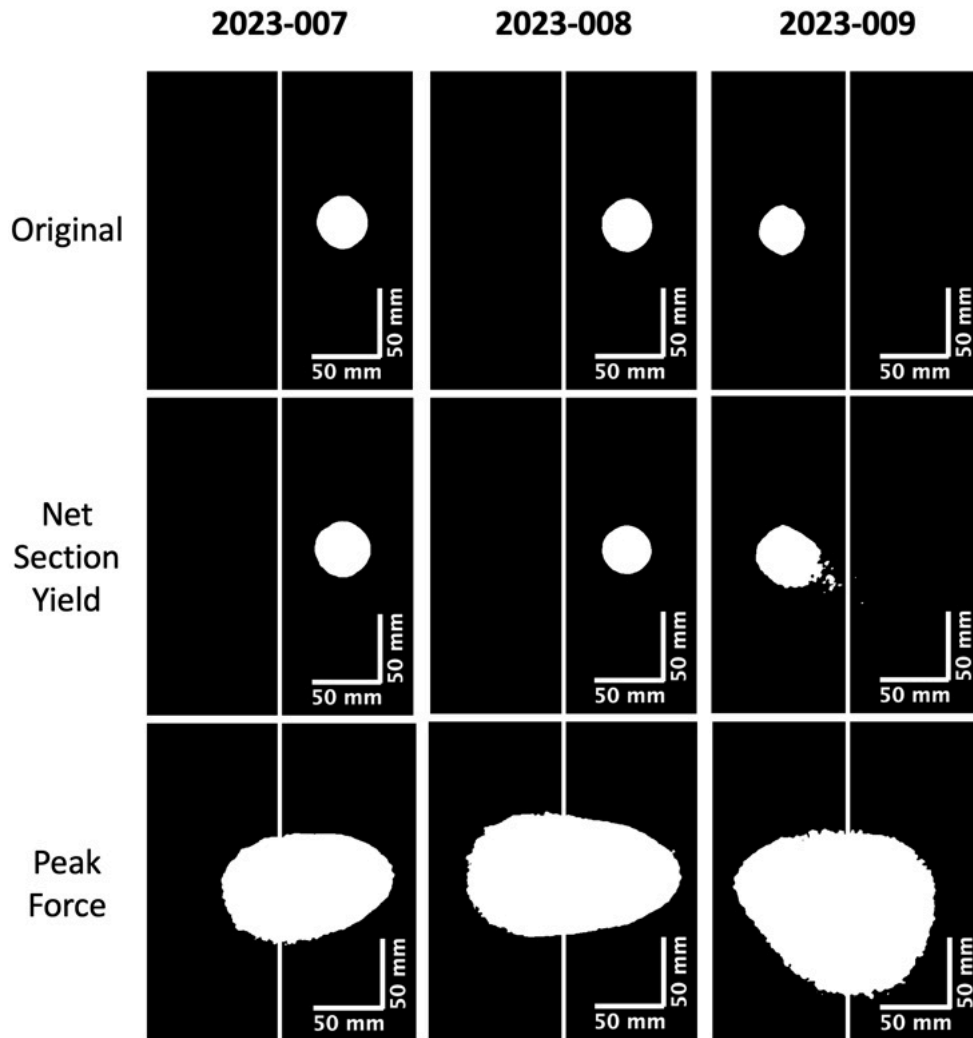


Figure 5.9: 60 mm ED dent deformation. Black identifies flat facesheet. White identifies a dented area of at least 0.25 mm depth. The scale bars are 50 mm. The white vertical line marks the panel centre.

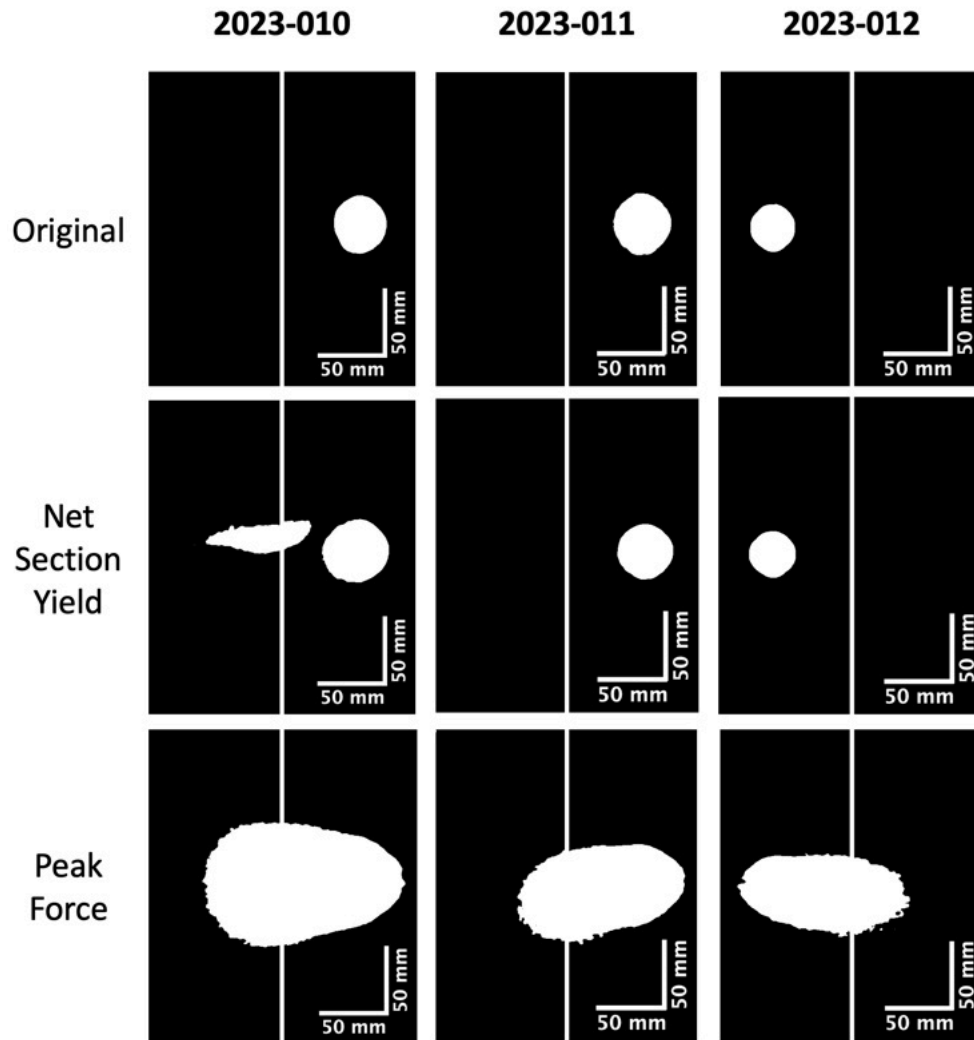


Figure 5.10: 50 mm ED dent deformation. Black identifies flat facesheet. White identifies a dented area of at least 0.25 mm depth. The scale bars are 50 mm. The white vertical line marks the panel centre.

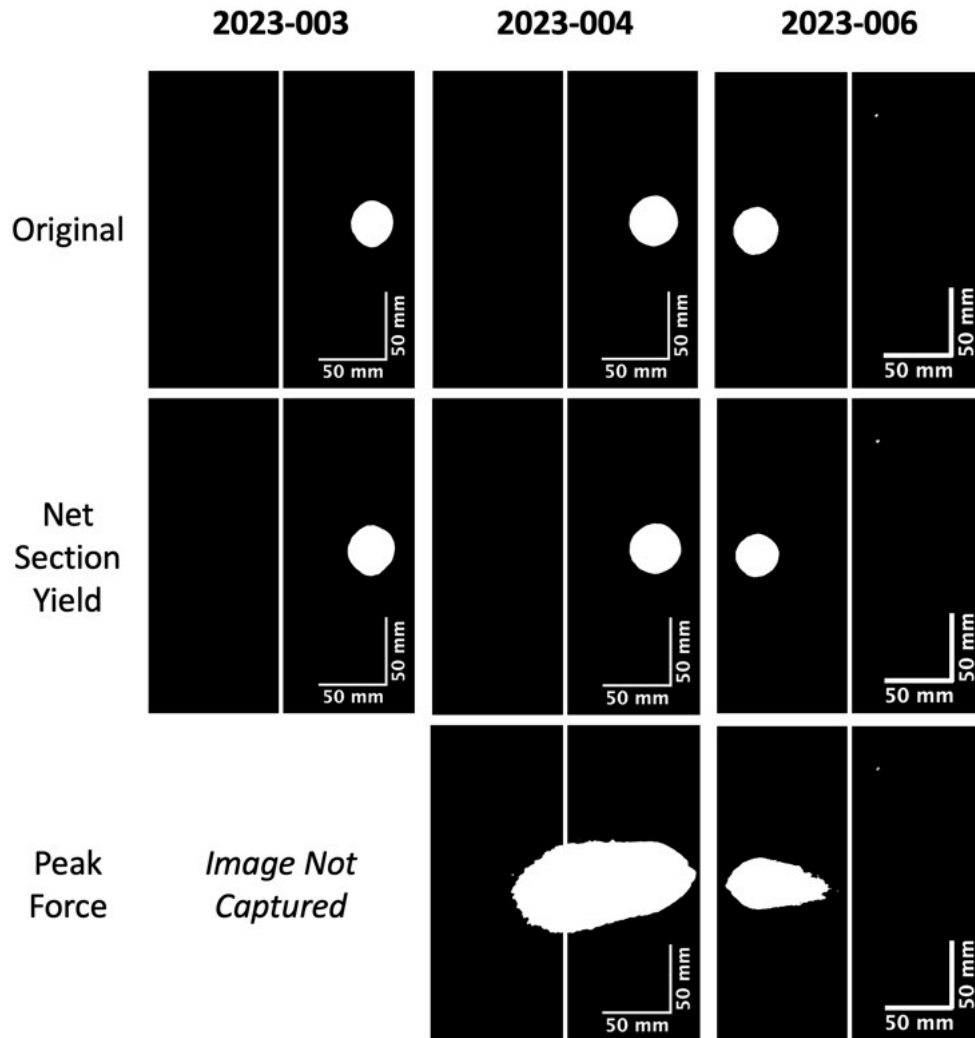


Figure 5.11: 40 mm ED dent deformation. Black identifies flat facesheet. White identifies a dented area of at least 0.25 mm depth. The scale bars are 50 mm. The white vertical line marks the panel centre.

With every test panel, the measured dent shape is near circular in the non-load (original) condition. As the impactor used to create the dent was spherical, this matches expectations. The size of the dent remains the same or increases slightly under the net section yield condition. There is little to no out-of-plane deformation of the facesheet below net section yield loads. The size of the dent increases significantly between the net section yield and peak force. In all cases, the dent grows more in width than in height. In the centre dent, the growth of the dent is symmetric. In all non-centre cases, the dent

growth is asymmetric: the dent grows more toward the centre of the panel than toward the edge of the panel.

Figures 5.12 and 5.13 present the test panel condition following CAI tests. All failures initiated at the dent and spread to the left and right perpendicular to the load direction.

The dented facesheet deformation during failure was classified into one of two variations. In 42% of the cases, variation (i) occurred in which some or all deformed areas outside the original dent deformed outward, away from the honeycomb core. In 58% of the cases, variation (ii) occurred where all deformed areas outside the original dent were deformed inward, into the honeycomb core. The areas where the facesheet deformed outward are boxed in blue in Figure 5.12, while the areas where the facesheet deformed inward are circled in red. There is no relationship between these failure modes and the damage edge distance or the location of the dent in the support fixture (left or right of centre).

All rear (originally undamaged) facesheets deformed outward but were restrained at the knife edge (see Figure 5.13).

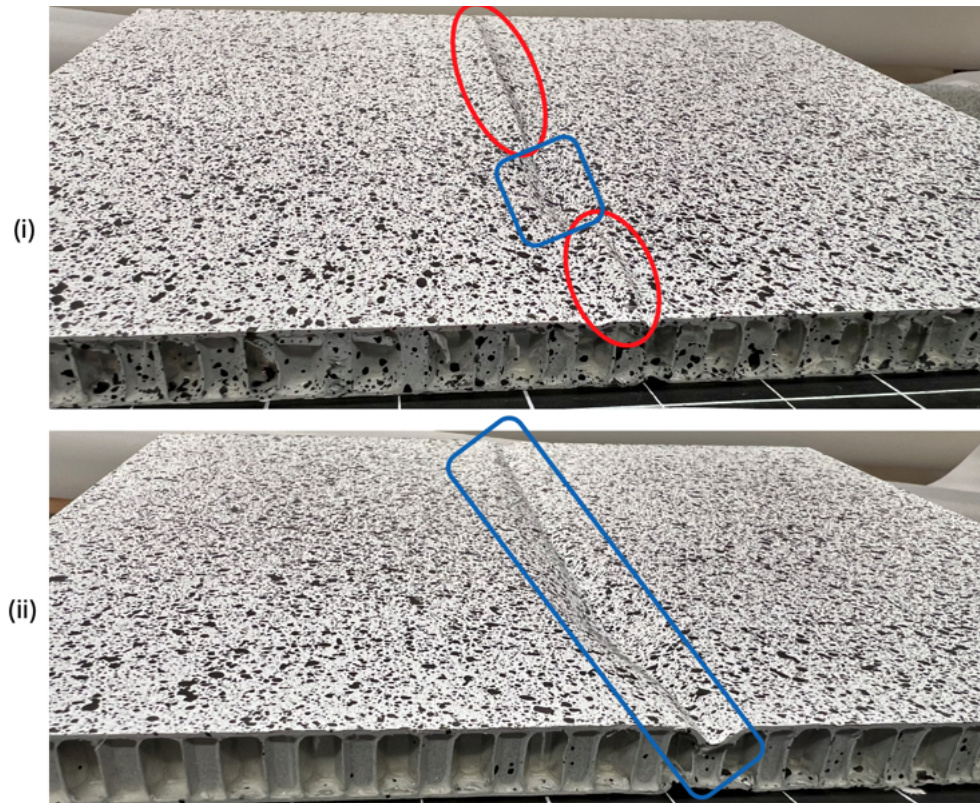


Figure 5.12: CAI failure mode variations of dented sandwich panels. Variation (i) is characterized by outward deformation of the damaged facesheet in addition to the inward deflection in the dent area. Variation (ii) is characterized by having only inward deflection of the damaged facesheet. Outward deflections (positive Z) are circled in red. Inward deflections (negative Z) are boxed in blue.

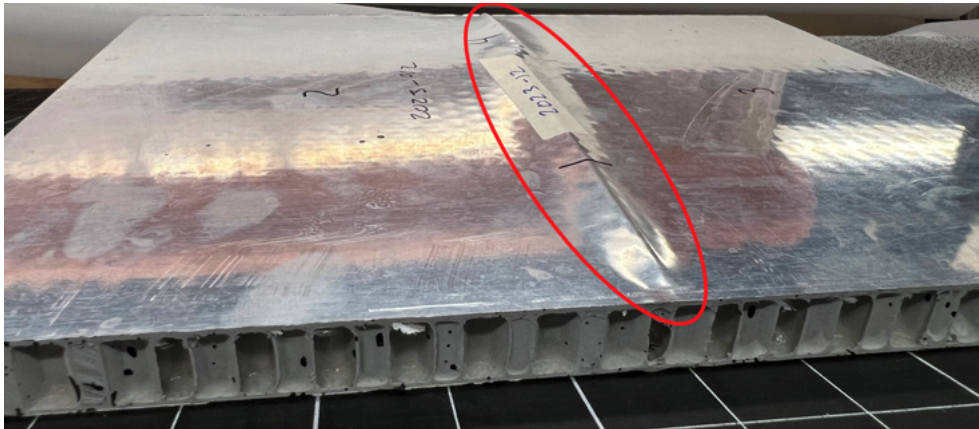


Figure 5.13: CAI failure mode on the back facesheet were all very similar. The facesheet deformed outward in a Euler macrobuckling manner (see Figure 3.2 (a)). but the knife edge prevented full outward deformation at edged. In the foreground, a mark made by the rear knife edge onto the panel is visible.

5.4 Facesheet Strain

VIC-3D 9 can calculate and present strain information in several ways. As mentioned in Chapter 4, this paper only considers the vertical Lagrangian strain, e_{yy} . Facesheet e_{yy} results from VIC-3D 9 can be presented in a variety of ways, including two- and three-dimensional representations, videos, and images, all with a number of contour scales. Figure 5.14 presents 14 images of a two-dimensional contour strain representation. 16 colour gradients are used to represent the strain contour from 0 to -4% strain. The 14 images are e_{yy} for every 25 seconds of a 40 mm ED CAI test (image 50, 100, 150, etc.). As the compression of the test panel progresses, the strain increases more or less evenly in the first frames. In image 250, the low strain areas immediately above and below the dent are clearly visible and the high strain areas on either side of the dent quickly grow into the highest strain areas. The net section yield force occurs at frame 276, between frames 250 and 300 which are shown. The peak force occurs at frame 478, between frames 450 and 500 which are shown. The elongated strain concentrations on either side grow outward as the panel deforms. The growth of the deformation and strain concentration on the right edge is restricted by the knife edge support much earlier, and the deformation and strain grow relatively unrestricted on the left side of the dent. At the same time, the lower strain areas above and below the dent grow asymmetrically, toward the knife edge support. This suggests that an increasing amount of load is being carried by the left (undamaged) side of the panel, and, potentially, load is being transferred into the knife edge support. The facesheet strain immediately adjacent to and below the knife edge is not visible to the DIC system.

Figures 5.15 through 5.18 show facesheet strain behaviour using a binary strain contour about the facesheet yield strain, ϵ_y , of 0.37% strain. ϵ_y is calculated as presented in Equation 5.8. The areas in white are below ϵ_y and considered elastic strain, while the areas in black are above ϵ_y and considered plastic strain. σ_y and E are taken from Matweb [58].

$$\begin{aligned}\epsilon_y &= \frac{\sigma_y}{E} \\ &= \frac{270 \text{ MPa}}{73.1 \text{ GPa}} \\ &= 0.0037\end{aligned}\tag{5.8}$$

In all cases, the elastic strain area reduces between net section yield and peak load, leaving a small elastic strain area immediately above and below the dent. In some cases, imperfections in the test panel are highlighted by a variation in the local strain behaviour. Test panel 2023-002 has a clear example of this. The elastic deformation area in the bottom left quadrant at peak force was a small imperfection (less than 0.5 mm out of plane) on the facesheet

not found during fabrication but visible here in the strain results and in the deformation image from the very first frame of the DIC analysis.

At peak load, the elastic strain areas in the immediate vicinity of the dent do not exhibit asymmetry using the single yield strain threshold analysis. The strain asymmetry is visible at the peak load using different thresholds such as in Figure 5.14. In some cases, such as with test panels 2023-008 and 2023-006, elastic strain behaviour around the dent at net section yield does indicate asymmetry. With these test panels, the elastic strain area is larger and slightly curved toward the knife edge.

Figure 5.19 presents the most dramatic illustration of the asymmetric strain for each dented test panel. These images were selected case by case, but all are following peak load, where the residual strength decreases, but catastrophic failure has not yet occurred. Black identifies areas in plastic strain, while white identifies elastic strain. For the centre dents, no significant asymmetry was observed. An asymmetric strain for the centre dents should only be present if the test support fixture or the test panel was asymmetric. As presented in Sections 5.1.5 and 6.1, the test support fixture and test panels were sufficiently square and aligned to characterize the effects of the damage edge distance.

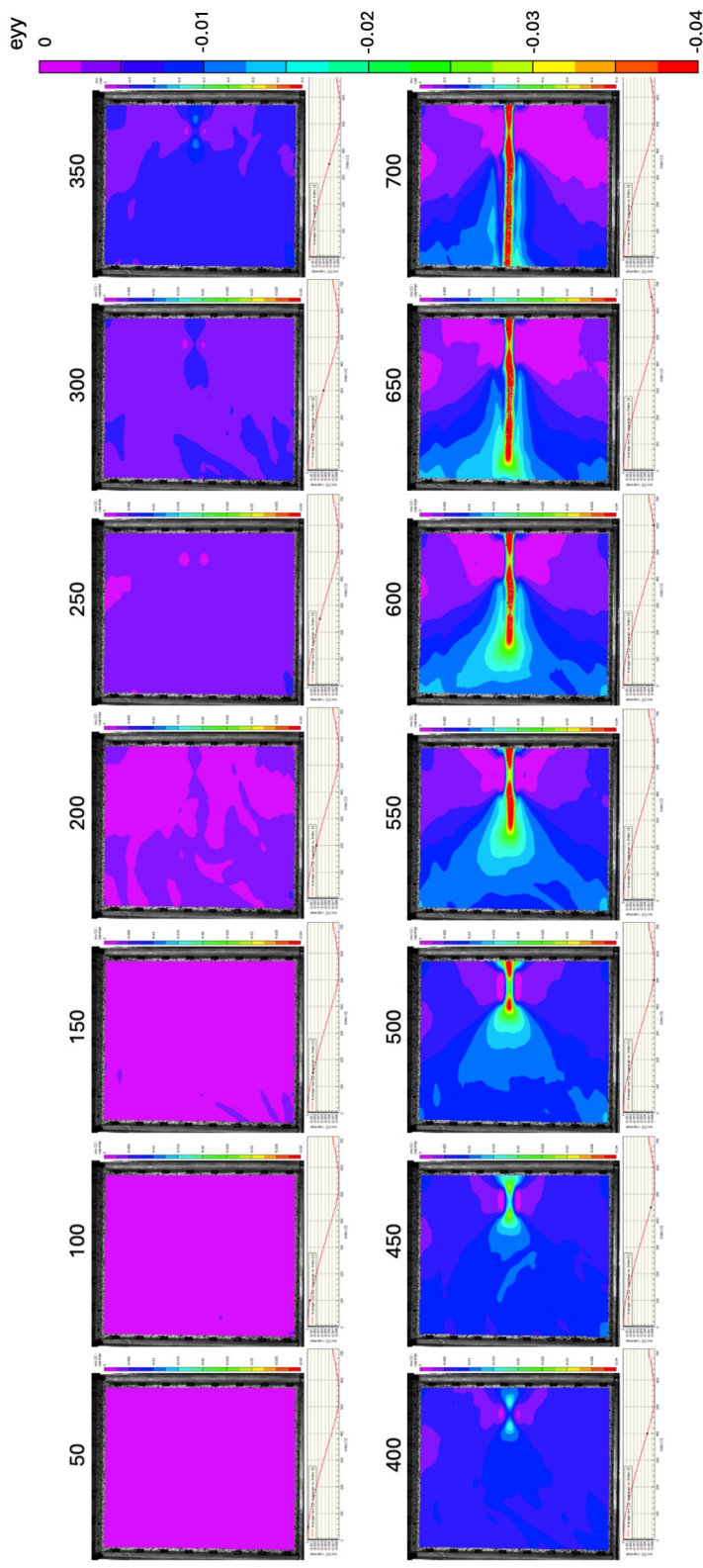


Figure 5.14: Vertical Lagrangian strain, ϵ_{yy} , behaviour of test panel 2023-004 is shown using a 16 colour gradient representing 0 to -4% strain. The 14 images capture every 25 seconds of the test (every 50 frames at 2 Hz). The net section yield force occurs in frame 276. The peak load occurred in frame 478.

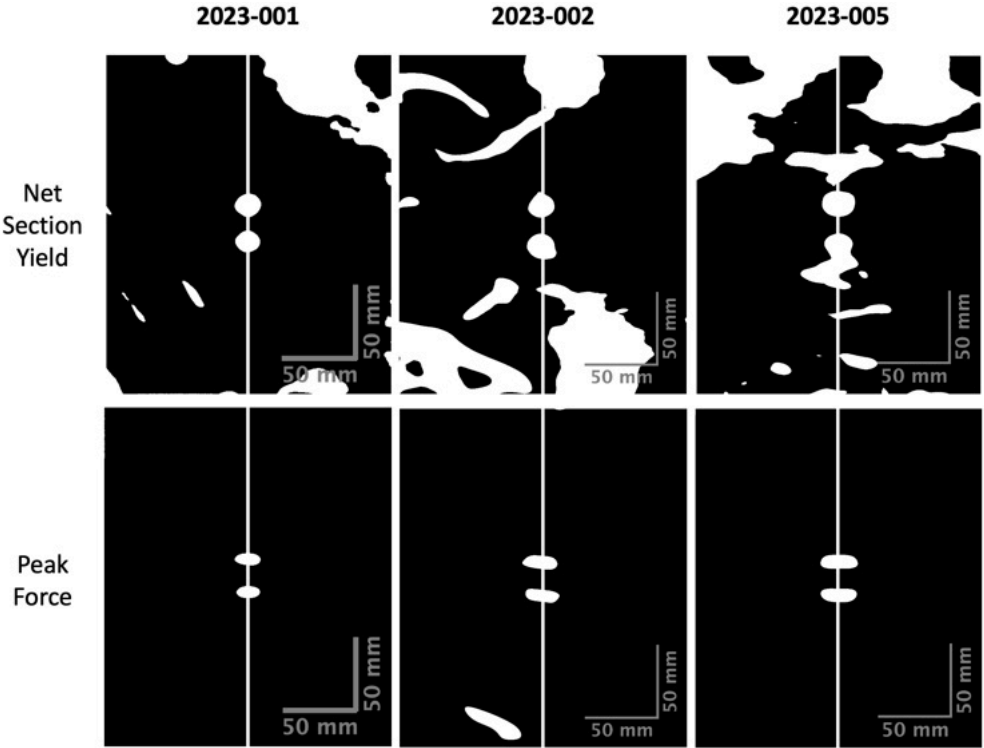


Figure 5.15: Centre dent strain. Black identifies area in plastic strain while white identifies areas under elastic strain. Scale bars are 50 mm. The vertical white line marks the panel centre.

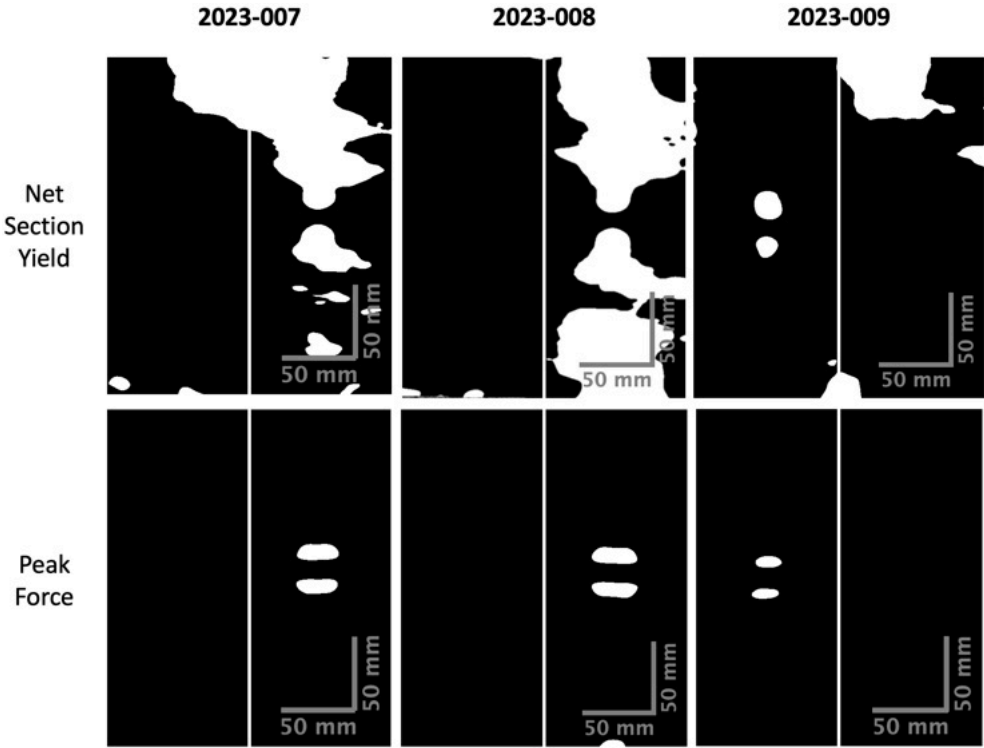


Figure 5.16: 60 mm ED dent strain. Black identifies area in plastic strain while white identifies areas under elastic strain. Scale bars are 50 mm. The vertical white line marks the panel centre.



Figure 5.17: 50 mm ED dent strain. Black identifies area in plastic strain while white identifies areas under elastic strain. Scale bars are 50 mm. The vertical white line marks the panel centre.

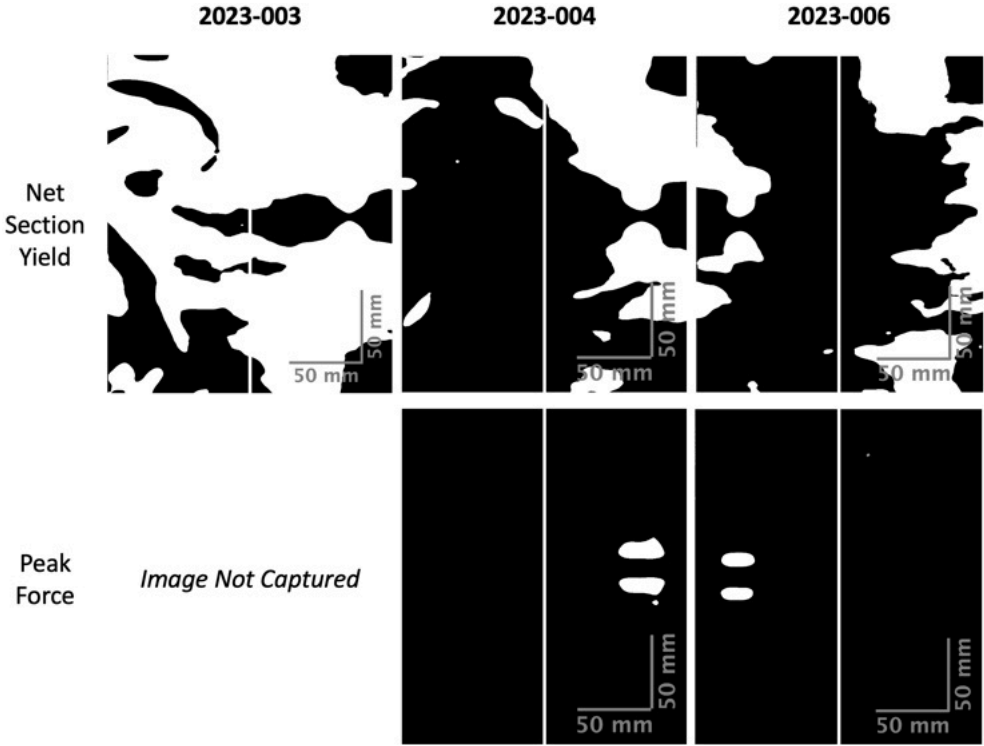


Figure 5.18: 40 mm ED dent strain. Black identifies area in plastic strain while white identifies areas under elastic strain. Scale bars are 50 mm. The vertical white line marks the panel centre.

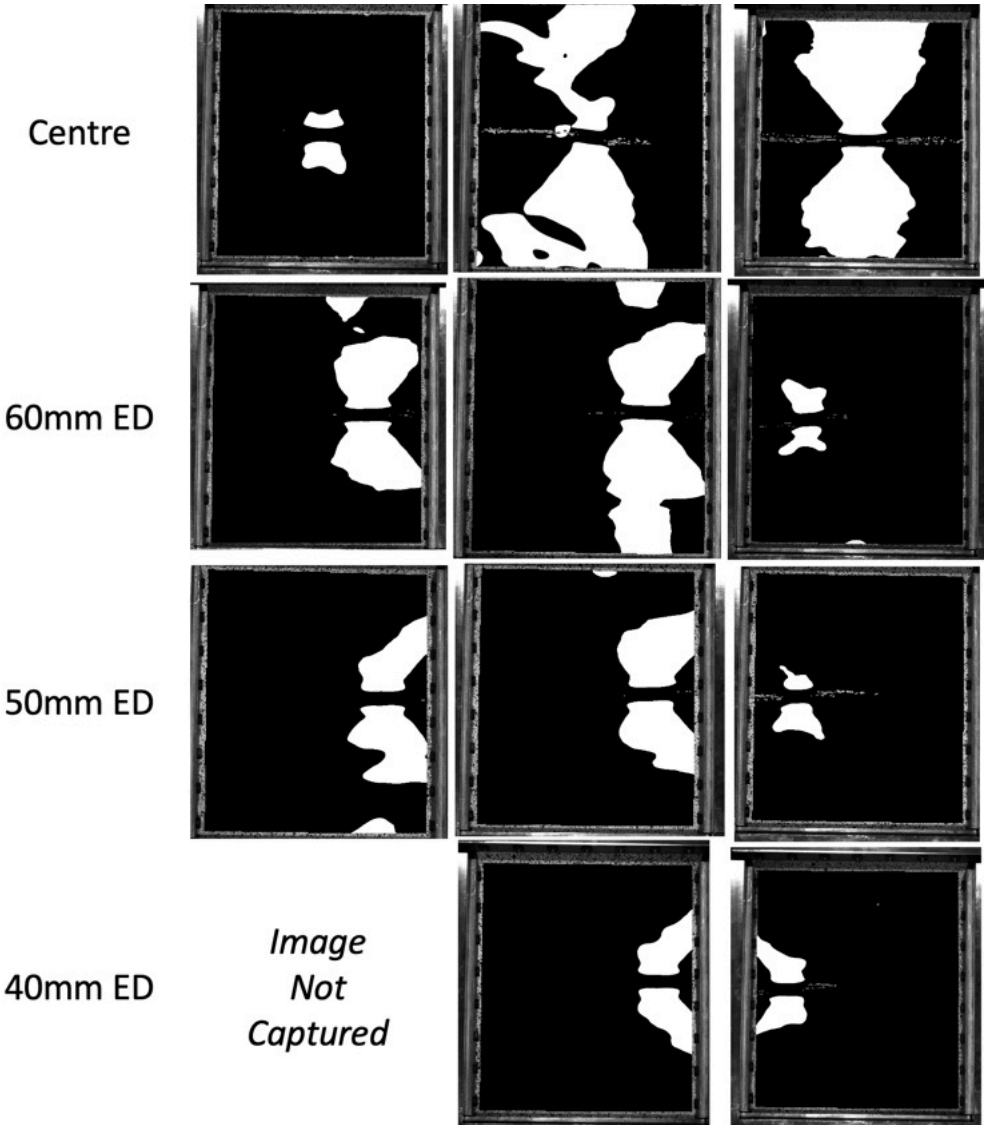


Figure 5.19: Observed asymmetry for 40 mm, 50 mm and 60 mm ED panels in strain distribution following peak load. The centre dent panels do not show asymmetry. Elastic strain areas are coloured white while plastic strain areas are coloured black.

5.5 Stress-Strain Behaviour

The stress-strain properties of materials are a commonly used metric, as these properties can be critical for material selection by engineers in the design process. The experimental measure of the stress-strain relationship of contiguous materials is usually achieved by creating a relatively long and thin test specimen with a narrow test section with constant cross section, gripping either end, and applying known tensile load while measuring the overall change in length of the test section. In the case of a structural composite, such as sandwich panels, where the composite is not contiguous, several additional challenges are present in the experimental measurement of the stress-strain properties. The combined use of load cell and DIC data provides an opportunity to calculate the effective stress-strain properties exhibited by sandwich panels in CAI.

In this experiment, the strain is measured using the DIC results. The average vertical Lagrangian facesheet strain, e_{yy} , will be used as the strain value.

Stress is calculated using the applied load data captured by the load cell in the MTS system. Using the initial cross-section area of the two facesheets and the load information collected from the load cell, we can calculate the engineering stress for each data point using Equation 5.9.

$$\sigma_{eng} = \frac{F}{A}, \quad (5.9)$$

The stress-strain results are presented in Figures 5.20 and 5.21. As the 3D DIC datasets were incomplete for test panels 2023-003 and 2023-013, the stress-strain values for these panels are not fully included in these two figures. These figures illustrate an interesting curl-type behaviour in the stress-strain data following failure of some panels where as stress decreases, the average facesheet strain also decreases. This is especially present in the centre dent test panels 2023-002 and 2023-005 which failed less abruptly. This phenomenon may be caused by the increased presence of tension strain in part of the dented facesheet as it fails and wrinkles. There may be a correlation between this curling in the stress-strain data and the direction of facesheet wrinkling presented in Figure 5.12. Further research in this area is recommended. The analysis of the elastic region of these results is presented in Chapter 6.

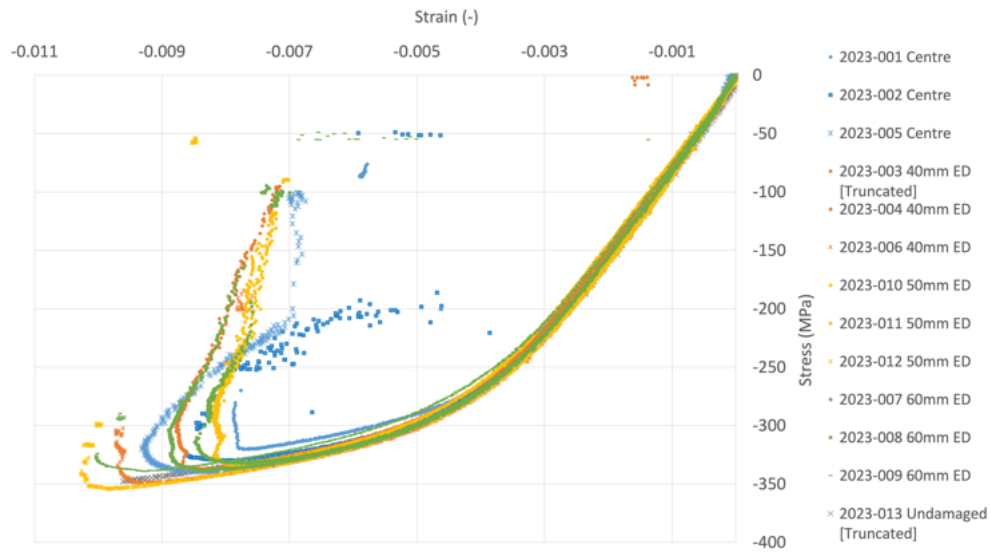


Figure 5.20: Stress-strain CAI performance. Stress is calculated using load cell data. Strain is calculated using DIC average e_{yy} data.

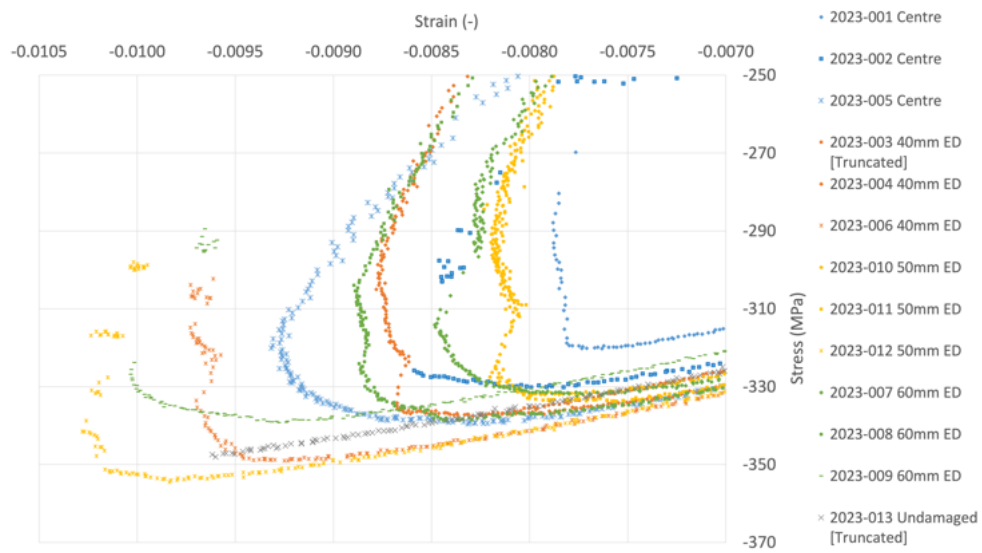


Figure 5.21: Zoomed view of the differentiation area for stress-strain CAI performance presented in Figure 5.20.

6 Discussion, Analysis and Recommendations

6.1 Development of Test Methodology

ASTM D8287 was successfully adapted for 3D DIC data collection and for characterizing damage edge distance effects. The fabrication, indentation, data collection, strain validation, and CAI test are discussed and analysed.

6.1.1 Test Panel Fabrication

Panel Cutting

The final dimensions of the test panel presented in Table 5.5 were within the tolerances required by ASTM D8287 [13]. Some of the corner or edge strain concentrations observed in the test panels during CAI tests can be attributed to the fabrication of the panel, but none of these are evaluated as significant enough to inhibit meaningful characterisation of the effects of the damage edge distance effects.

The rough and final cut processes were capable of achieving the desired panel dimensions. Properly set with a straight edge as a guide and masking tape to protect the facesheet, the skill saw was a cheap, fast, and effective tool for rough cutting of the panels. During prototyping, water jet cutting was tested as an alternative rough cut solution. The results were poor by comparison. More sandwich panel material was wasted due to cell wall damage. The wet tile saw used for the final cutting required only small adjustments to cut sufficiently square. It operated smoothly but required care and attention during operation to ensure that the guide bed and frame did not twist or affect the quality of the cut.

Several mitigation measures were implemented to achieve these results. The jigs that were created and used for final dimension cuts were instrumental in calibrating the cut length and then achieving that calibrated cut length repeatedly. Any simple jig without flexion and with the capability for fine adjustment is suitable, provided that it can be fixed once calibrated and repeatedly secured to the moving base plate in precisely the same location.

Repeated quality control checks throughout the panel cutting process ensured that errors were captured and addressed early in the fabrication process. Small cutting errors have the potential to compound during fabrication.

End Potting

The construction adhesive used for end potting was easy to work with during application and was much better to work with once cured as opposed to the epoxy, which would become sticky and difficult to remove by sanding. Once it was cured, the construction adhesive could be worked much like wood. The final sanding process with the machinist block worked well but may have allowed imperfect squareness and flatness of the edges. Alternate final adhesive shaping methods could be explored to limit the possibility of imperfection due to human error. It may be possible to complete the final adhesive shaping on the potted edges with a mill or plane to achieve better results than were achieved with sanding.

None of the test panels failed in the end potting area. The end potting did not appear damaged after CAI and no test panels experienced edge curling. The construction adhesive used was effective in providing the compression edges of the sandwich panel with the required support.

The closest failure to end potting was the wrinkling of the facesheet of the undamaged panel at the small vertical edge of the unsupported section between the upper and lower portions of the support fixture shown in Figure 6.1. The wrinkles began at the vertical edges of an open cell and spread inward. Figure 6.1 shows a wrinkle that started at the left edge of the test panel in the foreground. In the background, a second wrinkle is visible in the out-of-focus area that initiated a row of cells lower on the test panel. This failure is likely not caused by failed end potting. The left-initiated wrinkle occurred in the open cell located against the upper edge clamp of the support fixture. The upper edge clamp may have contributed to a stress concentration in the facesheet. However, the second wrinkle appeared to occur one cell row further down. It would not have been directly affected by the top edge clamp; however, it may have been affected by the proximity of the top end of the right-hand knife edge support. A stress concentration may have been created at that interface. This wrinkling failure of the test panel facesheet corresponds to the 70 kN drop in load of the sandwich panel 2023-013 shown in Figure 5.6.

6.1.2 Test Panel Indentation

The dents created in the indentation process were not identical in depth and width as measured by either of the measurement processes (see Tables 5.2 and 5.3). However, considering the results of the manual dent measurement alone and the performance of the dented sandwich panels in CAI testing, the dents created were sufficiently consistent in shape, depth and width for the purposes

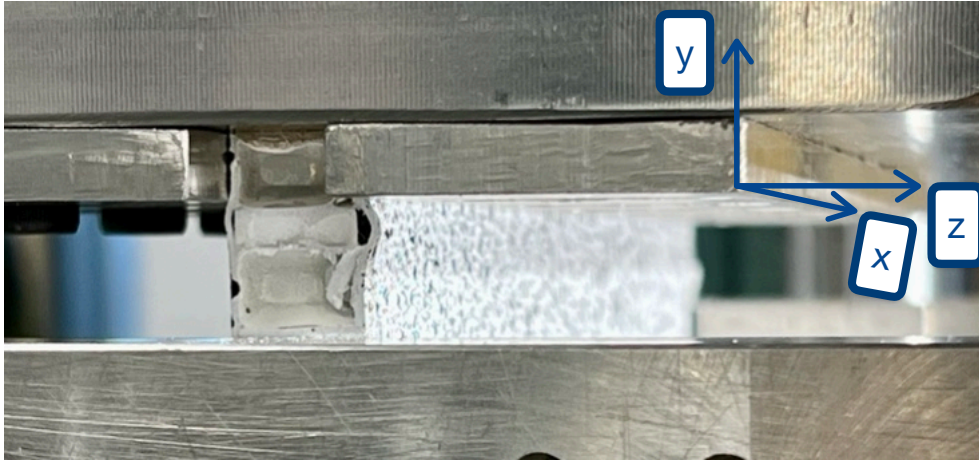


Figure 6.1: Facesheet wrinkling was observed near the top edge of the undamaged test panel, in the unsupported section at loads above 80 kN.

of this research. The spherical impactor worked well to create round, smooth dents. The drop tower was adequately accurate in dent placement. The base plate and holding clamps worked well. No panel movement occurred during impacts. Panel placement was easily performed, including the various edge distances.

Although adequate for these research purposes, the drop tower design could be further improved with greater control of the drop section and measurement of the speed of the drop section so that the impact energy could be better monitored. Many commercial drop weight tester solutions can be purchased for this purpose [59].

Traditional measurements and 3D DIC measurements yielded similar dent depth results. The average dent depths achieved (2.58 mm and 2.56 mm) were within 2% error of the target dent depth of 2.54 mm. The standard deviations of 0.13 mm and 0.14 mm represent about 5% standard deviation.

The dent widths according to the manual dent measurements were also consistent. The target width of the dent was 43 mm. The average manual dent measurement was 44 mm with a standard deviation of 1 mm. Measurement of dent width using 3D DIC deformation data and ImageJ approached dent edge definition in a different way than manual measurement. For digital dent width measurements, the dent edge was defined by the 0.25 mm deformation threshold presented in Section 4.8. The average dent width of 38 mm with a standard deviation of 6 mm obtained from 3D DIC and ImageJ was further from the target dent width of 43 mm than manual measurements and had much more variation. Selecting a slightly smaller deformation threshold to define the contour of the dent, as previously discussed in Section 5.1.3, may

increase the measured width of the dent, but may not improve the standard deviation.

The 3D DIC dent depth and width measurement is not known to be an approved aircraft inspection standard, while the manual dent depth measurement is a common sandwich panel dent measurement technique. Reyno et al. confirmed that manual dent measurements are subject to interpretation and can vary in result [60]. A more systematic and repeatable approach to dent measurement by 3D DIC, particularly in dent width measurement, would be required before it could be considered as a reliable and accurate dent measurement method. Any further use of digital acquisition for dent depth measurement should also consider investigating the use of 3D scanners for inspection of sandwich panel facesheet damage starting with Reyno et al. [60].

6.1.3 3D DIC

The 3D DIC system provided facesheet strain and full-field facesheet deformation information that would have been extremely difficult, if not impossible, to replicate using traditional instruments. The 3D DIC system from Correlated Solutions used for the testing was relatively easy to learn and set up; however, it proved challenging to achieve a calibration score in the range of 0.02 to 0.05. However, for the purposes of this research, the slightly lower out-of-plane resolution from the achieved calibration scores (0.058 mm to 0.064 mm) were sufficient to characterize the effects of the damage edge distance. Further use of 3D DIC should increase the number of calibration images captured significantly and be more liberal in manually removing poor image results to achieve a greater number of high-quality calibration images for final calibration.

The application of the speckle pattern with spray paint was visually assessed as evenly distributed, random, and of the right size by comparison with the Correlated Solution speckle pattern stamps. Good focus and lighting was achieved for this speckle pattern and was verified during setup using the tools in VIC-Snap. It is possible that the speckle can be improved. If this test methodology is used again and higher precision results are required, the speckle pattern technique and acceptable results should be further investigated, as it is a critical factor in the 3D DIC results [53].

The digital extensometer tools available in VIC-3D 9 were practical to compare results; however, the scatter in the extensometer values limited confidence in the results (see Figures 5.1 and 5.5). It is possible that the calibration, speckle pattern, and/or setup imperfections contributed to local scatter in the measured facesheet strain.

Taking into account all 3D DIC results, the following is offered as a recommendation for further use of the equipment:

1. Maintain awareness of the resolution of the correlation and the area being considered. The VIC-3D 9 performs data smoothing between subset correlation results to help reduce error. This smoothing may

mask particularly small areas with high strain gradients. If the results generated for an area contain too few subsets, there is an increasing potential for those results to be skewed. If the results of a particularly small area (such as the knife edge / facesheet interface) are of interest, additional testing with a new setup that focuses on that area using smaller subsets (higher-resolution camera or smaller field of view) is needed.

2. Both the scatter in extensometer plots and frame-by-frame examination of facesheet strain results highlight that local correlation errors can occur in a single frame or short series of frames. In the extensometer results, this is represented as scatter, where there is no reasonable physical explanation for scatter in the measurement. In a frame-by-frame analysis, this is manifested by local momentary "hot" or "cold" spots in the values generated. For extensometer results, scatter must be taken into account. For frame analysis, multiple frames should be considered together to rule out any local and temporary correlation issues in a given frame.

6.1.4 Strain Validation

Although there was some scatter in the strain measured by the DIC compared to the strain gauge values (discussed in Section 5.1.2), the scatter was relatively small and the average difference was exceptionally small. The strain validation provided confidence in the ability of the DIC system to characterize the strain behaviour of the facesheet. In addition, it highlighted some of the limitations of data interpretation for a given DIC setup, the inherent data smoothing process, and the effective resolution of the results.

Once the load was applied to the strain validation panel (see Figure 5.1.2), the average DIC strain is offset from the strain gauge by -0.0028% strain, which is a small but noticeable amount. As this is present only when the load is applied, it is proposed that this is the result of the paint layer. A thin layer of paint is applied to the facesheet to create the black and white speckle pattern. This paint has a much lower modulus of elasticity than the aluminum facesheet. As a result, the visible face of the paint would be expected to deform slightly less than the face of the paint adhered to the aluminum facesheet. An opportunity exists for further research to investigate this phenomenon.

6.1.5 CAI

The quality control measures implemented for test panel fabrication (Subsection 6.1.1) and support fixture alignment (below) were sufficient to generate meaningful results in characterizing edge distance effects. The failure was initiated in the dent area in all dented test panel cases.

There were four indicators of the dent-edge proximity affecting CAI behaviour as characterized by residual strength, deformation, and facesheet strain:

1. Increased residual strength as edge distance was reduced;
2. Dent growth asymmetry as discussed in Section 6.3;
3. Failure mode interference as discussed in Section 6.3; and
4. Strain asymmetry as discussed in Section 6.4.

Based on the data collected, it is not clear how much of the asymmetry is caused by the knife edge support and how much would be presented in a CAI test with an unsupported vertical edge. This is discussed further in Section 6.6.

Support Fixture

The boundary conditions provided to the test panel by the support fixture worked as intended by ASTM D8287 [13]. The upper and lower end clamps provided full out-of-plane support with little clamping force on the panel. No out-of-plane movement or slippage was detected between the panel and the clamp. The knife edge supports also performed as intended by preventing outward deformation of the facesheets at the vertical edges and not demonstrating indications of friction effects. No movement or misalignment of the knife edge was detected. Support fixtures of this design are recommended for future CAI testing.

When examining the binary strain data presented in Figures 5.15 through 5.18, a pattern suggests that there was some misalignment of the CAI support fixture; at a given load (net section yield or peak force) in Figures 5.16, 5.17, and 5.18, the area of elastic strain tends to be slightly smaller when the dent is on the left side of the panel. This is most evident when comparing elastic strain at peak force. This suggests that slightly more load may be applied by the support fixture on the left side of the test panel than the right. The vertical separation between the upper and lower portions of the support fixture may have been slightly shorter on the left side than on the right side.

This possible misalignment appears to be small and does not appear to have significantly affected the ability to characterize edge distance effects. Future CAI tests with such a support fixture should pay particular attention to alignment between the upper and lower support fixture. Creating an aluminum or steel test panel template (215 mm × 265 mm) with milled parallel end planes may help to check and set the correct alignment of the support fixture halves.

6.2 Effects of Damage Edge Distance on Residual Strength

The peak force of the test panel configurations presented earlier in Figures 5.6 and 5.7 was used to create Figure 6.2. Figure 6.2 shows that the presence of a

6.3. Effects of Damage Edge Distance on Failure Mode and Deformation

dent at any distance from the panel edge reduces residual strength below that of an undamaged panel. Residual strength is lowest for dents further from the panel edge. The centre dent configuration had the lowest overall average residual strength of approximately 72 kN, where, of the dented panels, the 40 mm edge distance had the highest average residual strength at 76 kN. The undamaged panel had the most residual strength at 83 kN.

For the test panel damage configurations tests, the damage edge distance appears to have an inverse relationship with the residual strength of damaged panels subjected to edge-wise compression. The error bars show one standard deviation. It is recommended that a statistical analysis be included in any future research to better understand any dent size and placement thresholds. This changing residual strength with edge distance should be considered with the data collected on facesheet strain; this will be discussed further in Section 6.4. Reasons for the effect of edge distance on residual strength will be discussed in Section 6.6

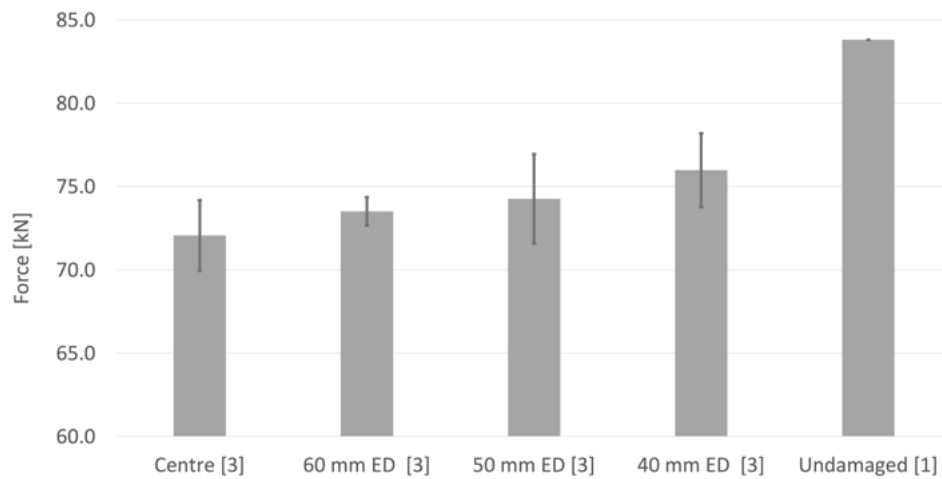


Figure 6.2: Residual strength distribution of for all tested panel. The results are averaged for each configuration. The error bars represent the standard deviation. Sample sizes of 3 and 1 are indicated in square brackets.

6.3 Effects of Damage Edge Distance on Failure Mode and Deformation

Figure 6.3 is a bar graph showing the average dent area of each damage configuration in each of the key compression stages. The area was calculated in ImageJ as described in Section 4.8 and is the total white area of the images

6.3. Effects of Damage Edge Distance on Failure Mode and Deformation

presented in Figures 5.8 through 5.11. There is little change in the dented area between the start of the compression test (unloaded) and when net section yield occurs. The dent areas increase between the net section yield and the peak force. The dent area present at the peak load reduces as the edge distance decreases. The relationship between the dent area at the peak force for the 60 mm ED, 50 mm ED, and 40 mm ED dented panels appears to be linear. This is confirmed in Figure 6.5 which shows a linear line of best fit calculated in Excel for the dent area at peak load of the non-centre damaged panels. Figure 6.4 provides an example of dent area and width measurements.

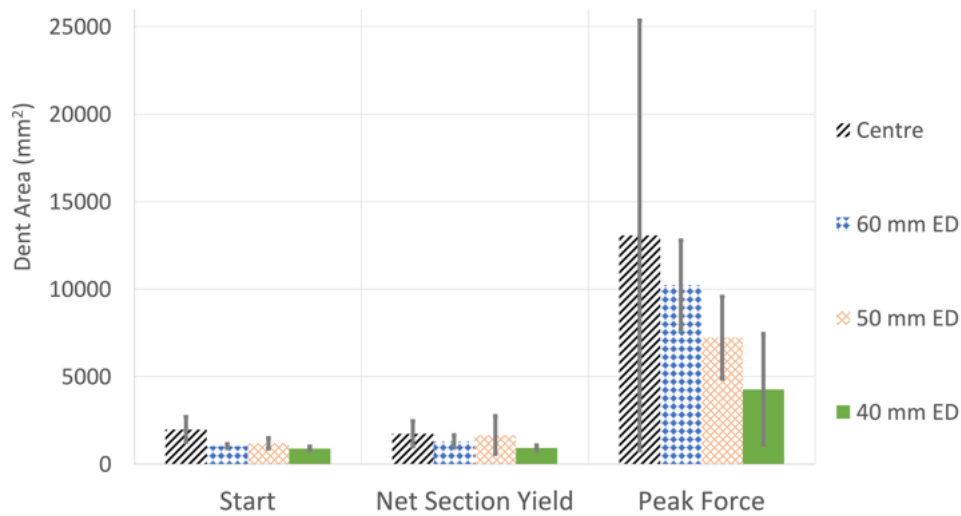


Figure 6.3: Change in average dent area for each configuration. The error bars represent the standard deviation. Data used for this Figure is available at Table B.1.

Figure 6.6 is a bar graph showing the average width of each damage type in the compression stage presented in Figures 5.8, through 5.11 and Table 5.3. In all cases, the width is measured horizontally, perpendicular to the compression direction (see Figure 6.4). There is little change in dent width between the start of the compression test (unloaded) and when net section yield occurs. The increase in dent width is larger between the net section yield and the peak force condition. At peak force, there is no significant change in the relative dent width of each configuration.

The growth of the dent area appears to be more sensitive to edge distance than dent width is sensitive to edge distance. The average 60 mm ED dent area is smaller than the centre dent, whereas the average 60 mm ED dent width is the same as the centre dent. Only in the 50 mm and 40 mm ED dent

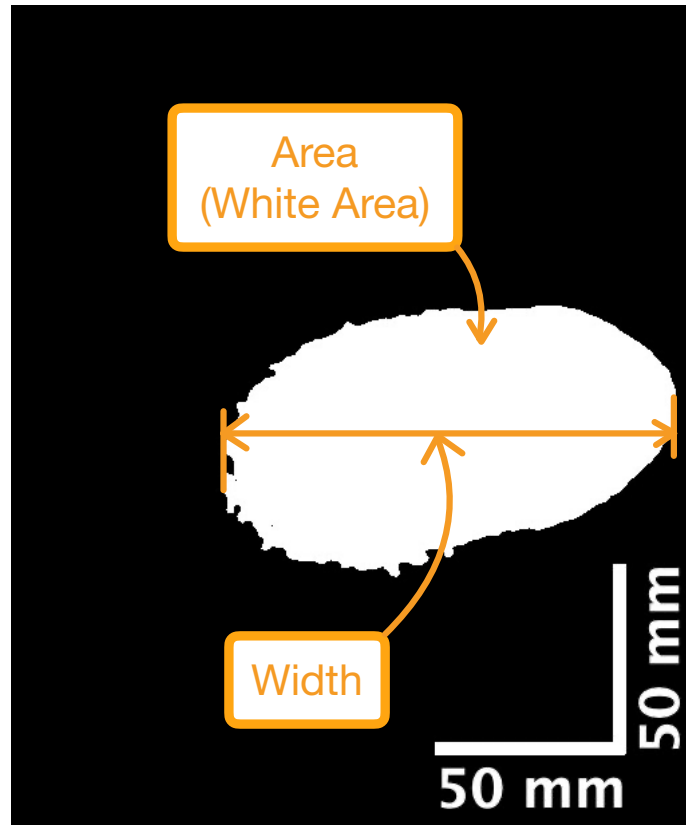


Figure 6.4: Dent area and width measurement performed in ImageJ.

configuration does the average dent width reduce. The proximity of the knife edge reduces the growth of the dent area overall and encourages a narrower dent, particularly in the region closest to the edge of the panel. This can be seen by comparing the elongated dent shapes at peak force of the 40 mm ED panels in Figure 5.11 with the more circular dents at peak force of the 60 mm ED panels in Figure 5.9.

The effect of the damage edge distance on dent deformation suggests that knife edge supports increasingly help prevent dent growth when the dent is closer to the edge. As the knife edge on the top facesheet only retains the top facesheet from moving outward (and the dent is an inward deformation), the knife edge on the bottom facesheet must be retarding the dent growth as the peak load is approached. Because the knife edge acts on the bottom facesheet, it is likely that the effect of edge distance retards Euler macrobuckling of the sandwich panel (see Figure 3.2 (a)) in addition to preventing outward deformation of the bottom facesheet.

Figure 6.7 shows the compressive displacement required to reach the maximum load for each edge distance. These displacement data are the same as

6.3. Effects of Damage Edge Distance on Failure Mode and Deformation

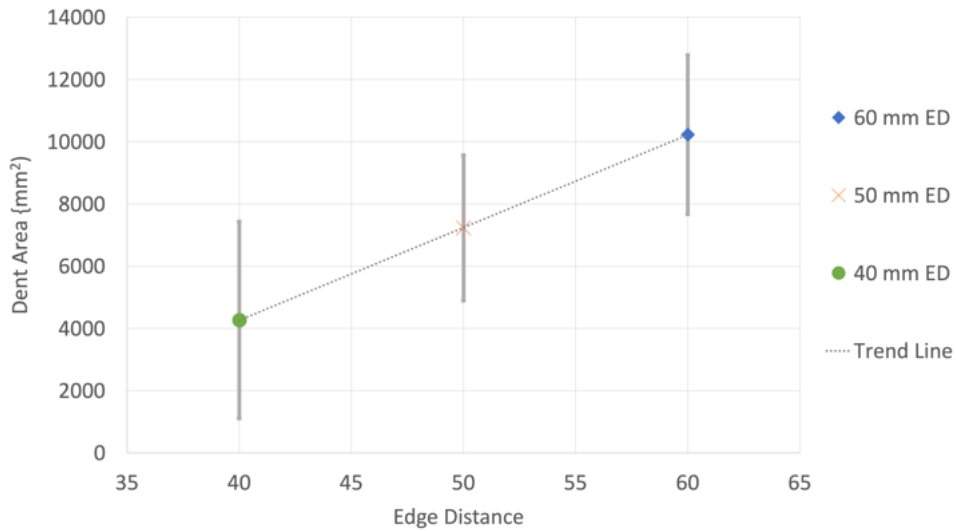


Figure 6.5: Average dent area at peak force demonstrates a linear relationship for the 40 mm ED, 50 mm ED, and 60 mm ED dented panels tested. The error bars represent the standard deviation.

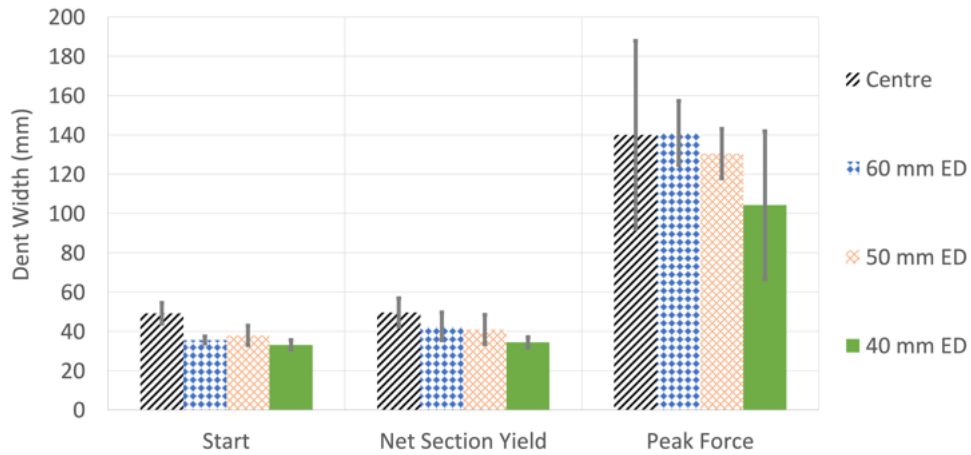


Figure 6.6: Change in average dent width for each configuration. The error bars represent the standard deviation. Data used for this Figure is available at Table B.1.

6.3. Effects of Damage Edge Distance on Failure Mode and Deformation

those presented in Figures 5.6 and 5.7. Over 70 % more displacement is required to achieve the peak load of the undamaged panels (4.7 mm) as compared to all damaged panels (2.7 mm mean displacement).

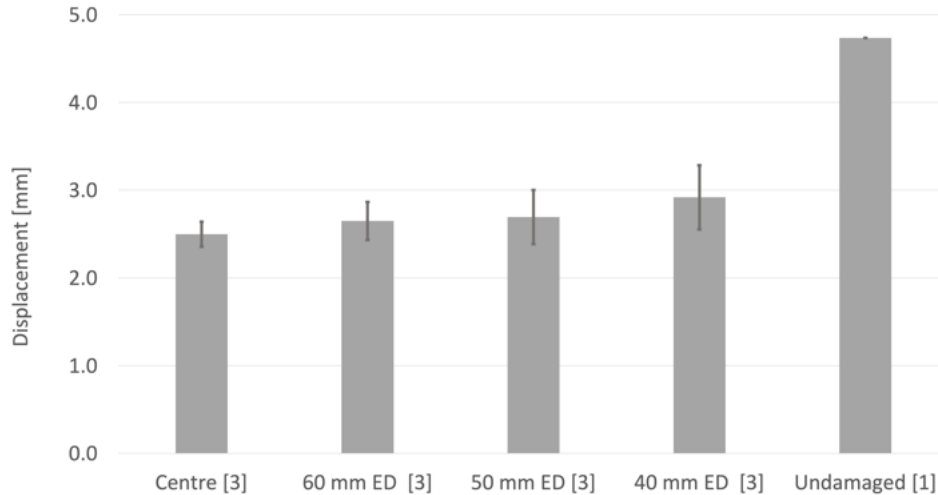


Figure 6.7: Displacement at peak load all tested panel. The results are averaged for each configuration with displacement normalised to the displacement at a 5 kN pre-load to minimise the effect of test apparatus and test panel settling. The error bars represent the standard deviation. Sample sizes of (3) and (1) are indicated. Data used for this Figure is available at Table B.2.

Taking into account the facesheet deformation data generated by VIC-3D 9 and ImageJ (earlier in this section), post-failure panel inspection (discussed and presented in Section 5.3), and the observation of failures during the experimental tests, failure of the test panels is best characterized as either support-edge-limited Euler macrobuckling (Figure 3.2 (a)) or modified facesheet wrinkling (Figure 3.2 (d)).

The condition of the rear of the test panels post-failure is a clear indication that the loaded panels wanted to macrobuckle away from the dented facesheet (see Figure 5.13). Every rear facesheet is characterized by an outward deformation and a wrinkle on the back facesheet at the mid-plane, opposite the dent on the front facesheet. However, simple Euler macrobuckling is not possible because the knife edge supports restrict the macrobuckling motion at the panel edges.

The dented facesheet on the front of the damaged sandwich panel has, at least at a local level, geometric characteristics similar to those of a facesheet that has undergone a wrinkling failure (see Figure 5.12). Before CAI, the facesheet

in the dent area is already deformed into a local wrinkling-like facesheet geometry. This precondition due to the dent ensured inward wrinkling in the original dent area. However, as seen by the variations in post-failure geometry shown in Figure 5.12, the area outside the original dent could wrinkle inward or outward. The precondition of the dented area of the facesheet does not appear to dictate the direction of wrinkling in the adjacent undented area of the facesheet. The variation in the wrinkling direction of the undamaged front facesheet area is indicative of instability in that facesheet.

The growth of this "wrinkled" test panel is theorized to be limited in CAI tests by two main forces:

- 1 Dent effect. The first is the shear and crush strength of the honeycomb core. Under CAI load, the top facesheet in the dent and immediately outside the dent wants to deform further out-of-plane in a buckling fashion, preferable towards the honeycomb core, as the dent is already out-of-plane in this direction. The core prevents this deformation. This resistance force is always present during loading. Dent growth is only possible if this resistance is overcome (the core must be crushed).
- 2 Edge distance effect. The second force that limits the growth of the dent is the knife edge support that keeps the edge of the panel in the plane. Macrobuckling creates a curvature in the panel that adds additional compressive load onto the dented top facesheet as it is on the inside face of the curvature. As curvature is limited in proximity to the knife edge support, dented areas placed closer to the edge have less overall bending, and therefore less compressive force is carried in the dented area.

It would be interesting to confirm this theory by examining the rear facesheet strain. The magnitude, distribution, and, importantly, timing of the facesheet strain are of interest. In the current data, it is not clear whether the loads transferred into the rear facesheet from the wrinkling front facesheet are present and grow or when the macrobuckling loads become dominant.

The final note on deformation and failure mode will be to comment on the hardening rate or something close to a structural composite modulus of plasticity. The curvature of the force-displacement data presented in Figures 5.6 and 5.7, beginning at the yield inflection point and ending at the point of catastrophic failure, is examined. The same behaviour is apparent in the stress-strain Figures 5.20 and 5.21. The most pronounced curve is a centre dent panel. The least pronounced curve is either a 50 mm ED or a 40 mm ED dent panel. This suggests that the edge distance has an effect on the work hardening behaviour. There is an opportunity to further investigate this area of plastic deformation differentiation.

6.4 Effects of Damage Edge Distance on Strain and Asymmetry

Figures 6.8 and 6.9 present elastic strain area data from Figures 5.15 through 5.18 in bar graphs. Due to the significant reduction in the elastic strain area between the net section yield and peak load, the data are presented in two figures to permit comparison of the panel configurations at both data points. At net section yield, the elastic strain area tends to increase as damage edge distance is reduced. However, at peak load, there is no significant difference between the elastic strain area of the three configurations.

There is a reduction in the average elastic strain area of all test panel configurations between the net section yield and the peak loads. The average elastic strain area ranges from more than 7500 mm^2 to less than 500 mm^2 . At net section yield, the average elastic strain area increases as the edge distance decreases. The same trend does not appear to be present at peak load, especially considering the relative size of the error bars (1 standard deviation).

The area of the panel that exhibits elastic strain, especially at the net section yield load, suggests that a smaller edge distance reduces the total compressive strain in the facesheet or that it changes the strain distribution. In theory, the total strain should be the same in all test configurations for a given applied CAI displacement. Figure 5.6 plots displacement against load and confirms that all panels had similar displacements at the net section yield load of 59 kN. As this analysis only considers the area of strain under the yield strain threshold, it is still possible that the average strain is the same in all configurations and only the distribution is different. That is, the average elastic strain could be lower when the elastic strain area is smaller and/or the average plastic strain is lower when the plastic strain area is larger. Another possibility is that a greater portion of the load that causes the strain is being carried outside of the DIC correlation area. The area outside the DIC correlation area is immediately next to or under the knife edge support: this would mean that edge effects are present.

Facesheet strain was higher in the dent affected area closest to the centre of the panel than in the area closest to the knife edge (see Figure 5.14 for an example). This is interpreted to mean that the sandwich panel transferred loads into the knife edge support.

The asymmetry in the strain distribution is visible in all dented panels of 60 mm, 50 mm and 40 mm ED (see Figure 5.19). The outer edges of the elastic strain region are larger on the knife edge side of each dent following the peak load. This indicates that the load is being redirected to the knife edge, toward the undamaged section of the test panel, or both. This asymmetry was also visible before the peak load, as shown for the test panel 2023-004 in Figure 5.14. For test panel 2023-004, peak load occurred at frame 478: however, strain asymmetry is apparent earlier in frames 400 and 450.

6.4. Effects of Damage Edge Distance on Strain and Asymmetry

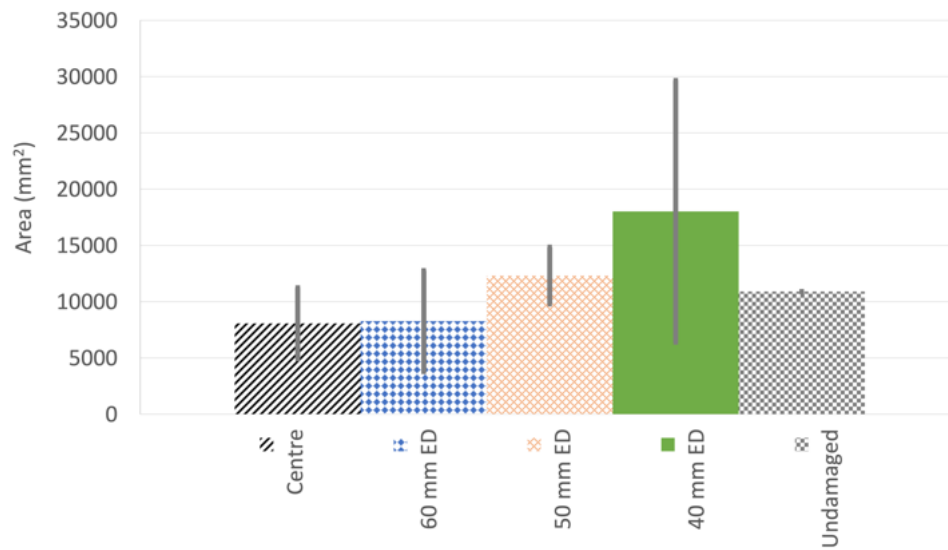


Figure 6.8: Elastic strain area comparison at net section yield. Error bars represent the standard deviation.

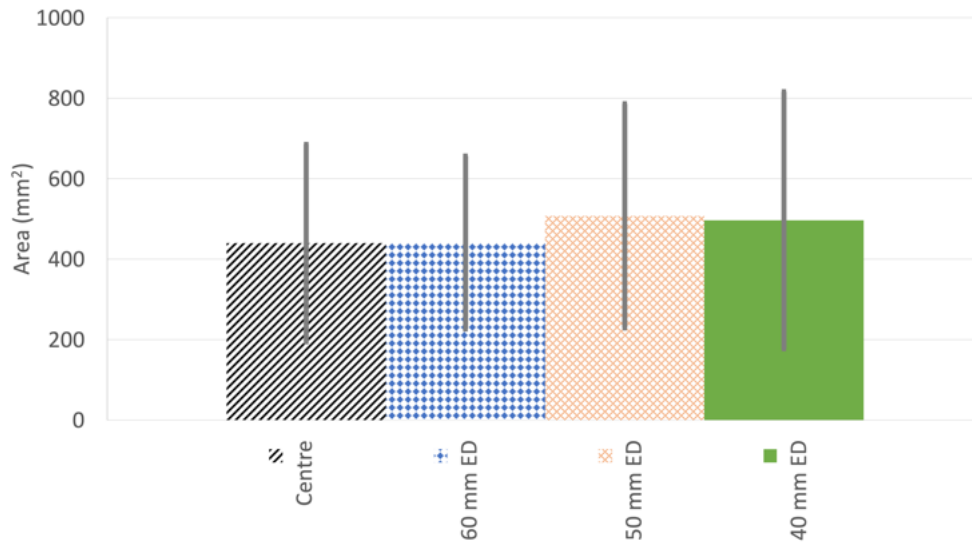


Figure 6.9: Elastic strain area comparison at peak load. Error bars represent the standard deviation. The undamaged panel had zero elastic strain in the facesheet at peak load.

6.5 Stress-Strain

The sandwich panel stress-strain relationship determined by plotting average facesheet strain from the DIC results against the stress calculated from the load cell data and the facesheet cross-sectional area in Section 5.4 is further analyzed. Figure 6.10 was created from Figure 5.20 in Excel by generating a line of best fit going through point the origin (0,0) for all test panel stress-strain data before up to the facesheet material yield stress, σ_y , of 270 MPa was achieved. The slope of that line represents the experimental modulus of elasticity, E_{exp} .

An E_{exp} of 72.7 GPa was calculated in Excel. E_{exp} is less than 1% smaller than the published modulus of elasticity for the facesheet material, 0.020 inch) thick 2024-T3-clad aluminum, 73.1 GPa [58]. Additionally, it should be noted that the MTS system (including the load cell) was calibrated by MTS Systems Corporation without this support fixture installed. Consequently, small losses in the system are probable which would slightly reduce the compressive forces measured by the load cell and reduce the calculated E_{exp} . The true experimental loads and the calculated experimental modulus of elasticity may be closer to 73.1 GPa.

In edge-wise compression, the dented and undamaged metallic honeycomb sandwich panels tested performed to the material properties of the facesheet material in the elastic region, before buckling occurs. This indicates that the in-plane stiffness depends on the cross-sectional area and properties of the facesheet material. All in-plane compression loads are carried by the facesheet. Furthermore, all dented panel configurations and undamaged panels have the same overall stress-strain and force-displacement performance in the elastic region (below the panel's net section yield load).

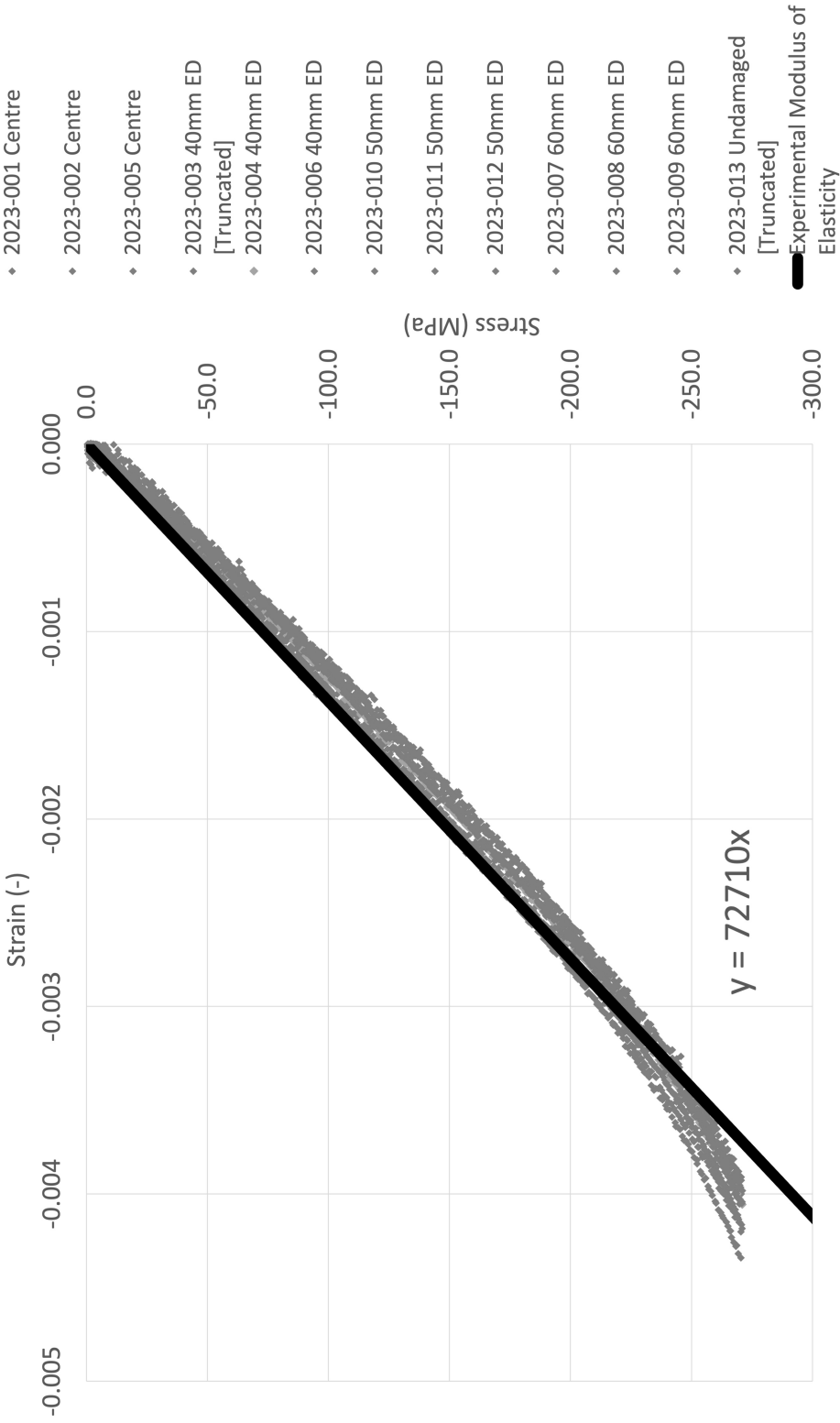


Figure 6.10: Stress-strain CAI Performance. Stress is calculated by dividing the force data from the load cell (provided to the DIC computer via an analogue DAC) by the cross-sectional area of the facesheet. Strain is the average facesheet strain from DIC results. A line of best fit was used in Excel to generate the experimental modulus of elasticity with slope 72.7 GPa

6.6 Effects of Edge Distance and Engineering Application

Several factors indicate the knife edge influences the response of the dented sandwich panel including:

1. Residual strength being inversely proportional to edge distance as discussed in 6.2;
2. Dent growth being asymmetrical with more dent growth towards the panel centre than towards the knife edge support as discussed in Section 5.3 and 6.3;
3. Failure mode interference included stunted facesheet wrinkling and macrobuckling by the knife edge support as discussed in Section and 5.3 and 6.3; and
4. Strain asymmetry with elastic strain tilting towards the knife edge as discussed in Section 6.4.

Each of these indications of the interaction suggest that the load is transferred by one or both of the facesheets into the knife edge. Factors 2 and 3 above are considered direct indicators, as it is not reasonable to assume that these effects would be present with unsupported vertical test panel edges. These factors are related to the physical deformation of the test panel being restricted by the presence of the knife edge support. Factors 1 and 4 are indirect indicators, as it is possible that these indicators exist to some extent with unsupported vertical test panel edges.

Comparative damage edge distance testing in a CAI support fixture without vertical edge support could help clarify factors 1 and 4. Additionally and potentially more valuable to the prediction of the residual strength of the sandwich panel, instrumentation of the interface area between the facesheets and the knife edge in the same tests would clarify load transfers between the test panel and the knife edge. This could also be explored further in finite element models.

It is not clear exactly how representative the knife edge is of a manufactured sandwich panel edge that is fastened to other structural components. Figure 6.11 presents a typical manufactured aluminum honeycomb sandwich panel edge. The knife edge support used in these CAI tests may not be sufficiently representative of the combined effects of a manufactured edge's taper, laminated facesheets, and fastener connection to the other structural members. To better understand how representative of the damage edge distance effects on aircraft panels this support fixture with a knife edge support is, it would be valuable to perform the same CAI instrumented test with a manufactured edge secured to a representative structural member. 3D DIC results for the panel edge, including the fasteners and the attaching point, would be of particular interest.

In terms of revisiting the damage edge distance limits, the damage edge distance does not appear to significantly affect the stiffness of the sandwich panel or deformation below the net section yield loads. All test panels behaved

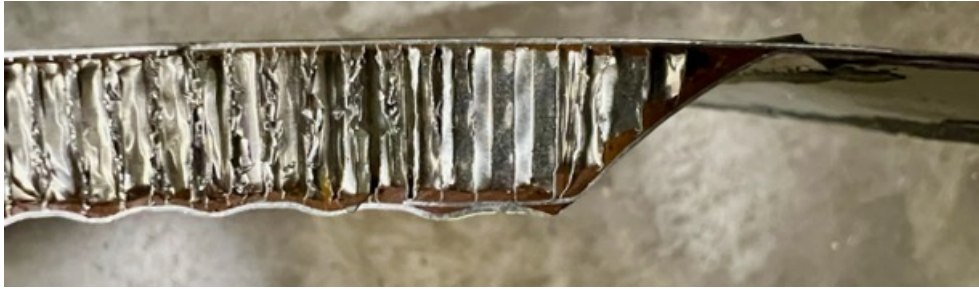


Figure 6.11: Cross sectional view of the manufactured edge of a CH146 Griffon aluminum honeycomb sandwich panel. At the edge, the core is tapered and facesheets are joined together into a laminated aluminum sheet that can be riveted or otherwise fastened to other structural members.

similarly below the net section yield load of 59 kN in Figure 5.6 and stress-strain below 270 MPa in Figures 5.20 and 6.10. Neither the dent area nor the dent width appear to change significantly between the unloaded condition and the net section yield in Figures 6.3 and 6.6. However, the potential inverse relationship between the elastic strain area in the facesheet and the damage edge distance shown in Figure 6.8 suggests that the strain distribution of the facesheet may be affected by the edge distance and loads may begin being shed into the edge support before net section yield. This potential trend is not very pronounced, especially when considering the one standard deviation error bars. Both the strength of the fasteners that connect the panel to adjacent structures and the adjacent structure itself should be considered when the damage edge distance is 60 mm or less for margins of safety until this is researched further.

Further research should include a parametric analysis of damage edge distance effects on residual strength, deformation (including dent growth data) and facesheet strain behaviour.

7 Conclusion

Conclusions are drawn and categorised by research goal, where possible. These conclusions are drawn for the specific test panel configuration (materials, dimensions, dent sizes, etc.) and the test method used.

7.1 FEA Model Validation

At this time, the research group has not modelled damage edge distance effects, and therefore no conclusions can be drawn in this regard beyond the related conclusions below concerning test methodology successes.

7.2 Experimental Test Methodology

1. The fabrication method developed and used resulted in ASTM D8287-compliant test specimens as discussed in Section 6.1; and
2. 3D DIC can be used as an alternative far-field strain measurement instrument to strain gauges as discussed in Section 6.1.

7.3 Damage Edge Distance Effects

1. Residual Strength:
 - a. Residual strength increases as damage edge distance is reduced, as discussed in Section 6.2;
 - b. For both dented and undamaged sandwich panels, in-plane compression loads are carried by the facesheet as shown by the stress-strain behaviour discussed in Sections 6.5 and 6.6;
2. Failure Mode and Deformation:
 - a. The growth of dent area and dent width between net section yield and peak loads is reduced as damage edge distance is reduced as discussed in Section 6.3;
 - b. Dent growth is asymmetric at damage edge distances of 60 mm or less, as discussed in Section 6.3; and
3. Facesheet strain: The facesheet strain is asymmetric at damage edge distances of 60 mm or less, with less strain present on the side of the dent closest to the edge of the panel, as discussed in Section 6.4.

7.4 Overall Conclusion

Dented sandwich panels appear to be increasingly shedding loads on the support fixture and increasing total residual strength as the damage edge distance is reduced, as discussed in Section 6.6.

Bibliography

- [1] Andrzej Katunin et al. “Characterization of quasi-static behavior of honeycomb core sandwich structures”. In: *Modelowanie Inzynierskie* 22.53 (2014), pp. 78–84.
- [2] Quanjin Ma et al. “A review of the recent trends on core structures and impact response of sandwich panels”. In: *Journal of Composite Materials* 55.18 (2021). eprint: <https://doi.org/10.1177/0021998321990734>, pp. 2513–2555. DOI: 10.1177/0021998321990734. URL: <https://doi.org/10.1177/0021998321990734>.
- [3] W.D. Callister and D.G. Rethwisch. *Materials Science and Engineering: An Introduction, 8th Edition*. Wiley, 2009. ISBN: 978-0-470-94166-9. URL: <https://books.google.com/books?id=0aIbAAAAQBAJ>.
- [4] Mengqian Sun. “Low-velocity impact and contact analyses of adhesively bonded aluminum honeycomb sandwich panels”. PhD thesis. Kingston, ON: Queen’s University, July 2021. 160 pp.
- [5] Ahmed K. Noor, W. Scott Burton, and Charles W. Bert. “Computational Models for Sandwich Panels and Shells”. In: *Applied Mechanics Reviews* 49.3 (Mar. 1996), pp. 155–199. ISSN: 0003-6900. DOI: 10.1115/1.3101923. URL: <https://doi.org/10.1115/1.3101923>.
- [6] W. Fairbairn. *An Account of the Construction of the Britannia and Conway Tubular Bridges: With a Complete History of Their Progress from the Conception of the Original Idea, to the Conclusion of the Elaborate Experiments which Determined the Exact Form and Mode of Construction Ultimately Adopted*. J. Weale, 1849. URL: <https://books.google.ca/books?id=FDhaz30vibUC>.
- [7] BAE Systems and BAE Systems Heritage. *De Havilland Mosquito: The fastest fighter-bomber of World War II*. URL: <https://www.baesystems.com/en/heritage/de-havilland-mosquito> (visited on 01/13/2023).
- [8] GR Rayjade and GS Rao. “Study of Composite Sandwich Structure and Bending Characteristics—A Review”. In: *International Journal of Current Engineering and Technology* 5.2 (2015), pp. 797–802.

-
- [9] D. Zenkert and Nordic Industrial Fund. *The Handbook of Sandwich Construction*. North European Engineering and Science Conference series. Engineering Materials Advisory Services, 1997. ISBN: 978-0-947817-96-1. URL: <https://books.google.ca/books?id=xgtpQgAACAAJ>.
- [10] Federal Aviation Administration. *AC 25.571-1 - Damage Tolerance and Fatigue Evaluation of Structure*. Sept. 28, 1978. URL: https://www.faa.gov/regulations_policies/advisory_circulars/index.cfm/go/document.information/documentID/865446.
- [11] Public Services {and} Procurement Canada. *Government of Canada announces contract to extend life of Royal Canadian Air Force fleet of 85 CH-146 Griffon helicopters*. May 30, 2022. URL: <https://www.canada.ca/en/public-services-procurement/news/2022/05/government-of-canada-announces-contract-to-extend-life-of-royal-canadian-air-force-fleet-of-85ch146-griffon-helicopters.html> (visited on 03/06/2024).
- [12] ASTM International. *D7137/D7137M-23 - Standard Test Method for Compressive Residual Strength Properties of Damaged Polymer Matrix Composite Plates*. International Standard D7137. ASTM International.
- [13] ASTM International. *D8287/D8287M - 22 Standard Test Method for Compressive Residual Strength Properties of Damaged Sandwich Composite Panels*. International Standard D8287/D8287M. ASTM International. (Visited on 05/11/2023).
- [14] ISO. *18352:2009 Carbon-fibre-reinforced plastics — Determination of compression-after-impact properties at a specified impact-energy level*. International Standard 18352:2009(en). Committee ISO/TC 61/SC 13. International Organization for Standardization), Aug. 2009.
- [15] Hexcel Composites. *Hexcel Technical Notes - Mechanical Testing of Sandwich Panels*. Mar. 2007. URL: <https://www.hexcel.com/resources/technology-manuals>.
- [16] ASTM International. *D7249/D7249M-20 Standard Test Method for Facesheet Properties of Sandwich Constructions by Long Beam Flexure*. International Standard D7249/D7249M-20. ASTM International.
- [17] Jiangtao Wang et al. “Compression performances and failure maps of sandwich cylinders with pyramidal truss cores obtained through geometric mapping and snap-fit method”. In: *Composite Structures* 226 (2019), p. 111212. ISSN: 0263-8223. DOI: <https://doi.org/10.1016/j.compstruct.2019.111212>. URL: <https://www.sciencedirect.com/science/article/pii/S0263822319314904>.

-
- [18] Simonetta Boria and Giuseppe Forasassi. “Honeycomb sandwich material modelling for dynamic simulations of a crash-box for racing car”. In: *WIT Transactions on the Built Environment*. Vol. 98. May 2008. DOI: 10.2495/SU080171.
- [19] Jakub Koci. *Everything you need to know about infills*. Prusa Blog. URL: https://blog.prusa3d.com/everything-you-need-to-know-about-infills_43579/ (visited on 02/23/2024).
- [20] King Home Printing. *What is Corrugated Cardboard? Different Uses And Types*. Feb. 1, 2021. URL: <https://kh-pack.com/sustainable-packaging/corrugated-cardboard/> (visited on 02/22/2024).
- [21] Tomasz Wierzbicki. “Crushing analysis of metal honeycombs”. In: *International Journal of Impact Engineering* 1.2 (1983), pp. 157–174. ISSN: 0734-743X. DOI: [https://doi.org/10.1016/0734-743X\(83\)90004-0](https://doi.org/10.1016/0734-743X(83)90004-0). URL: <https://www.sciencedirect.com/science/article/pii/S0734743X83900040>.
- [22] Mengqian Sun et al. “Surface and honeycomb core damage in adhesively bonded aluminum sandwich panels subjected to low-velocity impact”. In: *Composites Part B: Engineering* 230 (2022), p. 109506. ISSN: 1359-8368. DOI: <https://doi.org/10.1016/j.compositesb.2021.109506>. URL: <https://www.sciencedirect.com/science/article/pii/S1359836821008738>.
- [23] M.F. Ashby. “The properties of foams and lattices”. In: *Mathematical, Physical and Engineering Sciences* 364.1838 (2006), pp. 15–30.
- [24] Gregory Clarke. “Characterization of Low Velocity Impact Damage in Metallic Honeycomb Sandwich Aircraft Panels using Finite Element Analysis.” Masters of Applied Science. Kingston, ON: Royal Military College of Canada, Dec. 2017. 113 pp. URL: <https://hdl.handle.net/11264/1461>.
- [25] Mohan M. Ratwani. *Composite Materials and Sandwich Structures - A Primer, NATO RTO-EN-AVT-156*. See also ADA564486. Battle Damage Repair Techniques and Procedures on Air Vehicles - Lessons Learned and Prospects. RTO-EN-AVT-156. May 2010.
- [26] FAA {and} TCCA. *Implementation Procedures for Airworthiness Covering Design Approval, Production Activities, Export Airworthiness Approval, Post Design Approval Activities, and Technical Assistance, Rev 3*. Apr. 26, 2021. URL: https://tc.canada.ca/sites/default/files/2021-06/April-Final-FAA-TCCA_IPA_REVISION_3.pdf (visited on 03/11/2024).

-
- [27] U.S. Department of Transportation Federal Aviation Administration. *Order 8110.54A Instructions for Continues Airworthiness Responsibilities, Requirements and Contents*. Oct. 23, 2010. URL: https://www.faa.gov/documentLibrary/media/Order/FAA_Order_8110.54A.pdf (visited on 03/11/2024).
- [28] Michael A. Sutton, Jean-Jose Orteu, and Hubert W. Schrieir. *Image Correlation for Shape, Motion and Deformation Measurements: Basic Concepts, Theory and Applications*. Springer, 2009. 321 pp. ISBN: 978-0-387-78746-6. URL: <https://link.springer.com/book/10.1007/978-0-387-78747-3>.
- [29] Nathaniel W. Gardner, Mark W. Hilburger, and W. Allen Waters. *Digital Image Correlation Data Processing and Analysis Techniques to Enhance Test Data Assessment and Improve Structural Simulations*. Jan. 7, 2018. URL: <https://doi.org/10.2514/6.2018-1698>.
- [30] N. J. Hoff and S. E. Mautner. “The Buckling of Sandwich-Type Panels”. In: *Journal of the Aeronautical Sciences* 12.3 (1945). _eprint: <https://doi.org/10.2514/8.11246>, pp. 285–297. DOI: 10.2514/8.11246. URL: <https://doi.org/10.2514/8.11246>.
- [31] D. Zenkert. *An Introduction to Sandwich Construction*. Engineering Materials Advisory Services, 1995. ISBN: 978-0-947817-77-0. URL: <https://books.google.ca/books?id=zc-GQgAACAAJ>.
- [32] R. K. McFARLAND. “HEXAGONAL CELL STRUCTURES UNDER POST-BUCKLING AXIAL LOAD”. In: *AIAA Journal* 1.6 (1963). _eprint: <https://doi.org/10.2514/3.1798>, pp. 1380–1385. DOI: 10.2514/3.1798. URL: <https://doi.org/10.2514/3.1798>.
- [33] Janes. *Bell 212*. Military Intelligence (Open-Source). URL: <https://customer.janes.com/display/jhms4990-jhms#Current%20Versions-CH-135>: (visited on 02/23/2024).
- [34] Yixiong Feng et al. “Creative design for sandwich structures: A review”. In: *International Journal of Advanced Robotic Systems* 17.3 (2020). _eprint: <https://doi.org/10.1177/1729881420921327>, p. 1729881420921327. DOI: 10.1177/1729881420921327. URL: <https://doi.org/10.1177/1729881420921327>.
- [35] ASTM International. *C364/C364M-16 Standard Test Method for Edgewise Compressive Strength of Sandwich Constructions*. International Standard C364/C364M. ASTM International. (Visited on 09/15/2022).
- [36] ASTM International. *D7766/D7766M-16 Standard Practice for Damage Resistance Testing of Sandwich Constructions*. International Standard D7766/D7766M-16. ASTM International.

- [37] Patrick M. Schubel, Jyi-Jiin Luo, and Isaac M. Daniel. “Impact and post impact behavior of composite sandwich panels”. In: *Composites Part A: Applied Science and Manufacturing* 38.3 (2007), pp. 1051–1057. ISSN: 1359-835X. DOI: <https://doi.org/10.1016/j.compositesa.2006.06.022>. URL: <https://www.sciencedirect.com/science/article/pii/S1359835X06001989>.
- [38] D. Wowk et al. “An experimental and numerical investigation of core damage size in honeycomb sandwich panels subject to low-velocity impact”. In: *Composite Structures* 254 (2020), p. 112739. ISSN: 0263-8223. DOI: <https://doi.org/10.1016/j.compstruct.2020.112739>. URL: <https://www.sciencedirect.com/science/article/pii/S0263822320326659>.
- [39] D. P. W. Horrigan and R. A. Staal. “Predicting Failure Loads of Impact Damaged Honeycomb Sandwich Panels - A Refined Model”. In: *Journal of Sandwich Structures & Materials* 13.1 (2011). _eprint: <https://doi.org/10.1177/1099636208105039>, pp. 111–133. DOI: 10.1177/1099636208105039. URL: <https://doi.org/10.1177/1099636208105039>.
- [40] Mark Boctor. “Predicting the Effects of Interaction Between Multiple Impacts on the Residual Strength in Metallic Honeycomb Sandwich Aircraft Panels Subject to Low-Velocity Impact Damage”. MASc Thesis. Royal Military College of Canada, Sept. 2021. 106 pp. URL: <https://hdl.handle.net/11264/183>.
- [41] Hangyu Ye et al. “Residual compression property and response of honeycomb sandwich structures subjected to single and repeated quasi-static indentation”. In: *REVIEWS ON ADVANCED MATERIALS SCIENCE* 60.1 (2021), pp. 404–417. DOI: doi:10.1515/rams-2021-0033. URL: <https://doi.org/10.1515/rams-2021-0033> (visited on 04/17/2024).
- [42] Fawad Tariq, Muhammad Uzair, and Madni Shifa. “Residual compressive strength of aluminum alloy honeycomb sandwich panel in the presence of multiple impact dents”. In: *Journal of Sandwich Structures & Materials* 24.2 (2022). _eprint: <https://doi.org/10.1177/10996362211036987>, pp. 1189–1205. DOI: 10.1177/10996362211036987. URL: <https://doi.org/10.1177/10996362211036987>.
- [43] ASTM International. *D903-98 Standard Test Method for Peel or Stripping Strength of Adhesive Bonds*. International Standard D903-98. ASTM International, 2017. (Visited on 01/25/2024).
- [44] N. A. Fleck and I. Sridhar. “End compression of sandwich columns”. In: *Composites Part A: Applied Science and Manufacturing* 33.3 (2002), pp. 353–359. ISSN: 1359-835X. DOI: [https://doi.org/10.1016/S1359-835X\(01\)00118-X](https://doi.org/10.1016/S1359-835X(01)00118-X). URL: <https://www.sciencedirect.com/science/article/pii/S1359835X0100118X>.

-
- [45] Hexcel Composites. *Hexcel Technical Manual - Hexweb Honeycom Sandwich Design Technology*. URL: <https://www.hexcel.com/resources/technology-manuals>.
- [46] B. A. Bouwhuis, E. Bele, and G. D. Hibbard. “Edge effects in compression testing periodic cellular metal sandwich cores”. In: *Journal of Materials Science* 43.9 (May 1, 2008), pp. 3267–3273. ISSN: 1573-4803. DOI: 10.1007/s10853-008-2529-x. URL: <https://doi.org/10.1007/s10853-008-2529-x>.
- [47] Thomas D. McQuigg et al. “Compression After Impact Experiments on Thin Face Sheet Honeycomb Core Sandwich Panels”. In: *Journal of Spacecraft and Rockets* 51.1 (2014). eprint: <https://doi.org/10.2514/1.A32427>, pp. 253–266. DOI: 10.2514/1.A32427. URL: <https://doi.org/10.2514/1.A32427>.
- [48] E. Wang and A. Shukla. “Blast Performance of Sandwich Composites with In-Plane Compressive Loading”. In: *Experimental Mechanics* 52.1 (Jan. 1, 2012), pp. 49–58. ISSN: 1741-2765. DOI: 10.1007/s11340-011-9500-5. URL: <https://doi.org/10.1007/s11340-011-9500-5>.
- [49] ASTM International. *D7136/D7136M-20 Standard Test Method for Measuring the Damage Resistance of a Fiber-Reinforced Polymer Matrix Composite to a Drop-Weight Impact Event*. International Standard D7136. ASTM International.
- [50] Home Depot. *Product Specification - RIDGID 9-Amp 7-inch Portable Wet Tile Saw with Stand*. Mar. 31, 2020. URL: <https://www.homedepot.ca/product/ridgid-9-amp-7-inch-portable-wet-tile-saw-with-stand/1000744927> (visited on 01/17/2024).
- [51] LePage. *Technical Data Sheet - LePage PL Premium Construction Adhesive*. Mar. 31, 2020. URL: <https://www.lepage.ca/en/lepage-products/build-things/construction-adhesive/pl-construction-adhesive/pl-premium-construction-adhesive.html> (visited on 01/16/2024).
- [52] Correlated Solutions. *VIC-3D 9 Setup Procedures*. 2021. URL: <https://www.correlatedsolutions.com/product-literature>.
- [53] Correlated Solutions. *Speckle Kit User Manual*. Version 5 2021. 2021. URL: <https://www.correlatedsolutions.com/product-literature>.
- [54] Correlated Solutions. *Correlated Solutions Knowledgebase - Resolution and Accuracy*. Oct. 2023. URL: <https://correlated.kayako.com/article/32-resolution-and-accuracy> (visited on 01/18/2024).
- [55] Correlated Solutions. *Correlated Solutions Knowledgebase - Troubleshooting Calibration Problems*. Nov. 2023. URL: <https://correlated.kayako.com/article/47-troubleshooting-calibration-problems> (visited on 01/18/2024).

- [56] Bruel {and} Kjaer) HBK (Hottinger. *Catman Data Acquisition Software: Connect. Measure. Visualize. Analyze.* URL: https://www.hbm.com/en/2290/catman-data-acquisition-software/?product_type_no=DAQ%20Software.
- [57] R.C. Rice et al. *Metallic Materials Properties Development and Standardization (MMPDS)*. 1st ed. Metallic Materials Properties Development and Standardization (MMPDS): Scientific Report. National Technical Information Service, 2003. URL: <https://ntrl.ntis.gov/NTRL/dashboard/searchResults/titleDetail/PB2003106632.xhtml>.
- [58] LLC Matweb. *Matweb Material Property Data*. <https://matweb.com/>. URL: <https://matweb.com/>.
- [59] Zwick Roell. *Impact Testers and Charpy Impact Testers*. Testing machines for determination of the impact strength of plastics and metals. URL: <https://www.zwickroell.com/products/products-for-impact-testing/#c6326> (visited on 01/31/2024).
- [60] T. Reyno, C. Marsden, and D. Wowk. “Surface damage evaluation of honeycomb sandwich aircraft panels using 3D scanning technology”. In: *NDT & E International* 97 (2018), pp. 11–19. ISSN: 0963-8695. DOI: <https://doi.org/10.1016/j.ndteint.2018.03.007>. URL: <https://www.sciencedirect.com/science/article/pii/S0963869517306461>.

Appendices

A Test Reports and Calibration Certificates.

Test Report

Customer: Upper Canada Steel Inc.
 P.O. Box 917
 253 Industrial Park Road
 Colborne, Ontario K0K 1S0 Canada

Test Report Number: 18D0202
 PO #: RMC10195

DESCRIPTION OF PART

Part #	Thick	Width	Length	Face Material Back Material	Core Material	Lot No.	Shop No.	Qty
500x48x96	.500	48	96	.020-2024-T3-Clad-48 .020-2024-T3-Clad-48	1/4-.002N-5052-(4.3pcf)	092410	AE 1113-1	1

Test Type	T-ID	Required	Results	Average
Peel (Dry)	20841	Avg 25.5 in-lbs/3 in.	1 76	74.3 in-lbs/3 in.
			2 73	
			3 74	
Thickness	20844	0.500±0.010 in.	1 .499 2 .504	.502 in.
Flatness	20845	Max 0.025 in/ft.	1 0	0 in/ft.

Remarks:
 1 PC Released 4/4/2018 DT # 16779

THIS TEST MADE ACCORDING TO SPECIFICATION: Genesco No. 3, Special

I hereby certify that the above tests were made and the results were as shown hereon.

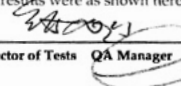

 Director of Tests QA Manager

Figure A.1: Test Report 18D0202 - 0.500x48x96 Aluminum Sandwich Panel



Figure A.2: Manufacturer's Certificate, Strain Gauge Type N11-FA-30-120-11 Lot 9008-411.

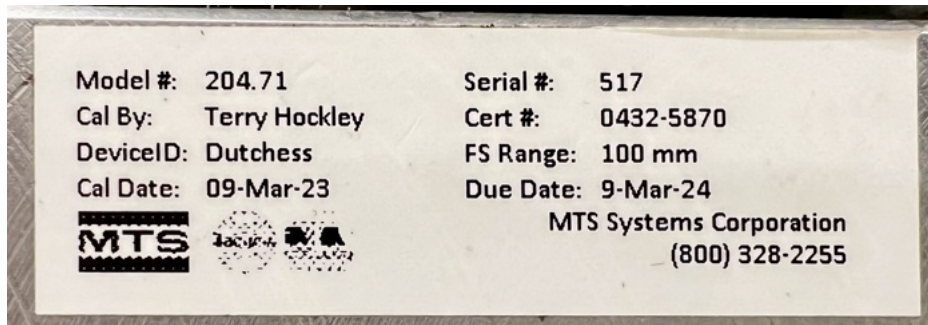


Figure A.3: Calibration Certificate 0432-5870, Dutchess, MTS Model 204.71, Serial 517, expires 9 March, 2024.

B Tabulated Data Used for Graphs

Table B.1: Deformation data presented in Figures 6.3 and 6.6. All values are averages.

		<u>Area (mm²)</u>	<u>width (mm)</u>
	Start	1629.1	45.3
Centre	Net Section Yield	1738.9	49.7
	Peak Force	13066.1	140.0
	Start	1036.9	35.6
60 mm ED	Net Section Yield	1307.0	42.6
	Peak Force	10228.9	140.9
	Start	1195.1	37.9
50 mm ED	Net Section Yield	1665.3	41.0
	Peak Force	7230.6	130.4
	Start	897.2	33.2
40 mm ED	Net Section Yield	927.3	34.4
	Peak Force	4272.7	104.2

Table B.2: Displacement data presented in Figure 6.7

	<u>Test 1 (mm)</u>	<u>Test 2 (mm)</u>	<u>Test 3 (mm)</u>
Centre [3]	2.350	2.509	2.634
60 mm ED [3]	2.415	2.692	2.840
50 mm ED [3]	2.495	2.538	3.048
40 mm ED [3]	3.303	2.576	2.876
Undamaged [1]	4.734	-	-